Technische Universität München
Fakultät für Physik

Quantitative Cardiac PET/MRI: Studies on Validation and Synergies in Clinical Applications of Perfusion Imaging and Tissue Characterization

Karl-Philipp Gerhart Friedrich Kunze

Vollständiger Abdruck der von der Fakultät für Physik der Technischen Universität München zur Erlangung des Akademischen Grades eines

Doktors der Naturwissenschaften (Dr. rer. nat.)

genehmigten Dissertation.

Vorsitzender:		Prof. Dr. Martin Zacharias
Prüfer der Dissertation:	1.	Prof. Dr. Axel Haase
	2.	Prof. Dr. Julia Herzen

Die Dissertation wurde am 15.03.2018 bei der Technischen Universität München eingereicht und durch die Fakultät für Physik am 12.09.2018 angenommen.

Abstract

During the last 20 years, significant efforts have been made towards integration of different clinical imaging modalities within a single device, i.e. multi-modality imaging. While PET/CT was established in clinical practice early on, the more recently introduced PET/MRI devices have so far remained research tools, nevertheless with a wide range of unique potential applications. The main appeal of fully integrated multi-modality imaging is the opportunity to utilize simultaneously acquired data in a way that does not merely add up or cross-validate distinct features of each modality, but exploits them in a truly synergistic fashion. For applications of cardiovascular PET/MRI, it was the main goal of this thesis to develop methods for quantitative image analysis that expand the current understanding of both imaging techniques in ways that would not be conceivable outside of a multi-modality context. The focus of this work is therefore the application of mathematical approaches to model the relationship between imaging data and physiology.

A large portion of this work is dedicated to the field of dynamic contrast-enhanced MRI perfusion imaging, for which opportunities and limitations of fully quantitative analysis have yet to be fully understood. While MRI offers the potential to assess physiologically meaningful parameters beyond perfusion flow, such as vascular permeability and vascular volume, their measurability depends on a number of factors including the physiological state of the tissue or the patient. It is the first major contribution of this thesis to propose an hierarchical framework for analysis of MRI perfusion data, in which an Akaike criterion is used to determine the respective applicability of three mathematically contiguous tissue models, representing distinct degrees of measurability for vascular parameters. In the same patient cohort, exhibiting a wide range of cellular tissue damage post myocardial infarction, it was also shown that estimates of extracellular distribution volume of the MRI contrast agent obtained from only 90 seconds of perfusion data were comparable to standard extracellular volume mapping techniques, which usually require significant equilibration periods of several minutes. As contrast agent doses for the latter are often two- to three-fold higher than for perfusion imaging, the proposed approach is both more time- and contrast agent dose-efficient. Addressing limitations of the described framework, the following two chapters propose tissue model-independent approaches to both assess vascular characteristics using spline-based algorithms as well as to calculate bolus delay time, which is also shown to have a potential value characterizing coronary physiology.

Having established a solid framework for understanding and executing MRI-based perfusion tissue modeling, the fourth chapter describes an evaluation of simultaneously acquired dynamic contrast-enhanced MRI and $^{13}NH_3$-ammonia PET data. While both methods can be used to derive estimates of tissue perfusion flow in mL/min/g, only PET tracers permeate red blood cells and therefore indicate (whole-) blood flow. Conversely, all common MRI contrast agents remain extracellular, implying that resulting plasma flow estimates need to be scaled by a tissue hematocrit fraction in order to be comparable to the cor-

responding PET results. The framework for simultaneous acquisition presented herein for the first time allowed for a combination of PET- and MRI-derived perfusion flow values in order to generate actual estimates of myocardial tissue hematocrit. While relative tissue hematocrit was found to be significantly lower than the usually assumed equality of macro- and microvascular hematocrit would suggest, they were also found to be different between resting and vasodilator-induced stress states. On the basis of the same data, an additional, important contribution towards understanding the limitations of MRI perfusion modeling in the regime of small contrast agent transit times was made: In comparison to the more robust PET approach, it could be shown that application of MRI tissue models, especially the widely-used Fermi-model, may result in unreliably high perfusion estimates if not constrained according to both the respective limits of temporal resolution in the dynamic data as well as to physiological plausibility.

In the final chapter, the same synergistic mindset is applied to myocardial tissue characterization in patients after myocardial infarction, comparing MRI-derived T_1 and extracellular volume estimates with fasted ^{18}F-FDG PET targeted at inflammatory cell populations. It was found that all three imaging markers indicate co-localized but quantitatively independent features of the underlying pathology, with the increase in absolute native T_1 highly correlated to systemic expression of monocytes, as well as absolute extracellular volume estimates highly correlated to creatine kinase-MB expression. Building on these correlates, it was hypothesized that the measured ^{18}F-FDG PET signal, representing a mixture of previously unknown proportions of post-ischemic myocytic glucose consumption and uptake by infiltrative inflammatory cell populations, could be constructed from a combination of the simultaneously acquired MRI markers representing these two pathways. Fits of a linear model yielded similar contributions for post-ischemic and inflammatory signal pathways, challenging the notion of fasted ^{18}F-FDG as a purely inflammatory image signal.

In summary, the presented thesis contains the description and validation of new methods for dynamic contrast-enhanced MRI perfusion quantification, and contributes significantly to the understanding of PET and MRI methods of myocardial tissue characterization. The described combinations of simultaneously acquired PET/MRI data have led to relevant insights with respect to cardiac physiology, thereby providing examples for the scientific value of quantitative multi-modality imaging.

Zusammenfassung

Im Zeitraum der letzten 20 Jahre wurden erhebliche Anstrengungen bezüglich der Kombination unterschiedlicher Bildgebungsmodalitäten innnerhalb eines einzelnen Gerätes unternommen, der sogenannten multimodalen Bildgebung. Während PET/CT frühzeitig im klinischen Betrieb erfolgreich etabliert werden konnte, sind die später eingeführten PET/MRT-Geräte bis heute hauptsächlich in wissenschaftlicher Verwendung, nichtsdestoweniger mit einer großen Bandbreite an einzigartigen Anwendungsmöglichkeiten. Der Hauptanreiz multimodaler Bildgebung besteht in der Möglichkeit zur Verwendung simultan akquirierter Daten, nicht nur als einer Addition bzw. Validierung unterschiedlicher Parameter aus beiden Modalitäten, sondern im Sinne einer tatsächlich synergistischen Nutzung. Es war ein Hauptziel dieser Arbeit, für Anwendungen der kardialen PET/MRT-Bildgebung Methoden zur quantitativen Datenanalyse zu entwickeln, die das momentane Verständnis beider Modalitäten erweitern, und ohne eine multimodale Datenakquisition nicht vorstellbar wären. Der Fokus der Arbeit liegt somit auf der mathematischen Modellierung des Verhältnisses von Bildgebungsdaten und Physiologie.

Ein großer Teil der vorgelegten Schrift befasst sich mit dynamisch kontrastmittelverstärkter MRT-Perfusionsbildgebung, für die Möglichkeiten und Limitationen der quantitativen Auswertung noch unvollständig verstanden sind. Obwohl die MRT prinzipiell eine Abschätzung physiologisch bedeutsamer Parameter zusätzlich zum Perfusionsfluss erlaubt, z.B. vaskuläre Permeabilität und vaskuläres Volumen, hängt deren Messbarkeit von unterschiedlichen Faktoren wie dem physiologischen Zustand des Gewebes oder des Patienten ab. Als erster wichtiger Beitrag dieser Arbeit kann die Vorlage einer hierarchischen Struktur zur Analyse von MRT-Perfusionsdaten angesehen werden. In dieser wird durch ein Akaike-Kriterium über die jeweilige Anwendbarkeit dreier, mathematisch verwandter Gewebemodelle entschieden, entsprechend jeweils unterschiedlichen Graden der Messbarkeit vaskulärer Parameter. In derselben Patientenkohorte, die eine große Bandbreite kardialen Zellschadens nach Infarkt beinhaltete, konnte dazu gezeigt werden, dass Schätzungen des extrazellulären Verteilungsvolumens des MRT-Kontrastmittels auf Basis von nur 90 Sekunden dynamischer Daten vergleichbar mit Ergebnissen von Standardtechniken für die Kartierung von Extrazellulärvolumen sind. Da die Kontrastmitteldosierung für letztgenannte Techniken oft zwei- bis dreimal höher ist als für Perfusionsbildgebung und diese Equilibrierungszeiten von einigen Minuten benötigen, kann der beschriebene Ansatz als eine Zeit- und Dosis-effizientere Alternative angesehen werden. In Bezug auf Limitationen der vorgestellten Methodik, behandeln die folgenden zwei Kapitel Modell-unabhängige Techniken zur Schätzung sowohl vaskulärer Parameter mithilfe eines Spline-Ansatzes, alsauch der Kontrast-Anflutungsverzögerung mithilfe ein Fourier-Phasen-Technik, deren Nutzen für die Charakterisierung koronarer Physiologie gezeigt wird.

Nach Etablierung einer fundierten Methodik zur MRT-basierten Perfusions-Gewebemodellierung, befasst sich das vierte Kapitel mit der Auswertung simultan

akquirierter dynamisch kontrastmittel-verstärkter MRT- und $^{13}NH_3$-Ammoniak PET-Perfusionsdaten. Obwohl beide Methoden verwendet werden können um einen Perfusionsfluss in mL/min/g abzuschätzen, dringen nur PET-Tracer in rote Blutzellen ein und sind somit sensitiv für (Voll-)Blutfluss. Übliche MRT-Kontrastmittel sind dagegen extrazellulär, weshalb die resultierenden Plasmaflusswerte mit einem Gewebehämatokrit skaliert werden müssen, um mit PET vergleichbar zu sein. Der hier vorgestellte, simultane Akquisitionsansatz ermöglichte in diesem Kontext erstmalig eine Kombination von PET- und MRT-Flusswerten zu einer tatsächlichen Abschätzung des myokardialen Gewebehämatokrits. Es ergab sich sowohl ein niedrigerer Gewebehämatokrit als der üblicherweise verwendete, aus der Annahme von gleichem mikro-und makrovaskulärem Hämatokrit hervorgehende Wert, als auch ein Unterschied in diesem zwischen Ruhe- und Vasodilatations-induziertem Stresszustand. Auf Basis derselben klinischen Daten konnte ein weiterer, wichtiger Beitrag zum Verständnis der MRT-basierten Perfusions-Gewebemodellierung kleiner Kontrastmittel-Transitzeiten geleistet werden: Im Vergleich mit der robusteren PET-Auswertung wurde gezeigt, dass Gewebemodelle für die MRT, insbesondere das weit verbreitete Fermi-Modell, zu unzuverlässig hohen Schätzungen des Perfusionsflusses führen können, falls keine Beschränkung der Modelle bezüglich Zeitauflösung der Daten und physiologischer Plausibilität verwendet werden.

Das letzte Kapitel enthält eine weitere Anwendung desselben synergistischen Auswertungsprinzips im Bereich der myokardialen Gewebecharakterisierung bei Patienten nach akutem Myokardinfarkt. Dazu wurden die MRT-basierte Abschätzung des T_1 sowie des Extrazellulärvolumens verglichen mit gefastetem ^{18}F-FDG PET, ausgerichtet auf inflammatorische Zellpopulationen. Es wurde gezeigt, dass alle drei Bildgebungsmarker kolokalisierte, jedoch quantitativ unabhängige Eigenschaften der zugrundeliegenden pathologischen Veränderuneng abbilden. Es zeigten sich Korrelationen zwischen Absolutwerten des nativen T_1 und systemischer Monozytenexpression, und zwischen Absolutwerten des Extrazellulärvolumens und der Expression von Kreatinkinase-MB. Auf Basis dieser Zusammenhänge wurde die Hypothese aufgestellt, dass das gemessene ^{18}F-FDG PET-Signal, bestehend zu unbekannten Teilen aus einer Mischung post-ischämischer, myozytischer Glukoseaufnahme mit Aufnahme durch eingewanderte, inflammatorische Zellpopulationen, durch eine Kombination der simultan akquirierten, diese Signalkanäle repräsentierenden MRT-Parameter konstruiert werden kann. Der Fit eines linearen Modells resultierte in der Schätzung ähnlicher Signalanteile für post-ischämische und inflammatorische Signalkanäle, was die Interpretation von gefastetem ^{18}F-FDG PET als einem rein inflammatorischen Bildsignal infragestellt.

Zusammenfassend enthält die vorgelegte Arbeit sowohl die Beschreibung und Validierung neuer Methoden zur Perfusionsquantifizierung auf Basis dynamisch kontrastmittelverstärkter MRT, sowie Beiträge zum Verständnis von PET- und MRT-basierter myokardialer Gewebecharakterisierung. Die beschriebenen Kombinationen simultan akquirierter PET/MRT-Daten ermöglichten relevante Erkenntnisse in Bezug auf die kardiale Physiologie und sind beispielgebend für den wissenschaftlichen Wert quantitativer multimodaler Bildgebung.

Contents

Part I

Introduction

Chapter 1

Background

Motivation

The field of medical imaging technology encompasses applications of a large range of physical principles to biological systems, including nuclear physics, electromagnetism, ionizing radiation and acoustics. When assessing the timeline of technical developments in imaging science, one can appreciate the last two to three decades as a turn away from successful clinical establishment of entirely new imaging modalities towards an era of technical refinement for existing techniques, paralleled by significant efforts towards integrating different imaging modalities, i.e. so-called multi-modality or hybrid imaging. While sequential application of imaging techniques may often suffice to answer a more complex clinical question at hand, actual integration within a single scanner was expected to greatly increase time efficiency in a clinical setting and open up a broad range of new possibilities for research. The first major clinical success of integrated multi-modality imaging was the combination of positron emission tomography (PET) and computed tomography (CT) within a single PET/CT device [8], which has essentially replaced standalone PET since its introduction in the early 2000s. An important reason for this success is the fact that morphological information provided by the high spatial resolution of CT acts as an important extension to the spatially less well resolved functional and metabolic information from PET. Additionally, the information on x-ray attenuation - which essentially constitutes the CT signal - represents a somewhat natural complement to the emission data gathered from PET, which needs to be corrected for attenuation especially when accurate signal quantification is desired.

As a consequence of this success, significant efforts towards a combination of positron emission tomography with magnetic resonance imaging (MRI) were made. While MRI provides a comparable complement to PET with respect to spatial resolution, its main advantage over computed tomography - not just in the context of multi-modality imaging - is the large range of achievable image contrasts through utilization of different magnetic relaxation properties, without ionizing radiation. However, the development of integrated PET/MRI scanners faced significantly larger obstacles than the corresponding development towards integrated PET/CT. Both the interference between magnetic fields used in MRI with PET hardware, as well as the increased high energy photon attenuation and scattering due to the MRI bed and coil systems have proven to be superb technical challenges for production of an operational, integrated whole-body PET/MRI device.

After the first commercial system received approval by authorities in 2011 [35], it had soon become clear that the mid- to short-term commercial potential of integrated

PET/MRI was not comparable to the earlier success of PET/CT. Even after important technical developments in MRI e.g. towards reliable attenuation estimation [91,108], the much higher price of PET/MRI systems and the significantly lower patient throughput when compared to PET/CT render a cost-effective clinical operation challenging. While considerations with respect to cost and clinical value are subject to change, e.g. due to the potential emergence of PET/MRI applications providing unique clinical value as well as more vendors introducing commercial systems into the market, it can still be considered largely a research device.

Regardless of the respective imaging technique, cardiovascular research is one of the areas receiving the largest scientific interest as of today, which mirrors the fact that cardiovascular disease is the leading cause of death worldwide [159]. Here, different imaging modalities have exhibited a wide range of - partly overlapping - diagnostic ability with respect to clinical markers of cardiac integrity, such as perfusion (PET, MRI, single photon emission tomography (SPECT), CT, Ultrasound), function (MRI, Ultrasound), morphology (MRI, CT), metabolism (PET), viability (PET, MRI) and coronary angiography (CT). Therefore, in the context of integrated PET/MRI imaging, a number of different cardiovascular applications with synergistic potential have been proposed. While many of these, e.g. the assessment of metabolism and function [121] or coronary plaque/inflammatory imaging [122], essentially add clinical examinations from both modalities in an efficient manner, also more complex approaches have been developed e.g. regarding joint motion correction [44]. The latter is especially relevant for PET/MRI, as both respiratory and cardiac motion may degrade PET image quality, for which motion correction may be guided by temporally well resolved morphological MRI information, resulting in a much lower radiation exposure than conceivable corresponding PET/CT techniques.

With respect to synergies in multi-modality imaging, an area that has remained largely unexplored as of today is the absolute quantification of physiological processes. While the clinical value of absolute quantification e.g. in cardiac perfusion imaging is well established for PET [48], MRI techniques allowing for absolute quantification of tissue characteristics have only recently matured to a level of clinical applicability and widespread use. Especially myocardial tissue characterization using quantitative relaxometry - mainly for assessment of T_1 [95] or extracellular volume (ECV) [2] - has received a significant increase in attention over the last couple of years, leading to a higher standardization of techniques across vendors and research sites [94,100]. For MRI perfusion imaging, qualitative analysis of Dynamic Contrast-Enhanced (DCE-) MRI has been shown to be highly effective in the management of patients with coronary artery disease (CAD) [31,51]. However, absolute quantification of tissue perfusion remains challenging both with respect to acquisition and post-processing techniques, despite significant efforts to develop consensus methods tackling the remaining obstacles, e.g. absolute quantification of contrast agent concentrations from MRI signal [73]. Here, especially the understanding for proper kinetic analysis of DCE-MRI data has remained limited, mainly due to its mathematical complexity and the large array of available modeling methods to derive perfusion characteristics from dynamic data [134]. While the corresponding approaches for PET are mainly used to quantify tracer extraction acting as a surrogate for vascular perfusion flow [63,128], it can be seen as one of the great advantages of DCE-MRI that, due to a continuing increase in perfusion data quality and a superior temporal resolution, a host of additional, physiologically

meaningful parameters have come into its scope more recently [16,88]. Still, despite efforts to validate perfusion flow quantification from DCE-MRI with PET [98,102,116], there is a significant lack of methodologically sound assessments of systematic differences between both methods.

Structure of the Thesis

In order to provide the reader with a deeper understanding of the imaging methods, mathematical modeling formalisms, as well as the underlying cardiovascular physiology to be assessed, this introduction is extended by a detailed theoretical review in the next chapter. Applications of the so-described concepts in a clinical setting substantiate the scientific content of this thesis. The individual contributions published as journal or conference papers during the work on this thesis - occasionally extended or altered from the published versions in order to avoid redundancies in the description of methodology - are compiled in Part II of this thesis with each chapter representing a distinct publication.

With respect to the quantification of myocardial perfusion, it is one of the main goals of this thesis to provide an in-depth discussion of methods, both on the MRI side as well as in the context of multi-modality imaging using PET/MRI. The presented studies address some of the most important technical issues in DCE-MRI data analysis with respect to quantitative assessment of microvascular perfusion parameters. In this context, the third chapter proposes an algorithm to determine the measurability of vascular characteristics, which can vary significantly between different physiological perfusion states observed in the myocardium. It additionally reports the validation of perfusion-derived extracellular volume estimates, which has potentially significant implications for scan time and contrast media-dose reduction in cardiac MRI. While the following two chapters address some less prominent aspects in DCE-MRI analysis, such as bolus delay and flow heterogeneity, the sixth chapter features an extensive study on the comparison of perfusion quantification on the basis of simultaneously acquired PET/MRI data. Using the example of perfusion imaging, it can be seen as an effort to establish a paradigm for quantitative multi-modality imaging, rebutting the notion of simple validation in favor of appreciating the existing systematic differences between PET and MRI as an opportunity for synergistic application in the context of basic research. The seventh chapter is a direct continuation of this paradigm into the field of quantitative tissue characterization, featuring a comparison of MRI parameters and inflammatory PET imaging both mutually as well as with blood markers of cardiac pathology. In a similar fashion as the previous section for perfusion, it reports on a combination of PET and MRI imaging results broadening the understanding of both modalities in a way that would not be conceivable outside of an integrated multi-modality context.

It is the hope of the author that - beyond the already significant implications of the individual findings - the approaches presented herein for the combined use of quantitative results from different modalities will serve as an inspiration for future research in multi-modality imaging.

Chapter 2

Theory

2.1 Technical Basics

2.1.1 Nuclear Magnetic Resonance (NMR)

Magnetic resonance imaging is based on nuclear magnetic resonance (NMR), which was first discovered by I.I. Rabi in 1938. The quantum mechanical explanation of NMR phenomena is the fact that all elementary particles have a quantum property called spin, which can be imagined as a quantized, intrinsic angular momentum. Neutrons, protons and electrons as the constituents of matter each have a spin of ½, and are therefore so-called fermions. Depending on the composition of different atomic nuclei, their respective total spin may exhibit different integer or half integer values. While both NMR and MRI experiments can target various nuclei with non-vanishing total spin, imaging is most often performed using the nucleus of hydrogen atoms due to their abundance in the human body within fat and water molecules.

The nucleus of a hydrogen atom consists of a single proton and has a total spin S (or isospin I) of ½. In the classical picture, the proton spin may be imagined as a magnetic dipole moment $\boldsymbol{\mu}$ related to quantum mechanical spin via a so-called gyromagnetic ratio γ:

$$\boldsymbol{\mu} = \gamma \boldsymbol{I} \tag{2.1}$$

A magnetic quantum number m_I indicates the state of the spin moment. For the hydrogen nucleus, i.e. a proton, m_I may only assume the two discrete values +½ and -½, leading to a two-state system which is as such energetically degenerate. This degeneracy may be lifted by the presence of a magnetic field (usually called B_0-field) interacting with the magnetic dipole property of the hydrogen nucleus and energetically favoring one of the two previously degenerate states. With a magnetic field of magnitude B_0 pointing along the z-axis, the magnetic energy of the proton is given by:

$$E = -\boldsymbol{\mu} \cdot \boldsymbol{B_0} = -\gamma I_z B_z = -\gamma m_I \hbar B_0 \tag{2.2}$$

With the so-called Larmor frequency ω_0, the energy difference between the two states is:

$$\Delta E = \gamma \hbar B_0 := \hbar \omega_0 \tag{2.3}$$

For protons, depending on the magnetic field strength, this energy gap lies within the radio frequency (rf) spectrum, e.g at around 128 MHz at a B_0-field of 3 Tesla. Since all

standard NMR and MRI experiments are applied across macroscopic volumes, the statistical concept of magnetization needs to be introduced, which is defined as the sum of all magnetic moments per volume V:

$$\boldsymbol{M} = \frac{1}{V} \sum_{\boldsymbol{\mu}\, in\, V} \boldsymbol{\mu} \tag{2.4}$$

Assuming a large ensemble of spins residing inside a magnetic field across the z-direction, the rotating expectation values of the x- and y-components of different moments cancel in summation, leaving $\boldsymbol{M}$ with a component only along the z-direction. In thermal equilibrium, the probability of magnetic spin moments to populate either of the two energetic states is determined by Boltzmann statistics. At room temperature, the net magnetization in z-direction arising from a higher probability to populate the energetically lower state is [55]:

$$\frac{P_+}{P_-} = \frac{Ze^{(\frac{E_+}{k_B T})}}{Ze^{(\frac{E_-}{k_B T})}} = e^{(\frac{\hbar\omega_0}{k_B T})} \simeq 1 + 6.6 \cdot 10^{-6} \cdot B_0 \tag{2.5}$$

Equation 2.5 implies that the macroscopically observable excess magnetization that is used to generate MR signals corresponds to a polarization of only a few in a million protons, depending on B_0-field strength. The process of manipulating this net magnetization via application of additional rf-fields (often called B_1-fields) is the basis for all NMR and MRI applications. Such excitation of $\boldsymbol{M}$ from its equilibrium state by external fields has essentially two effects: A rotation of $\boldsymbol{M}$ about the direction of $\boldsymbol{B_1}$ as well as a subsequent precession of $\boldsymbol{M}$ about the direction of $\boldsymbol{B_0}$. The term nuclear magnetic resonance describes the fact that the frequency of this precession is the Larmor frequency ω_0, which is the same frequency that was used with $\boldsymbol{B_1}$ during the initial excitation. A full inversion of the thermal equilibrium state corresponds macroscopically to a rotation of the magnetization vector by 180°. Depending on the strength and duration of exposure to the rf-field, $\boldsymbol{M}$ may be rotated by any angle between 0° and 180°.

Relaxation of a non-equilibrium state induced by $\boldsymbol{B_1}$ is the core observation in essentially all magnetic resonance experiments. The relaxation of excited states in NMR is the combined effect of two different phenomena: The first channel of relaxation is the decay of the transversal magnetization component $M_\perp$, visualized e.g. with a free induction decay (FID) experiment (Fig. 2.1). It is associated with the time constant T_2 and can be explained as a loss of coherence in precession phases of spins due to interactions with the magnetic fields of other spin moments. This so-called spin-spin relaxation is further accelerated by potential inhomogeneities in the B_0-field, leading to the definition of an additional constant $T_2^{'}$. The resulting relaxation time constant is called T_2^* and is given by:

$$\frac{1}{T_2^*} = \frac{1}{T_2} + \frac{1}{T_2^{'}} \tag{2.6}$$

The second channel of relaxation corresponds to the loss of energy of the spin system to the surrounding tissue, and can macroscopically be imagined as a regrowth of the longitudinal magnetization component M_z. This so-called spin-lattice relaxation is associated

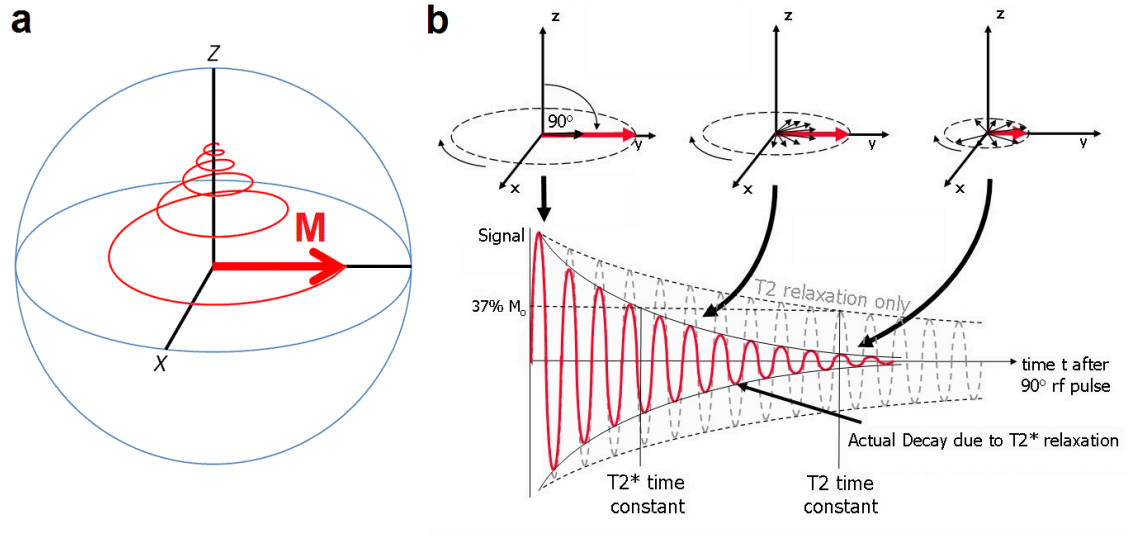

Figure 2.1: Free induction decay after application of a 90° pulse with the tip of the magnetization vector shown while returning to equilibrium (**a**). A corresponding induction signal that would be recorded with a coil placed around the x-axis is shown in (**b**).[1]

with the time constant T_1. Both relaxation constants may be equivalently expressed in terms of rates (R) or times (T), with $R_{1/2}$ equal to $1/T_{1/2}$. The fundamental equation governing precession and relaxation of the magnetization vector $\boldsymbol{M}$ with magnitude M_0 inside a magnetic field $\boldsymbol{B}$ is the Bloch equation:

$$\frac{d\boldsymbol{M}}{dt} = \gamma \boldsymbol{M} \times \boldsymbol{B} + \frac{1}{T_1}(M_0 - M_z)\hat{e}_z - \frac{M_\perp}{T_2^{(*)}} \tag{2.7}$$

For a static B-field in z-direction, this simplifies to:

$$\frac{dM_z}{dt} = \frac{1}{T_1}(M_0 - M_z) \tag{2.8}$$

$$\frac{dM_\perp}{dt} = -\frac{M_\perp}{T_2^{(*)}} \tag{2.9}$$

In order to observe the relaxation phenomena described by these equations, a coil can be placed around one of the transversal axes. As soon as the magnetization is excited to the effect of having a nonzero transversal component, its rotation around the z-axis induces a current inside the coil which can be detected as a signal. On the right hand side of Fig. 2.1, the basic structure of such a signal is depicted after the application of a 90° rotation to the equilibrium magnetization.

A technique that is fundamental to MR experiments is the formation of spin echoes or gradient echoes. A so-called spin echo is formed by the application of a 180° rotation after

[1] Image (**a**) reproduced with permission from [153]. Image (**b**) reproduced with permission from [118], originally published by SpringerOpen.

initially rotating the magnetization by 90° and subsequently waiting for a time $T_E/2$. During the so-called echo time T_E, spin populations are allowed to dephase before the 180° pulse again reverses their current phase relation, leading them back to coherence (Fig. 2.2(a)). The 180° pulses also reverse the effects of inhomogeneities in the external B_0-field, making the strength of the echo signal depend on T_2.

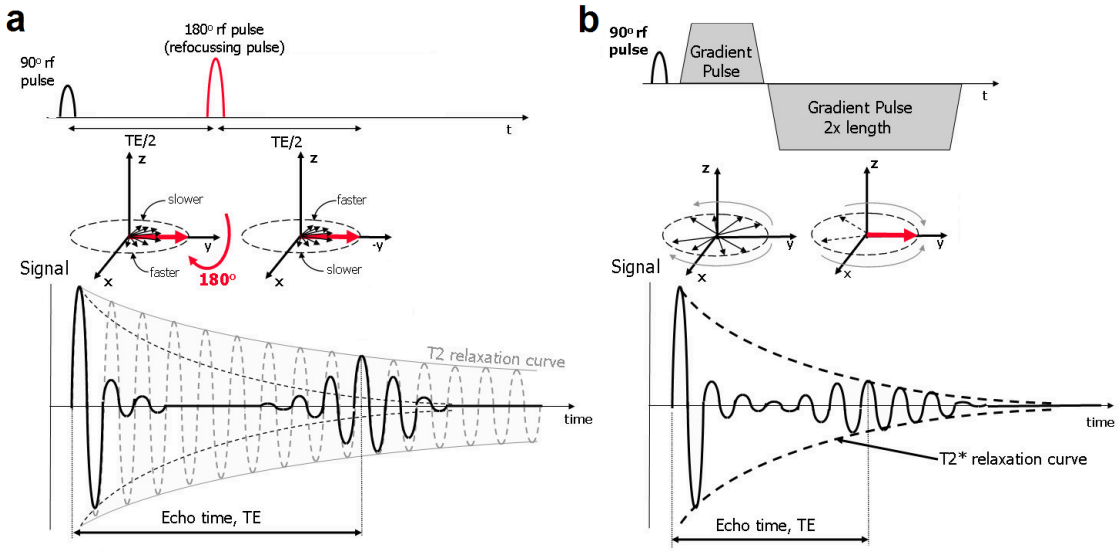

Figure 2.2: Two ways of creating a signal echo: A spin echo reversing the effects of external magnetic field inhomogeneities (**a**) and the creation of a gradient echo with signal decay depending on T_2^* (**b**).[2]

This reversal of inhomogeneities is not possible with so-called gradient echoes, which is why their signal decay is determined by T_2^*. A gradient echo is formed by the application of spatially dependent magnetic field gradients in addition to the main B_0-field. The first gradient (the dephase lobe) artificially destroys the phase coherence of spins so that after it is turned off, every spin has acquired a phase which is exclusive to its spatial residence within the gradient field. The second part of the gradient configuration (the rephase lobe) is of the same strength but twice as long and has opposite polarity. It may be switched on almost immediately after the dephase lobe is turned off, reversing its effect and thus creating a signal echo at time T_E with a peak at the center of the rephase lobe (Fig. 2.2(b)). The switching of gradient polarities occurring at $T_E/2$ cannot happen instantaneously due to a finite latency of the gradient coils caused by their inductance. This latency (or slew rate) is one of the fundamental technical limits of speed in MR applications.

2.1.2 Magnetic Resonance Imaging (MRI)

The key to MR imaging is the acquisition of information about the described NMR phenomena and relaxation constants in a spatially resolved manner. An MR imaging setup is

[2]Images (**a**) and (**b**) reproduced with permission from [118], originally published by SpringerOpen.

depicted schematically in figure 2.3 with the patient lying along the z-axis being also the axis of the B_0-field.

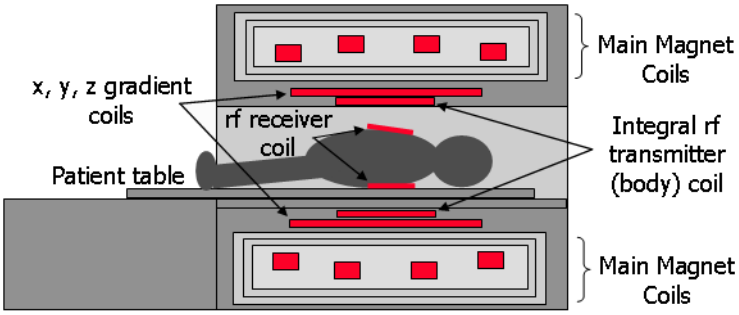

Figure 2.3: Basic setup of a clinical MRI system. A schematic depiction of the coil arrangement inside the system is shown consisting of coils for the main magnet, gradients, as well as rf-field transmission and reception.[3]

The basis for spatial encoding is the application of spatially dependent magnetic field gradients in addition to the main B_0-field. Across a limited extension, these gradients result in an effective magnetic field that varies close to linearly along potentially all three spatial directions. For the duration of gradient application, every spin moment is assigned with a precession frequency that is dependent on its position on the corresponding axes and is therefore accumulating a phase difference with respect to spins in other locations. Using this principle, an example for the generation of images can be given for a 2D imaging approach as follows: Magnetization from a single transversal slice covering the x-y plane may be excited by application of a linear magnetic field gradient in z-direction during the rf-excitation, with the rf-frequency of the excitation pulse chosen to match the frequency belonging to the desired z-position. Spatial encoding of the signal in the remaining two dimensions is achieved by introduction of so-called k-space. The axes of k-space form a coordinate system in which every point corresponds to the density of spins ρ in all points (or voxels) of real space that have accumulated the same phase due to the magnetic field gradients along x- and y-axes. For a regular Cartesian sampling of k-space, the G_x-gradient can be used for acquisition of a gradient echo signal representing information about one line of k-space along the k_x-axis. The vertical placement of that line is determined by the phase assigned to it by the gradient field G_y. With τ_y being the time that G_y is applied, it is:

$$k_x(t) = \gamma G_x t \qquad and \qquad k_y(\tau_y) = \gamma G_y \tau_y \tag{2.10}$$

The resulting signal is given by the so-called imaging equation (Eq. 2.11) for the 2D case, connecting the density of protons ρ in real space with the corresponding signal values in k-space via a 2D Fourier transformation between the variables $\boldsymbol{r}$ and $\boldsymbol{k}$.

$$S(\boldsymbol{k}) = \mathcal{FT}\left[\varrho(\boldsymbol{r}, z_0)\right] = \iint \varrho(x, y, z_0) e^{-2\pi i(k_x x + k_y y)} dx\, dy \tag{2.11}$$

[3]Image reproduced with permission from [118], originally published by SpringerOpen.

According to this equation, MR images, i.e. spatially resolved information about the spin density ρ, can be obtained by application of an inverse Fourier transform to the recorded MRI signal $S(\boldsymbol{k})$, which represents the spectrum of accumulated precession phases in the sample. The nature of this encoding process has facilitated the development of an enormous variety of strategies to sample and reconstruct k-space in both 2D and 3D imaging applications. The MRI sequences used for imaging in this thesis all use the described cartesian sampling approach based on gradient echoes. They employ Fast Low Angle Shot (FLASH) [56] techniques with either spoiled or preserved transverse magnetization coherences.

As seen in Fig. 2.3, rf transmit and receive coils are usually separated, resulting in a large body transmit coil for more homogeneous excitation and smaller receive elements as close as possible to the imaging target for an improved signal-to-noise ratio (SNR). Concerning signal reception, especially cardiac applications have benefited significantly from the introduction of array coils with multiple coil elements. These allow for time-saving undersampling of k-space by making use of redundancies in information gathered from spatially overlapping coil signals, e.g. in the form of Generalized Autocalibrating Partially Parallel Acquisitions (GRAPPA) [53].

2.1.3 Gadolinium-based MRI Contrast Agents

Despite the large variety of possibilities to achieve image contrast in MRI, a number of applications benefit from the use of additional exogenous contrast agent (CA). Essentially all clinically accepted agents rely on the paramagnetic properties of Gd^{3+}-ions. As Gd^{3+} has seven unpaired electrons in parallel spin configuration, its magnetic susceptibility is significantly higher than that of normal protons. In MRI experiments, the strong resulting paramagnetic dipole field may act as a local field inhomogeneity, which accelerates relaxation implying a shortening of T_1 and T_2^* times.

For clinical administration, Gd^{3+} needs to be combined with a chelate acting as a shell around the ion due to its high toxicity. The purpose of the chelate is to effectively inhibit any physiological interaction of the Gd^{3+}-ion until it is excreted via the kidneys. Two classes of clinically established chelates for Gadolinium exist, which are called linear and macrocyclic. Based on linear chelation, gadopentetic acid (Gd-DTPA) was the first compound to be accepted for clinical usage [25], while the most widely-used agent with macrocyclic chelation is gadoteric acid (Gd-DOTA) (Fig. 2.4). Despite being well tolerated and excreted rapidly by the vast majority of patients, the association of Gd-DTPA administration with Nephrogenic Systemic Fibrosis (NSF) in end-stage renal disease [54] has prompted ongoing investigations on the long-term retention and stability of Gd-based compounds. A number of studies since then have investigated the disassociation of Gadolinium from its chelate, which is believed to be the main pathogenic effect, suggesting a generally higher in-vivo stability of macrocyclic compared to linear chelation [101,113,133].

The structure formula for Gd-DTPA depicted in Fig. 2.4(a) shows the addition of a water molecule to the compound, attached directly to the Gd^{3+}-ion by a coordinative bond. This bond provides the spatial vicinity needed for efficient dipole-dipole interaction between water protons and the Gd^{3+}-ion. Protons at the binding site are relaxed very rapidly, making the magnetic relaxation of a whole volume of water effectively depend

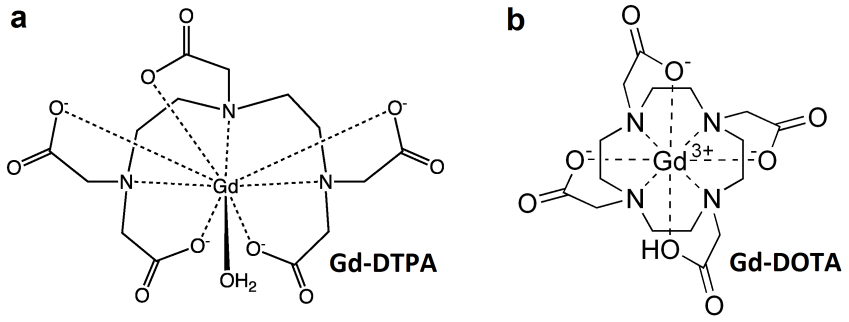

Figure 2.4: Chemical structure formulae for the most widely-used MRI contrast agents Gd-DTPA based on linear chelation (**a**) and Gd-DOTA based on macrocyclic chelation (**b**).[4]

on the rate at which the water molecule at the binding site is being exchanged. This rate is determined by the ability of water to move within its molecular context, effectively making it a tissue property, and the potential impact of macromolecular content on the relaxation properties of Gd-based compounds within tissue have been documented [137]. Quantitatively, the influence of MRI contrast agents on T_1 and T_2^* relaxation is usually condensed into a single global constant ($r_{1/2^*}$) called relaxivity. With $R_{1/2^*,0}$ as the native relaxation rate and [Gd] as the local concentration of the contrast agent, it is:

$$R_{1/2^*} := \frac{1}{T_{1/2^*}} = R_{1/2^*,0} + r_{1/2^*} \cdot [Gd] \tag{2.12}$$

Concerning biodistribution, the described molecules are mainly bound to the vasculature [4], although their relatively small size allows permeation of vascular walls and therefore leakage into the interstitial tissue space (or equivalently, the extravascular-extracellular space (EES)) for a number of organs including the heart. However, no Gd-based agent is able to move across intact cellular walls, leading e.g. to a relative myocardial distribution volume for Gd-DTPA/Gd-DOTA of about 25% of the whole tissue space. Although agents that distribute almost exclusively intravascular have been developed for clinical use, their effectiveness for dynamic or quantitative applications is limited, as intravascularity usually depends on reversible albumin binding, potentially changing the kinetic properties of the agent itself during dynamic experiments.

With respect to the relative distribution volume of MRI agents, it is also important to introduce the distinction between what is commonly called a tracer and an indicator: While tracers usually both represent the imaging target and beget the image signal - e.g via radioactive decay in PET - indicators only passively report on the presence of the imaging target, i.e. water protons in the case of MRI. The fact that MRI indicators are usually confined to the extracellular space while the water molecules creating the actual image signal may move between all tissue subspaces introduces the necessity to consider so-called water exchange effects. For a tissue voxel containing two subspaces (a,b), the impact of water exchange on MRI signal is proportional to the relationship between water exchange rates across their border and the difference in their magnetic relaxation rates. The basic

[4]Images adapted from [156] (**a**) and [155] (**b**).

mathematical framework for the treatment of exchange effects was given by Hazlewood et al. [59] and later adapted for sequences mapping R_1 recovery after inversion [40]. For the two extreme cases - the so-called fast-exchange (FEXL) and no-exchange limits (NEXL) - normalized signals after an inversion time T_I from a voxel comprising two subspaces with relative volumes $v_{a/b}$ and relaxation rates $R_{1,a/b}$ may be written as:

$$S^{FEXL}(T_I)/M_0 = 1 - 2e^{-T_I(v_a R_{1,a} + v_b R_{1,b})} \tag{2.13}$$

$$S^{NEXL}(T_I)/M_0 = v'_a(1 - 2e^{-T_I R'_{1,a}}) + v'_b(1 - 2e^{-T_I R'_{1,b}}) \tag{2.14}$$

In the fast-exchange limit, water protons move rapidly between subspaces making them subject to a single, effective R_1 that is a weighted average of R_1 rates within the two subspaces (Eq. 2.13). In the case of limited or no water exchange, each subspace contributes to the voxel signal with a separate exponential, depending on a set of apparent (primed) relative volumes and relaxation rates (see [40] for details). While limited exchange implies the possibility to estimate relative volumes of subspaces from a bi-exponential fit according to Eq. 2.14, it complicates the estimation of absolute CA concentration from MRI voxel signal. For this process, Eq. 2.12 is applicable to a mixed voxel-signal only when assuming the FEXL, in which a single effective R_1 exists that is linearly proportional to indicator concentration within the respective subspace.

Whether the FEXL applies depends to a large degree on the MRI sequence with which exchange effects are sampled. For common gradient-echo sequences, short repetition times reduce exchange sensitivity and may fully alleviate them if certain conditions are met [40]. The main problem for contrast-enhanced imaging in this context is that agents may introduce very large differences in R_1 between tissue subspaces, and therefore may violate the FEXL independent of the physiological water exchange rate. Especially for dynamic imaging, which involves the tracking of a high-concentration indicator bolus through the tissue, water exchange effects have been extensively discussed in the literature. For intravascular indicator behavior, e.g. cerebral applications of Gd-DTPA, the FEXL is measurably violated between vascular and extravascular tissue compartments [70]. In the case of significant extravasation, e.g. in cardiac applications of Gd-DTPA, effects of both vascular/interstitial [18] and interstitial/cellular [88] water exchange have, however, been shown to be not measurable using gradient echo sequences with short T_R.

2.1.4 Positron Emission Tomography (PET)

Positron emission tomography imaging relies on the application of short-lived isotopes whose decay invokes the emission of a positron (β^+) as part of the conversion of protons into neutrons:

$$^1_1p^+ \rightarrow {}^0_1n + {}^1_0\beta^+ + \nu \tag{2.15}$$

Such isotopes may be chemically substituted into a large variety of different biological molecules which may act as tracers to a potentially vast amount of metabolic or functional processes. The radiotracers used in this thesis belong to the most widely used ones in medicine today, namely the glucose analogue F18-fluorodeoxyglucose (^{18}F-FDG) and the

ammonia analogue $^{13}NH_3$. The decay equations for fluorine and nitrogen isotopes are given below, half-lives are about 110 min and 10 min respectively.

$$^{18}_{9}F \rightarrow {}^{18}_{8}O + {}^{1}_{0}\beta^{+} + \nu \tag{2.16}$$

$$^{13}_{7}N \rightarrow {}^{13}_{6}C + {}^{1}_{0}\beta^{+} + \nu \tag{2.17}$$

After injection of a radiotracer into the human body, the emitted positrons perform elastic and inelastic collisions with atomic electrons or nuclei of surrounding matter. When kinetic energy is reduced far enough the positron combines with an electron, resulting in annihilation either directly or via the formation of a short-lived positronium system. The eventual annihilation produces two photons with an energy of 511 keV, usually emitted with a relative angle of 180° according to the conservation of momentum. The synchronous detection of theses photons is the basic imaging signal of PET, corresponding however to detection of the annihilation event rather than the location of the original isotope/radiotracer decay. The positron range between emission and annihilation events is one of the fundamental limits of spatial resolution in PET imaging, being at about 0.6 mm for ^{18}F and 0.9 mm for ^{13}N in tissue [87].

In order to locate the positron annihilation, both photons need to be detected by detectors on opposing sides across a so-called line of response (LOR). The most commonly used (block) detectors are a combination of an array of scintillation crystals in front of a photodetector. The main scintillator material interacts with incoming annihilation photons via Compton scattering events. The concomitant energy deposition creates electron-hole pairs that in turn interact with targeted crystalline impurities (activators), ultimately producing photons in the range of visible light. Photodetectors process the incoming scintillation photons into an electrical current of photo-electrons. They consist either of standard photomultiplier tubes (PMTs) or semiconductor-based photomultipliers such as avalanche photodiodes (APDs) and silicon photomultipliers (SiPMs).

In the so-described detection process, precise timing on the order of a few nanoseconds is necessary to sufficiently identify coinciding detection events. In addition to the so-called true coincidences recorded for LORs passing through the actual point of annihilation, the finite time resolution of detection as well as scattering of annihilation photons may also lead to random coincidences and scattered coincidences. Especially the latter is a major contributor to image noise in medical scanners, and widely-used methods for scatter correction exist [146].

Quantitative estimation of activity from PET image data relies on another pre-reconstruction step which is called attenuation correction (AC). In any extended object, the path lengths for annihilation photons passing through media that may absorb them before detection can vary significantly. The probability of absorption also depends on the material that is passed through, and is e.g. much higher in bone than in mostly air-filled lung tissue. Attenuation correction refers to the process of estimating for each LOR the probability that both photons from a preceding annihilation event are actually detected, and subsequently normalizing detection events across all LORs to these probabilities. The necessary information about the variation of the attenuation coefficient μ within the sample

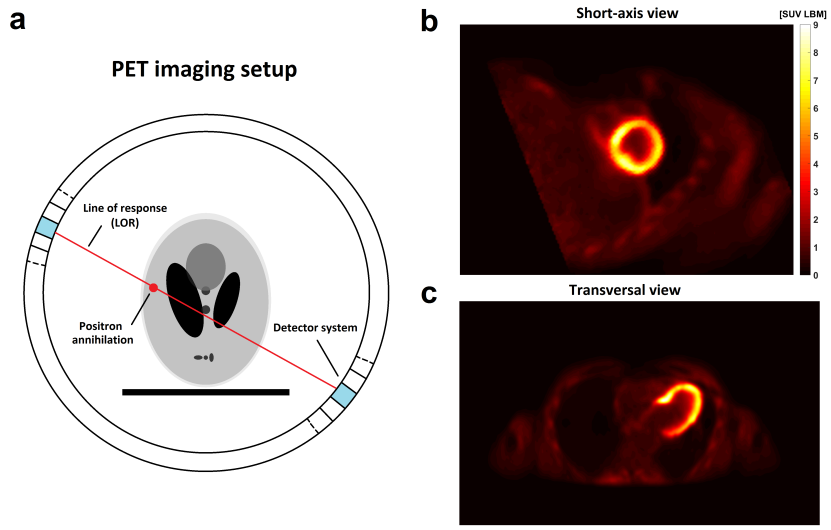

Figure 2.5: Visualization of the basic PET imaging principle. In (**a**) a schematic PET imaging setup is shown, consisting of a detector ring designed to detect annihilation photons across a LOR. Placing of the annihilation event inside the subject (here: a Shepp-Logan phantom) determines the photon path through different tissue types and therefore the probability to be detected at the corresponding side of the detector. Examples for 2D short-axis (**a**) and transversal (**b**) slices from a 3D ^{18}F-FDG PET image are shown in units of SUV LBM with prominent tracer uptake in the myocardium.

is recorded in most clinical scenarios, i.e. with combined PET/CT devices, using a low-dose CT scan [78].

The so-corrected PET data may be reformatted before image reconstruction into a number of recorded coincidence events populating a set of projection lines. In 2D, these projection lines represent the integration of events across all LORs under a certain projection angle ϕ, leading to a sinogram or Radon transform data format $p(s, \phi)$. Akin to computed tomography, the most basic reconstruction algorithm for such projection data is the so-called backprojection or tomographic reconstruction. For a 2D case with $f(x, y)$ as the distribution of activity in the volume of interest, it is:

$$f(x,y) = \frac{1}{2\pi} \int_0^{\pi} p(x\,cos(\varphi) + y\,sin(\varphi), \varphi)\, d\varphi \tag{2.18}$$

Due to the higher density of data in the center of sinogram space, direct reconstruction according to Eq. 2.18 is applied in combination with weighting filters as a filtered backprojection (FBP). Because such filters usually create undesirable noise patterns, most of the clinically applied reconstruction frameworks rely on iterative, numerical reconstruction algorithms such as Ordered Subsets Expectation Maximization (OSEM) [62]. One of the main differences of PET data to MRI is that the acquisition process is inherently continuous and three-dimensional, and certain time windows of the whole acquired raw dataset may be reconstructed separately, e.g. for dynamic imaging.

Concerning the quantitative representation of image data in PET, basic intensity values after reconstruction are usually given as an activity I in units of Bq/mL, which is equivalent to the number of recorded decay events per second per milliliter. Both for dynamic imaging as well as for the calculation of a so-called standardized uptake value (SUV), decay correction specific to the radioisotope is executed based on the difference between the time of injection and image acquisition. The SUV can be seen as a measure of deviation from equal dose distribution to all organs and is mostly used in ^{18}F-FDG applications (Fig. 2.5). It is calculated at a time point t after injection using the injected dose ID and the body mass BM or alternatively the lean body mass LBM of the subject, yielding either SUV or SUV LBM:

$$SUV(t) = \frac{I(t)}{ID/BM} \qquad and \qquad SUV\ LBM(t) = \frac{I(t)}{ID/LBM} \tag{2.19}$$

2.1.5 PET/MRI

The clinical success of integrated PET/CT scanners and the ability of MRI with respect to soft tissue contrast and reduction of exposure to ionizing radiation has inspired the development of combined PET/MRI scanners. With respect to the technical aspects of both systems as outlined in the preceding sections, a number of additional obstacles needed to be overcome. As dynamic magnetic fields have strong detrimental effects on the operation of PET detector hardware based on PMTs, development of detector systems that are not influenced by magnetic fields was crucial. The use of semiconductor-based photodetectors, first realized for pre-clinical system using APDs [27], has led to the first clinical systems based on APDs [35] and more recently using SiPMs [50]. Conversely, proper shielding of PET detector hardware is necessary in order to diminish their influence on magnetic field homogeneity. With respect to MRI hardware, also the design of patient beds and surface coils changed to move as much of electronics or otherwise attenuating material out of the PET bore. A detailed assessment of performance aspects for both PET and MRI subsystems of the integrated clinical PET/MRI scanner system used in this thesis has been published in [35].

With respect to quantitative applications, the generation of reliable μ-maps is more demanding than for PET/CT, where the basic image signal of the CT is essentially the attenuation coefficient (apart from differences in photon energy). For abdominal and cardiac PET/MRI applications, the most widespread approach is a fat-water separation (Dixon-) technique [39] from which tissue-types may be classified and assigned with known attenuation values. Still, truncation artifacts from the limited field of view across which the MRI can estimate attenuation remains challenging especially for whole-body applications [10]. Also cerebral applications are relying on further development of ultra short echo time (UTE) sequences capable of generating MRI signals from highly attenuating bone structures exhibiting very short T_2^* times [26].

2.2 Cardiovascular Physiology and Blood Flow

This section introduces aspects of basic cardiac physiology with specific relevance to the topic of this thesis, focusing on the coronary circulation and the physiology of microvascular perfusion as well as pathologies associated with it.

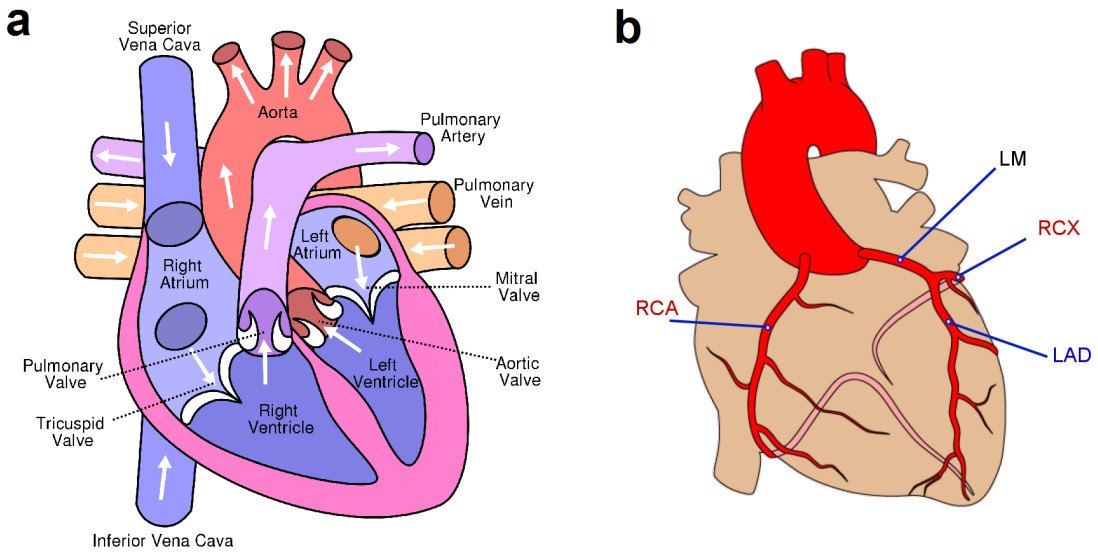

Figure 2.6: Idealized physiology of the human heart. An inside view of the large vessels and four chambers of the heart with arrows indicating the direction of blood flow is shown on the left (**a**), the heart muscle (myocardium) is magenta. On the right (**b**) is an outside view of the heart showing the course and origin of the three large epicardial arteries supplying blood to the microvasculature inside the myocardium. It is RCA = right coronary artery, LAD = left anterior descending artery, LCx = left circumflex and LM = left main stem.[5]

The human heart as depicted in Fig. 2.6 is best idealized as a system of tubes and chambers designed to move deoxygenated blood through the lungs (via the pulmonary vessels) and subsequently distribute oxygenated blood via the left ventricle (LV) and the aorta into the rest of the body. Like every other muscle inside the human body, the heart muscle itself - represented by the contractible walls of the two ventricles - needs blood supply. This blood supply is provided by the so-called coronary circulation. It consists of the coronary veins and arteries constituting a system of vessels within the myocardium and on its outer surface. The coronary arteries have their origin at the aortic root just downstream of the aortic valve. The arterial coronary vasculature may be divided into functional subgroups by vessel diameter [23]. It consists of the macroscopic epicardial arteries (>0.5 mm) as well as the microvasculature within the tissue, consisting of prearterioles (0.5 - 0.1 mm), arterioles (<0.1 mm) and capillaries. The capillaries represent the main functional unit of tissue perfusion as pertaining to oxygen and nutrient exchange across the vascular walls.

[5]Image (**a**) reproduced from [160]. Image (**b**) reproduced from [157], © R.C.B. Kreuger and ECGpedia.org.

There is a complex mechanical (prearterioles) and metabolic (arterioles) regulation of flow resistance and thus microvascular blood flow in the myocardium (Fig. 2.7, left). The purpose of this regulation is to at all times meet the perfusion demand of the heart muscle, while at the same time maintaining a pressure gradient along the vascular hierarchy to protect the sensitive capillaries from high systemic blood pressure.

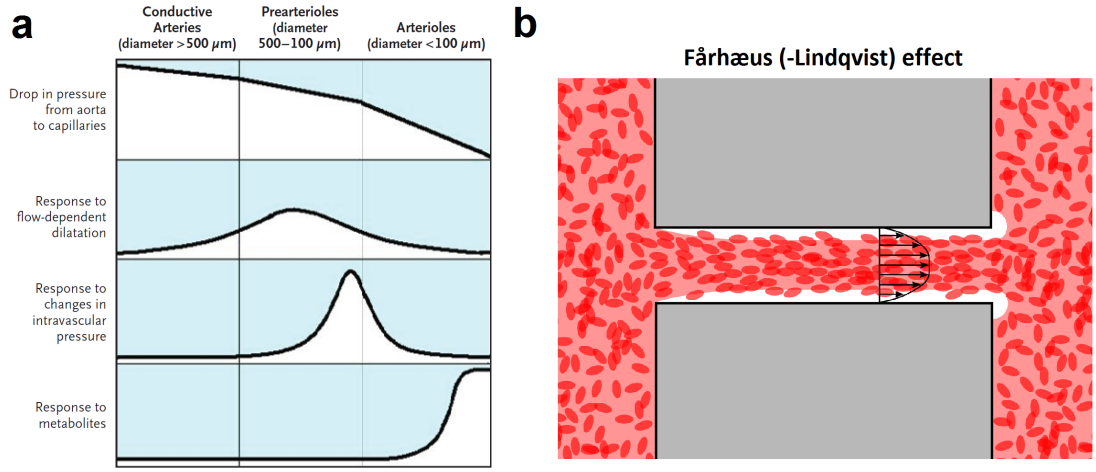

Figure 2.7: Characterization of perfusion on a microvascular level. Plot (**a**) shows functional subunits of the arterial coronary vasculature in a hierarchical fashion, highlighting the physiological pathways of pressure regulation. On the right (**b**), Fårhæus- and Fårhæus-Lindqvist effects are visualized, depicting a drop in blood viscosity by phase separation of blood and plasma in the microvasculature as well as a concomitant drop in tube hematocrit.[6]

With respect to blood flow, the drop in pressure is partially compensated for by a decrease in overall blood viscosity with decreasing vessel diameter called the Fårhæus-Lindqvist effect [41]. It describes the observation that, at small tube diameters, red blood cells and plasma flow patterns separate, resulting in a cell-free layer at the inner vessel wall where laminar shear resistance is greatest (Fig. 2.7, right). While the resulting drop in overall blood viscosity is called Farhaeus-Lindquist effect, the concomitant drop of effective tube hematocrit, i.e. the volumetric ratio of vascular cell to plasma content, is usually referred to as the Farhaeus effect. Both Fårhæus- [81] and Fårhæus-Lindqvist effects [114] have been observed in-vivo, although differing accounts on their strength and interplay with the general physiological state exist [5,115].

An additional factor that is assumed to play an important role in the regulation of oxygen delivery in the myocardium is the local heterogeneity of flows within a single vascular bed. Evidence for both the heterogeneity itself as well as its change during vasodilator stress has been documented early on in animal studies [32,124]. The basic concept of how heterogeneity of flow rates in a given vascular bed, equivalently expressed as capillary transit

[6]Image (**a**) reproduced with permission from [22], © Massachusetts Medical Society. Image (**b**) adapted from [154], © R. Hellmuth.

time heterogeneity (CTH), influences the average efficacy of oxygen extraction (OEF) is depicted in Fig. 2.8.

It shows that the maximum achievable diffusion of oxygen from a single exchanging vessel increases sub-linearly with flow according to the flow-diffusion equation. This implies that the most efficient way in which a given vascular bed can facilitate oxygen extraction at a given average flow rate is by exhibiting a completely homogeneous flow distribution across all pathways it contains. It also implies that - theoretically - the most efficient way to adapt to an increase in oxygen demand includes both an increase of overall flow and a homogenization of capillary flow patterns (Fig. 2.8(b)) [109].

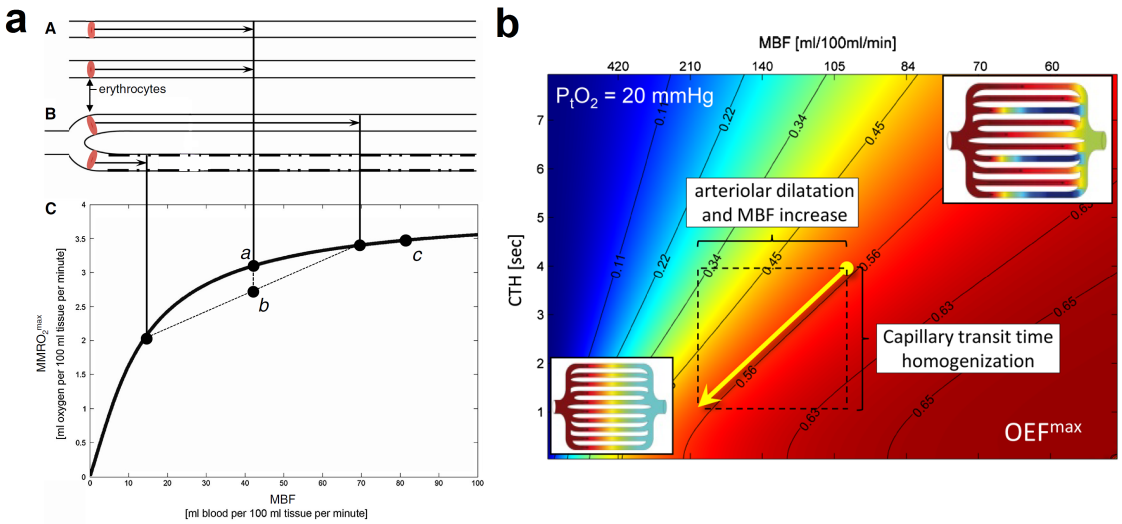

Figure 2.8: Visualization of the effects of flow heterogeneity on oxygen extraction. (**a**) The graph on the left shows diffusion of oxygen - expressed as an upper limit to the maximal metabolic rate of oxygen ($MMRO_2$) - with a sub-linear relationship to blood flow along a single vessel as predicted by the flow-diffusion equation. The subsequent difference in achievable oxygen extraction between homogeneously (A) and heterogeneously (B) perfused vascular beds is indicated by the difference between points (a) and (b). (**b**) The plot on the right is a 2D representation of the graph on the left with a continuous scale of average blood flow (MBF) and CTH for a hypothetical vascular bed.[7]

The described system of cardiac perfusion can be affected by disease on a number of different levels, which may manifest as life-threatening acute insults or gradual alterations of vascular or overall tissue structure. The most prevalent disease associated with cardiac perfusion is coronary artery disease, which describes the narrowing of macroscopic coronary arteries due to calcification or atherosclerotic plaque. The actual impact of CAD on tissue perfusion may vary depending on its location and whether downstream tissue is sufficiently supported (collateralized) by other arteries. An acute ischemic event, i.e. occlusion of a major coronary vessel, is the most dramatic complication from CAD. It results in a complex biochemical cascade inducing edematous-inflammatory processes in the short-

[7]Images (**a**) and (**b**) adapted with permission from [109], originally published by Springer.

term and fibrotization of myocardial tissue or ventricular remodeling in the long-term. The main effect on tissue composition consists of a gradual exchange of formerly intact cellular tissue content with fibroblasts, effectively increasing the relative volume of the extracellular matrix.

Somewhat separate from the simple clinical picture of macrovascular obstruction and downstream ischemia associated with CAD, a number of overall less-well understood disease patterns associated with morphologic or functional alterations of the microvasculature are collectively referred to as either microvascular disease (MVD) or coronary microvascular dysfunction (CMD). They may manifest as both symptoms or risk factors to a number of other disease processes [22], and may in some instances be seen as underlying explanations for ischemic alterations in tissue structure in the absence of large-vessel CAD [33]. While a number of scenarios for ischemic disease processes that are only determined by functional alterations to the microvasculature are theoretically conceivable [109], direct observation of cause and effect is not as easily achievable as for macroscopic CAD.

2.3 Myocardial Perfusion Imaging

2.3.1 Generic Perspective

The main purpose of perfusion imaging is the visualization of vascular tissue space, which refers to the hierarchy of microscopic vessels that due to their small size escape direct visualization by angiography techniques. A contrast with respect to perfusion is usually created both in time and space by administration of a bolus of external contrast agent, whose distribution is monitored by observing dynamic signal changes of the tissue space as a whole. All major clinical imaging techniques (MRI, CT, PET, SPECT, ultrasound) have established protocols for perfusion imaging that may vary in applicability with respect to the organ of interest.

The main motivation behind the development of myocardial perfusion imaging has been assessment of the very prevalent and potentially life-threatening CAD, for which cause (coronary obstruction) and effect (ischemic tissue) are somewhat spatially separated. While the presence of calcifications in the large arteries may be visualized by invasive angiography or non-invasive by CT, their effect both with respect to location and severity of ischemia cannot readily be deduced from angiographical data. Conceptually, perfusion imaging fills this gap in information and may, from a clinical point of view, act as a gatekeeper to the prescription of more expensive invasive angiography diagnostics or recanalisation therapy. In addition to its relevance in estimating the severity of known or suspected CAD, direct assessment of tissue perfusion may yield information on vascular pathology that only manifest microscopically and - depending on the biodistribution of the agent - also characterize tissue properties associated with CA distribution beyond perfusion flow.

In a clinical setting, the ability of the vasculature to adapt to high demands during physical stress is often tested by simulating a stressed state via patient exercise or administration of a pharmacological vasodilating agent. An attenuated reaction to stress, implying that some part of the coronary vasculature is limiting the accommodation of perfusion flow to a state of high energy demand, is considered an indicator of ischemia. Ischemia due to pathologic narrowing of a single epicardial artery (single-vessel disease)

may be detected by any qualitative technique yielding a perfusion contrast. One of the main clinical motivations for absolute quantification of perfusion information is the fact that ischemia may also present itself as a globally balanced effect, e.g. in three-vessel disease or microvascular disease, for which diagnosis requires the comparison of quantitative perfusion information to some absolute reference standard.

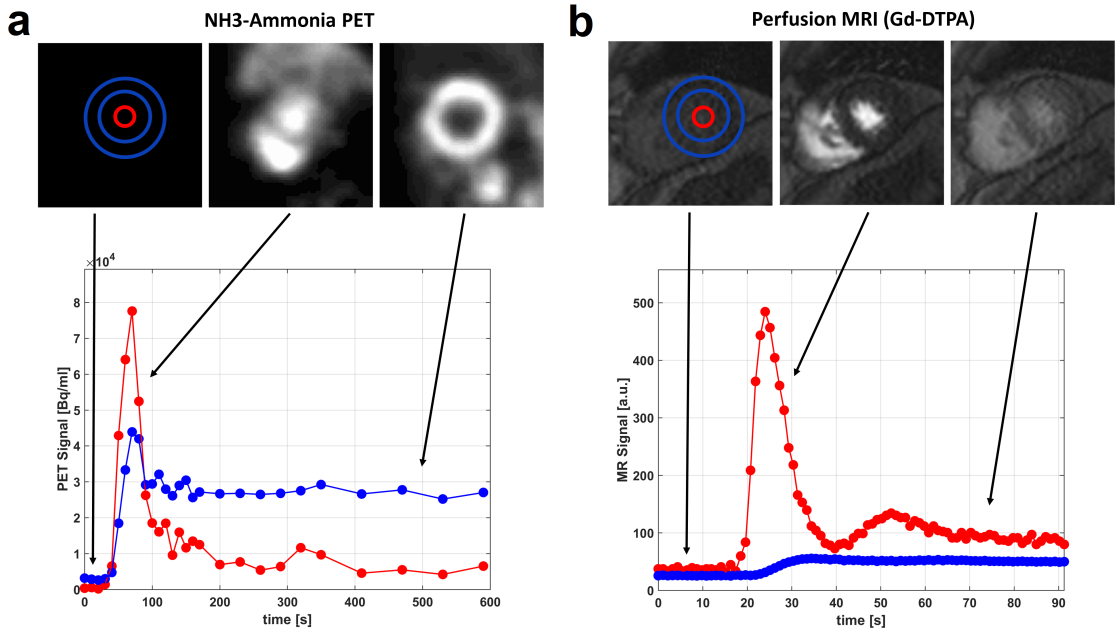

Figure 2.9: Bolus passage and corresponding enhancement curves for dynamic $^{13}NH_3$-ammonia PET (**a**) and perfusion MRI (**b**) in one mid-ventricular slice. The regions of interest from which tissue curve (blue) and AIF (red) were taken are highlighted in the baseline image prior to contrast arrival. The relationship of AIF and tissue curves between PET and MRI indicates the different relative distribution volumes of $^{13}NH_3$ and Gd-DTPA inside the tissue. Both CA injection speed and time resolution of perfusion images are about one order of magnitude lower for PET than for MRI.

Figure 2.9 shows examples of a mid-ventricular perfusion MR image series and the corresponding PET slice during the passage of intravenously administered CA. It also shows the signal enhancement over time, both from regions of interest inside the LV and the myocardium. By convention, any enhancement curve acquired from myocardial tissue space is called tissue curve, while a curve corresponding to blood enhancement, e.g. in the LV cavity, is called arterial input function (AIF). In a generic sense, quantitative perfusion imaging is based on using the AIF as a surrogate for CA input into the tissue vasculature. Quantitative estimation of tissue properties - e.g. flow in units of mL/min/g - is based on the mathematical modeling of the relationship between tissue curve and input function. The specific formalism of how this is performed depends greatly on the properties of the contrast agent and the time resolution of the imaging modality, and may include modeling of CA convection, its chemical interactions within the tissue, or both. In a broader

technical sense, analogies can be made to virtually any system characterization for which sampling of excitation and answer is used in order to deduce a response function that characterizes an unknown system at hand with respect to the excited property. This may refer to unknown elements in electric circuits, where excitations may be made in the current or voltage domain, in a similar way as in this case to perfused tissue, where an excitation in the CA concentration domain is answered with a distinct pattern of retention and outflow over time. With respect to myocardial perfusion MRI, the concepts and applications of stabilizing the search for a proper system characterization in the form of an impulse-response function - which is essentially a mathematical deconvolution problem - substantiate large parts of the scientific content of this thesis. With respect to quantitative PET perfusion imaging, application of the concepts of deconvolution and impulse responses are slightly modified to accommodate the low time resolution of PET, which is elucidated in detail in the following section.

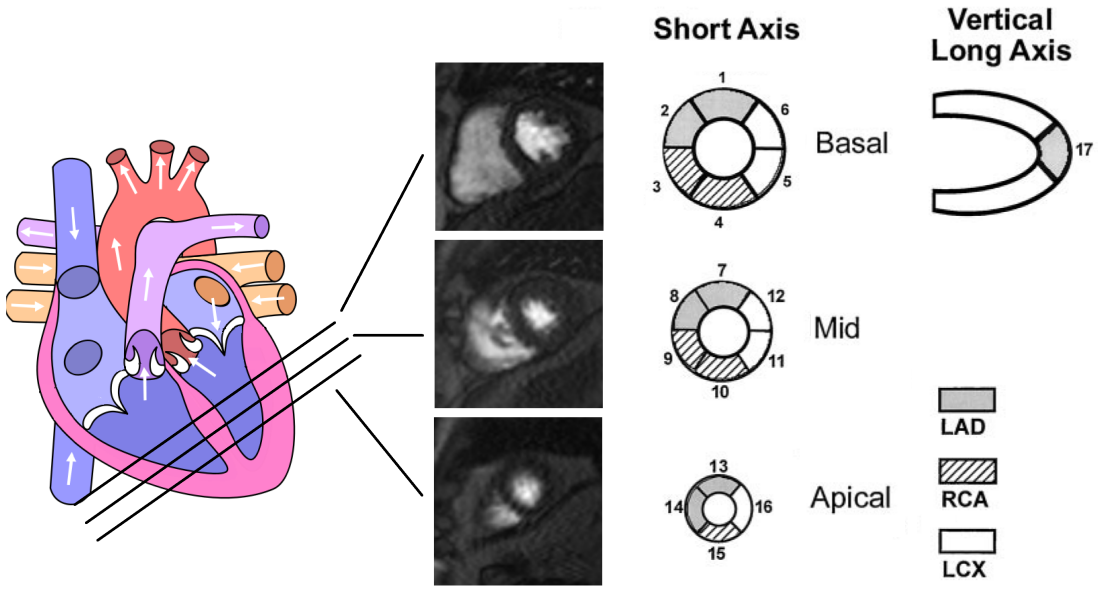

Figure 2.10: MRI example for placement of perfusion slices across the LV myocardium. Standard division into 17 segments is shown with the most common pattern of large artery support.[8]

In order to unify the terms for navigation inside cardiac imaging slices, there exists a standard segmentation proposition by the American Heart Association [29]. It divides the left-ventricular myocardium into a total of 17 segments distributed across three short-axis and one long axis slices. Figure 2.10 shows the segmented myocardium with basal and mid-ventricular slices each containing six, and the smaller apical position holding four segments. The 17th segment is represented by the most apical tip of the myocardium.

[8]Schematic image of the heart adapted with permission from [160]. Schematic depiction of coronary territories reproduced with permission from [29], © American Heart Association, Inc.

2.3.2 Dynamic $^{13}NH_3$-Ammonia PET

The basic concept of clinical PET perfusion imaging is the intravenous injection of a small, rapidly diffusible tracer molecule and the monitoring of its extraction from the vascular space and subsequent retention inside the tissue of interest. Historically, this mechanism was adapted from existing invasive techniques based on the administration of microspheres that were only applicable in preclinical settings. Such extraction-based approaches can be seen as a passive way of indicating actual vascular perfusion, because information about blood flow is only inferred from the rate of extraction from the vascular space (usually called K_1). Consequentially, the most important quality criterion for a perfusion tracer in PET is its diffusivity, i.e. how close to linear the relationship between extraction rate and vascular flow is, especially at high flow rates during stress testing. The four clinically available PET tracers vary in extraction efficacy from ^{82}Rb-Rubidium to $^{13}NH_3$-ammonia, ^{18}F-flurpiridaz and ^{15}O-water. Wide-spread clinical application of $^{13}NH_3$-ammonia and ^{15}O-water is hampered e.g. by the need for an on-site cyclotron, while worldwide regulatory approval for ^{18}F-flurpiridaz is still pending. Therefore, as of today, ^{82}Rb-Rubidium is one of the most widely used PET perfusion tracers despite mediocre extraction properties.

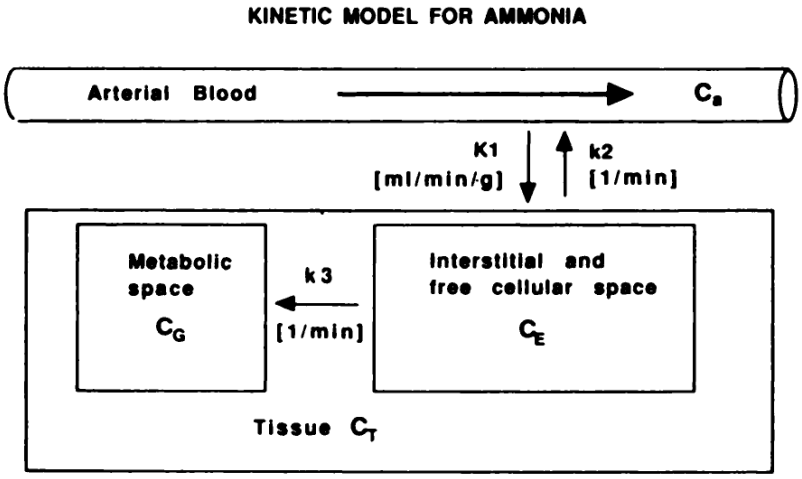

Figure 2.11: Schematic representation of functional myocardial tissue compartments with respect to ammonia distribution.[9]

One of the first applications of quantitative perfusion imaging that was established in a clinical setting was dynamic $^{13}NH_3$-ammonia PET, for which an example of dynamic data is given in Figure 2.9(b). One of the decisive advantages of PET with respect to quantitative imaging is the linearity of image signal to tracer concentration, i.e. after decay and attenuation correction. The main drawbacks are its low time and spatial resolution, as clinically achievable time windows for dynamic imaging are usually on the order of 10 s and intra-slice spatial resolution is usually not higher than 5 mm^2. Low time resolution is the technical reason why PET perfusion imaging can usually only infer characteristics of fast

[9]Image originally published in *JNM* [104], © Society of Nuclear Medicine and Molecular Imaging, Inc.

vascular tracer convection from extraction and retention in a slow-changing extravascular pool. Both the coronary transit of LV blood into the tissue (1 - 4 s) as well as the transit of blood through the tissue (2 - 10 s) may not be resolved directly, which is visualized e.g. by a missing delay in the onset between LV blood and tissue enhancement curves compared to MRI (Fig. 2.9).

The most established kinetic models for distribution of $^{13}NH_3$-ammonia classify myocardial tissue into three functional compartments [128]: A vascular space with $^{13}NH_3$ concentration C_a, an extravascular space with free diffusion (C_E) and a cellular space in which ammonia is irreversibly metabolized and retained (C_G). Linear kinetic rate constants K_1, k_2 and k_3 between tissue compartments are defined as shown in Fig. 2.11. With a dynamic correction for radioactive decay (λ), the basic pharmacokinetic differential equations for the tissue can be written as:

$$\frac{\partial C_E(t)}{\partial t} = K_1 C_a(t) - k_2 C_E(t) - k_3 C_E(t) - \lambda C_E(t) \tag{2.20}$$

$$\frac{\partial C_G(t)}{\partial t} = k_3 C_E(t) - \lambda C_G(t). \tag{2.21}$$

These may be solved with respect to a vascular input C_a and an extravascular tissue concentration C_T, yielding:

$$C_T(t) = C_E(t) + C_G(t) = R_K(t) \otimes C_a(t) \tag{2.22}$$

with

$$R_K(t) = K_1 \cdot \left[e^{-(k_2+k_3+\lambda)t} + \frac{k_3}{\alpha_+ - \alpha_-} \left(e^{-\alpha_- t} - e^{\alpha_+ t} \right) \right] \tag{2.23}$$

$$\alpha_\pm = \frac{(k_2 + k_3 + 2\lambda) \pm \sqrt{(k_2 + k_3 + 2\lambda)^2 - 4\lambda(k_2 + k_3 + \lambda)}}{2}. \tag{2.24}$$

A derivation of the above solution can be found in the Appendix of [63]. In the generic sense outlined in the previous section, it represent extraction and retention inside the tissue as the result of filtering the incoming signal profile, i.e. the AIF, with a convolution kernel R_K containing all information about the tissue in the form of rate constants.

With respect to the vascular tissue space, low temporal and spatial resolution in clinical applications motivate two major simplifications: As vascular blood signal from the tissue cannot be distinguished from LV blood signal with respect to time, C_a can be identified with the measured AIF. Additionally, the volumetric contributions of all blood activity inside the tissue can be lumped into a tissue-blood volume fraction (TBV) [63]. It represents the added relative volumes of the vascular bed inside the tissue and a potential partial-volume/spillover fraction from the LV. With that, the measured overall tissue concentration C_m can be expressed as:

$$C_m(t) = C_a(t) \cdot TBV + (R_K(t) \otimes C_a(t)) \cdot (1 - TBV) \tag{2.25}$$

Using the measured AIF (C_a) and tissue curve (C_m), this equation may be solved numerically for the four parameters TBV, K_1, k_2 and k_3. Finally, actual vascular blood flow (F) can be expressed as the ratio of K_1 and the so-called first-pass extraction fraction (E), which is related to the permeability-surface area product (PS) of the vascular wall for ammonia according to the Kety-Schmidt equation [76]:

$$K_1 = FE = F(1 - e^{-\frac{PS}{F}}) \tag{2.26}$$

The assumption that E is close enough to unity so that K_1 can be assumed equal to flow F is one of the fundamental limits of accuracy, although it has been shown to hold for the clinically relevant flow range [104,128]. An additional assumption that is usually made is that the presence of radioactive, blood-borne ammonia metabolites urea and glutamine that contribute to the AIF signal do not have a significant effect on flow estimation. While this has been shown to be accurate with respect K_1 and flow, estimates of k_3 may be significantly affected by metabolite correction [63,104]. Concerning the use of rate constants other than K_1, it has been shown that the ratio K_1/k_2 may also serve as an indirect way of characterizing the metabolically active $^{13}NH_3$ distribution volume [7].

For a comparison of the conceptual basics between PET and MRI flow estimation, it is important to note that the simplifications for tracer dynamics in the vascular space, described in this section for clinical $^{13}NH_3$ PET applications, are only valid at low time resolutions, irrespective of the imaging method. One implication of Eq. 2.20 is that the vascular tissue space appears as having no concentration gradient in flow direction, which is a valid assumption only as long as the time resolution is too low to observe the transit of blood through the tissue. In situations where kinetic data is sampled with high time resolution, models allowing for a more physiologically faithful representation of vascular flow dynamics have to be applied, as it is usually the case in MRI. The fact that this is not a feature of the imaging modality but a matter of dynamic data structure has been shown more recently by the application of axially-distributed vascular models with preclinical $^{13}NH_3$-ammonia PET at a time resolution of 2 s [1].

2.3.3 Dynamic Contrast-Enhanced (DCE-) MRI

Perfusion applications in MRI can be divided according to whether they include exogenous contrast agent or not. Non-contrast perfusion techniques such as blood-oxygen level dependent (BOLD) imaging or arterial spin labeling (ASL) are established for a number of cerebral applications, but complications such as cardiac and respiratory motion as well as a generally low sensitivity are limiting their effectiveness in cardiac MRI. The two clinically established methods that include CA are dynamic contrast-enhanced MRI and dynamic susceptibility contrast (DSC-) MRI. The latter is used mainly in cerebral studies, where e.g. Gd-DTPA and Gd-DOTA stay intravascular due to the blood brain barrier and therefore create significant susceptibility (T_2^*) contrast that may be used to identify vascular leakages. Its advantage in quantitative applications is the linearity of the MRI signal mapping the susceptibility effect to CA concentration, its dependence on CA intravascularity however limit its use to the brain. Perfusion MRI in oncology and cardiac applications relies on DCE-MRI, which maps the T_1-shortening properties of MRI contrast agents to a dynamic increase of image signal. While there are efforts to develop sequences that allow

perfusion acquisition comparable to PET, i.e. continuous in space and time, as of today the most stable and established cardiac DCE-MRI protocols are limited to acquiring non-isotropic 2D slices as snapshots. These usually cover 3-6 short-axis positions (see Fig. 2.10) during each cardiac cycle for a certain amount of time after CA injection.

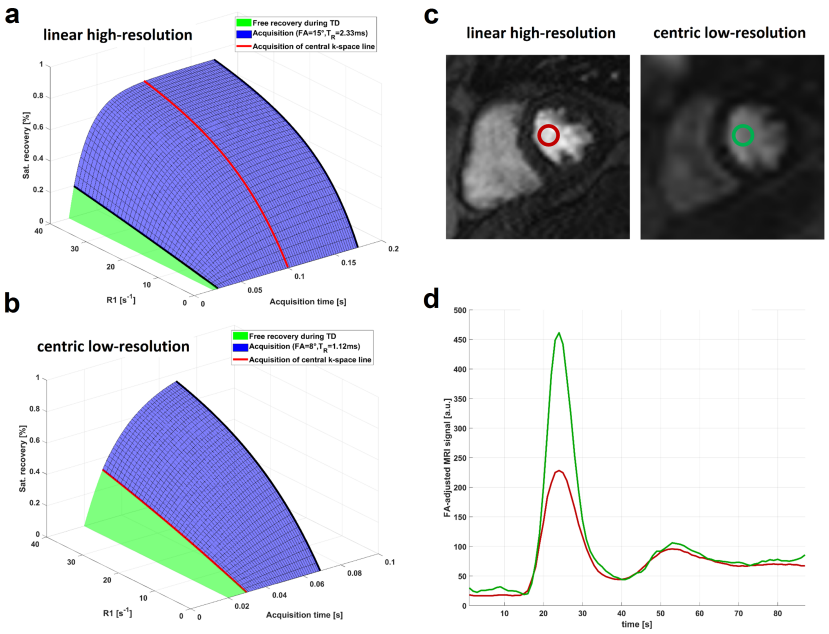

Figure 2.12: Effects of signal saturation in DCE-MRI for the example of an SR-FLASH dual-sequence design. Bloch-simulation of a high-resolution acquisition with centric k-space readout in the upper left shows a highly nonlinear relationship between R_1 and recovered magnetization along the highlighted central k-space line. Additional acquisition of images with adjusted sequence parameters and centric k-space ordering mitigate signal saturation at peak LV enhancement as shown on the right.

Depending on a trade-off between the desired slice coverage, in-plane resolution, SNR and the effects of cardiac motion, acquisition times for a single slice may vary anywhere below 200 ms. Due to ECG-triggering of the first acquisition in each cardiac cycle, cardiac motion appears frozen for each individual slice position. Respiratory motion is usually corrected retrospectively based on the dynamic image series as it is slow compared to image acquisition time and therefore only noticeable between images from different cardiac cycles. Figure 2.9(b) shows typical DCE-MRI enhancement curves visualizing a bolus passage of Gd-DTPA through the heart for a single slice position. Due to its relatively small extracellular distribution volume, the difference in relative voxel concentration of Gd-DTPA between tissue and peak blood signal is about one order of magnitude. Therefore, it is one of the main obstacles for perfusion quantification based on DCE-MRI to linearly map the highly shortened T_1 times during bolus passage to MRI signal, while still acquiring the tissue curve with appropriate sensitivity and SNR.

Standard T_1-weighted sequences may exhibit a strongly sublinear relationship between MR image signal and T_1, which is usually called signal saturation and varies with sequence

design. The Bloch-equation simulation in Fig. 2.12 shows this for the most widely used saturation-recovery (SR-)FLASH sequence, which achieves T_1 contrast through an initial destruction of all magnetization components and image acquisition during the subsequent recovery of longitudinal magnetization. An equation for the signal evolution considering only T_1 relaxation, i.e. assuming that echo time T_E is very short compared to T_2^*, may be derived from basic Bloch equations [12]. It contains a spatially-varying normalization constant S_0 and a function f characterizing the relationship of recovered magnetization signal with R_1:

$$\begin{aligned} S(T_N) &= S_0 \cdot f(R_1, T_D, T_R, N, \alpha) \\ &= S_0 \left[(1 - e^{-R_1 T_D}) \cdot a^{N-1} + (1 - e^{-R_1 T_R}) \cdot \frac{1 - a^{N-1}}{1 - a} \right] \end{aligned} \tag{2.27}$$

with

$$a = cos(\alpha) \cdot e^{-R_1 T_R}.$$

The function f predicts recovered magnetization available for acquisition of the Nth k-space line. It takes into account a delay time T_D after saturation as well as N-1 preceding acquisitions with repetition time T_R and flip angle α. The central k-space line, which effectively corresponds to image signal magnitude, is highlighted in red in Fig. 2.12 showing the non-linearity between R_1 and MR image signal for the case of a regular perfusion acquisition. The most widely-used approaches to overcome this are referred to as dual-bolus, dual-sequence and theory-based magnetization modeling techniques. The most logistically challenging is the dual-bolus approach, which includes injection of a diluted or smaller pre-bolus [83] to measure an AIF curve at a level of signal saturation that is comparable to the tissue curve. The so-acquired AIF is scaled by the dilution factor to recreate a hypothetically unsaturated AIF, and the tissue curve is acquired afterwards using a full bolus of CA, while both pre-bolus tissue curve and full-bolus AIF are discarded. The more elegant dual-sequence approach also separates acquisition of AIF and tissue curve, but does so by adding a short additional low-resolution acquisition at a single basal slice position to each cardiac cycle [46]. Sequence parameters and k-space ordering for the low-resolution image are adjusted so that they map changes in T_1 close to linearly to image signal as shown in Fig. 2.12. The logistically most simple approach is the theory-based calibration of dynamic T_1 with DCE-MRI image signal by using a theoretical simulation of the sequence with known parameters such as Eq. 2.27. Recovery of the normalization constant S_0 may be performed either using additional proton-density weighted images [28] or a combination of pre- or post-contrast baseline signals and additional reference T_1 values [17].

Assuming that tissue curve and AIF accurately reflect T_1 values during CA bolus passage, CA concentration may be calculated according to Eq. 2.12. Before modeling the relationship between AIF and tissue curve, the AIF needs to be adjusted for differences between voxel reference volume (i.e. whole blood) and CA distribution volume (i.e. blood plasma). Therefore, in order to obtain an accurate input function for the vascular, i.e.

plasma, tissue space, the reference frame for concentration can be shifted from whole blood (b) to plasma (p) using arterial hematocrit $\mathrm{hct_a}$ according to [134]:

$$AIF_p = \frac{AIF_b}{1 - hct_a}, \quad F_b = \frac{F_p}{1 - hct_t}, \quad v_b = \frac{v_p}{1 - hct_t}. \tag{2.28}$$

Rescaling of resulting plasma parameters, i.e. flow F_p and volume v_p, to corresponding blood parameters requires the introduction of a tissue hematocrit $\mathrm{hct_t}$ for the vascular bed. Note that this rescaling also implies the assumption of equal flow patterns of plasma and blood within the tissue.

2.3.4 DCE-MRI Tissue Modeling

In the early days of DCE-MRI, the paradigm of calculating vascular flow from CA extraction akin to established PET or microsphere applications has led to the development of approaches such as the Tofts-model [139]. It is mathematically equivalent to the ammonia model described above (Eq. 2.25 with $k_3 = \lambda = 0$), and originally had the purpose to use K_1 for characterization of vascular lesion in the blood brain barrier. However, the effects of a low and more variable extraction of Gadolinium-based agents compared to PET tracers preclude application of models oversimplifying vascular kinetics for most DCE-MRI applications [135].

In a generic sense, most of the existing DCE-MRI modeling approaches - especially for the myocardium - can be related more directly to earlier applications of the indicator-dilution principle, in which tissue is thought of strictly a as black-box system. In their invasive form, indicator-dilution techniques include the injection of dyes or radiolabeled molecules (indicators) into the feeding vessel of an organ or vascular bed of interest. Simultaneously, a time-concentration profile of the indicator mixed with blood is sampled from all exit pathways of the vascular bed. The so-acquired outflow curve can be identified with the distribution of transit times through the organ, historically called h, if the following conditions hold:

1. The input injection is rapid enough to be considered a δ-like impulse.
2. There is no recirculation of indicator.
3. The vascular system is linear and time-invariant, meaning that its properties do not change with time or indicator concentration.

The transit time distribution h fully characterizes the flow pattern of the vascular bed in a statistical sense and can equivalently be described as a function of transit frequencies over time. For an intravascular indicator, it may exhibit the shape of a right-skewed Gaussian or gamma-variate function as depicted in Fig. 2.13.

However, the (complete) sampling of outflow curves is by definition an invasive process and not compatible with clinical applications. Additionally, while the third condition stated above is the foundation of any kinetic analysis using linear rate constants, the first two cannot readily be met in non-invasive situations. The original comprehensive set of mathematical tools for the description of indicator-dilution techniques using external monitoring instead of outflow analysis was given by Zierler in the 1960s [151]. Its basis is the

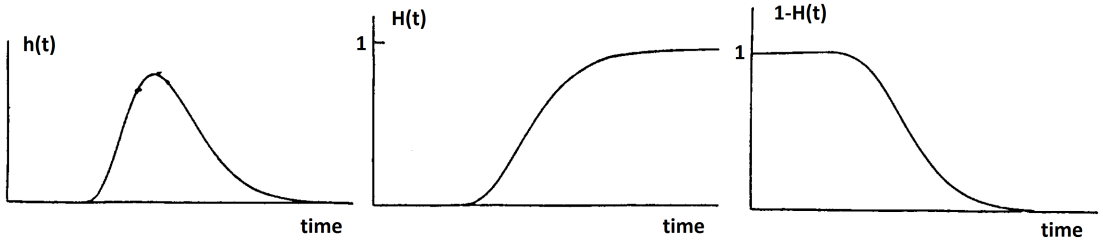

Figure 2.13: Basic indicator-dilution curves $h(t)$, $H(t)$ and $1 - H(t)$. The transit time distribution h reports the frequencies of transit events, its cumulative distribution H therefore is the fraction of indicator having left the tissue, and its reverse cumulative distribution gives the fraction of indicator remaining in the tissue at time t after injection.[10]

concept that transit of indicator can be described by relating its accumulation within the tissue to a so-called remaining fraction $1-H(t)$ via mathematical convolution. While measuring accumulation instead of outflow is the basis for its non-invasiveness, the convolution approach is also able to both cope with recirculating indicator as well as accept indicator input functions that are more dispersed than sharp δ-like impulses. The defining equation of the convolution approach can be given in analogy to the corresponding equations for PET (Eqs. 2.23 and 2.25) with tissue curve C_m and AIF C_a. The main difference is that vascular kinetics are fully included within the filter function R_F, and its normalization constant is therefore not extraction K_1 as in PET but actual vascular flow F:

$$\begin{aligned} C_m &= C_a(t) \otimes F \cdot (1 - H(t)) \\ &=: C_a(t) \otimes R_F(t) \end{aligned} \tag{2.29}$$

A detailed derivation of this equation from the basic principles of indicator-dilution theory is given in Appendix A. Solving it with respect to R_F, which contains all information about the tissue as related to CA distribution, is equivalent to a deconvolution of tissue curve C_m with input function C_a. For a computationally efficient implementation, Eq. 2.29 may be vectorized assuming that both measured curves consist of n discrete data points sampled in uniform steps Δt:

$$C_m(t_i) = \Delta t \cdot \sum_{j=1}^{i} C_a(t_i - t_j) \cdot R_F(t_j) = \sum_{j=1}^{i} A_{ij} \cdot R_F(t_j) \tag{2.30}$$

[10]Image reproduced with permission from [151], © American Heart Association, Inc.

with

$$\boldsymbol{A} := \Delta t \cdot \begin{pmatrix} C_a(t_0) & 0 & 0 & \dots & 0 \\ C_a(t_1) & C_a(t_0) & 0 & \dots & 0 \\ C_a(t_2) & C_a(t_1) & C_a(t_0) & \dots & 0 \\ \vdots & \vdots & \vdots & \ddots & \vdots \\ C_a(t_n) & C_a(t_{n-1}) & C_a(t_{n-2}) & \dots & C_a(t_0) \end{pmatrix}. \tag{2.31}$$

Because R_F is as such not determined by any tissue- or indicator-specific assumption, different strategies for solution of Eq. 2.29 may be applied. These are introduced in the following sections, including regularized analytic deconvolution as well as model-constrained deconvolution using shape functions that are either heuristic or parameterized in a physiologically meaningful way.

Model-free Deconvolution

The main problem for direct analytic deconvolution, e.g. by division of C_m and C_a in the Fourier domain or matrix inversion of $\boldsymbol{A}$, is that as soon as the AIF deviates from a perfect δ-impulse, the frequency content of the excitation it provides with respect to indicator concentration is reduced. In this situation, direct deconvolution is equivalent to the attempt of reconstructing an answer of the tissue to frequencies that were never excited by the AIF in the first place, which is commonly referred to as an ill-posed problem. Consequentially, this leads to arbitrary high-frequency oscillations in the time-domain solution of R_F already in the presence of minimal noise. The main strategy for overcoming this problem in model-free deconvolution is using a regularized singular value decomposition (SVD) approach, which allows for introduction of variable side constraints or basis functions for the construction of R_F. Regularized SVD effectively dampens the high-frequency content of R_F in the Fourier domain and thus reduces oscillations in the time domain. Both the effect of regularization as well as the oscillations in time and the underdetermined frequency content in frequency space for unregularized deconvolution are visualized in Fig. 2.14.

For SVD, a number of different regularization approaches exist, and a detailed educational review as well as implementation advice may be found in [58]. The most common form of regularization that is used throughout this thesis is called Tikhonov regularization, and may be expressed by rephrasing Eq. 2.30 as a minimization problem:

$$\boldsymbol{x}_\lambda \; = min \left\{ \|\boldsymbol{A}\boldsymbol{x} - \boldsymbol{b}\|_2^2 + \lambda^2 \|\boldsymbol{L}\boldsymbol{x}\|_2^2 \right\}, \tag{2.32}$$

with vectorization of curves

$$x_i = R_F(t_i), \qquad b_i = C_m(t_i).$$

The regularization operator L whose weight is controlled by λ may represent any linear smoothness constraint, the most common choice being a first-order differential operator. In order to arrive at plausible solutions $\boldsymbol{x}_\lambda$ while avoiding excessive damping, the choice of a regularization parameter λ usually includes weighting the residual norm $\|\boldsymbol{A}\boldsymbol{x}_\lambda - \boldsymbol{b}\|_2^2$ against the solution norm $\|\boldsymbol{x}_\lambda\|_2^2$. A widely-used optimality criterion for this is the so-called L-curve criterion [57], and an example for a so-regularized deconvolution result can be seen

in Fig. 2.14 (b/c). Flow F is finally extracted from the resulting R_F curve as its maximum amplitude, where accuracy is limited in cases of highly damped solutions as well as cases exhibiting significant oscillations.

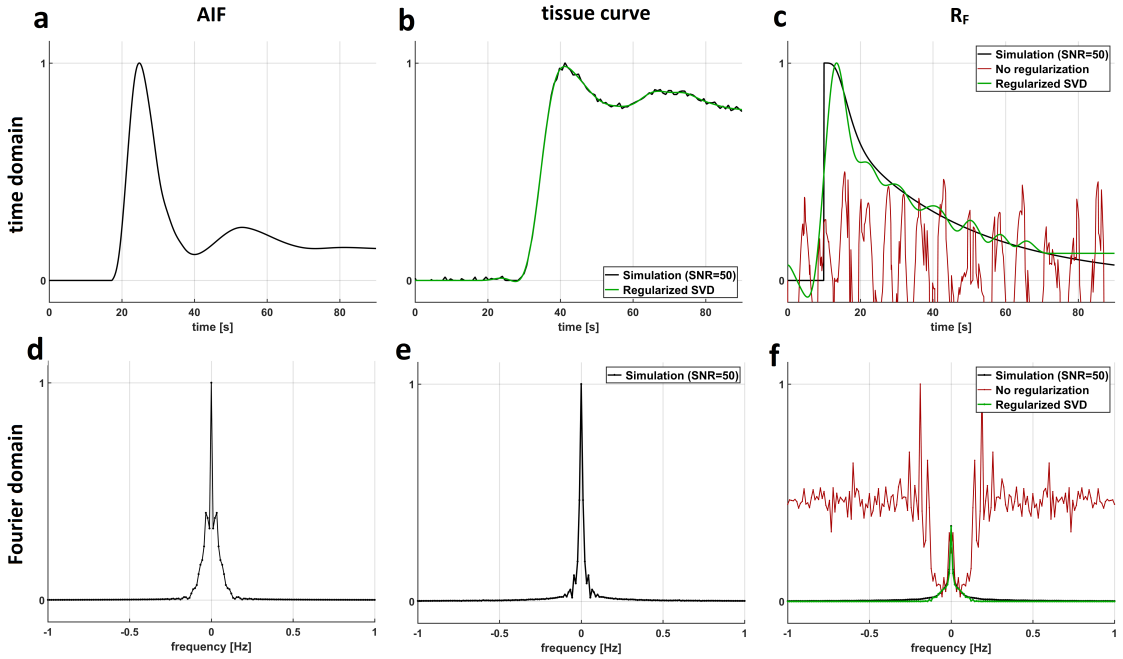

Figure 2.14: Examples for direct deconvolution in the Fourier domain and SVD regularization. The upper panel shows time domain representations for a measured AIF (**a**), a tissue curve simulated with SNR 50 (**b**) and the corresponding response function (**c**). The lower panel shows the respective Fourier transform spectra for a frequency range of -1 Hz to +1 Hz. The red curve in (**c**/**f**) visualizes a response function resulting from deconvolution of tissue curve and AIF via direct division of their Fourier transforms. As seen in (**d**), the Fourier spectrum of the AIF deviates from a δ-like excitation of all frequencies, which leads to arbitrary oscillations at higher frequencies where the AIF, i.e. denominator of the Fourier deconvolution, is close to zero (**f**). The use of regularized SVD for adaptive damping of high frequency content is visualized in green (**b**/**c**/**f**).

In addition to Tikhonov regularization, deconvolution may be stabilized further by introducing the constraint that R_F be constructed from a set of smooth basis functions. This has been shown for deconvolution in general [144] and specifically for cardiac DCE-MRI data [69] with the use of so-called B-splines. Splines are commonly used to interpolate functions by representing them as concatenations of polynomials with degree d that are defined piecewise between a series of knots (or control points), resulting in $d-1$ times

smoothly differentiable interpolating curves. A mathematical representation of the response function R_F in terms of a spline basis can be given as:

$$R_F(t_i) = \sum_{j=1}^{p} B_j^{(d)}(t_i) \cdot \alpha_j \tag{2.33}$$

Here, $B_j^{(d)}$ is the jth B-spline of degree d and α_j is its corresponding coefficient. The spline is defined on a sequence of $p+d$ knots where p is the number of coefficients. Depending on the desired properties with respect to smoothness or behavior at the edges, knots with multiplicity >1 may be introduced, maintaining the original number of knots and reducing the number of variable coefficients. In analogy to the definition of the convolution matrix A in Eq. 2.30, the spline representation given above may be inserted into Eq.2.29 according to:

$$C_m(t_i) = \Delta t \cdot \sum_{j=1}^{p} \sum_{l=1}^{i-1} C_a(t_i - t_j) \cdot B_j^{(d)}(t_i) \cdot \alpha_j = \sum_{j=1}^{p} D_{ij} \cdot \alpha_j \tag{2.34}$$

The difference between matrices A and D is essentially a basis transformation from an n-dimensional basis of sampled time points to a p-dimensional basis of spline coefficients. Solving for coefficients α_j by exchanging matrix A with matrix D in Eq. 2.32 usually reduces the dimensionality of the problem, while the shape of the resulting curve may be better controlled by individual placement of knots along the time course of sampled data.

Model-constrained Deconvolution

While regularized SVD may provide a computationally efficient, stable deconvolution method, it is limited to heuristic flow estimation by examining the shape of the response function R_F. A more complete description of CA kinetics would also include parameters that represent e.g. vascular extraction or fractional volumes of functional compartments within the tissue in analogy to the described PET model. The most comprehensive tissue model that is established in the the context of myocardial perfusion is the so-called Multiple path, Multiple tracer, Indicator-Dilution, 4 region (MMID4) model. It is used to simulate indicator kinetics in the tissue by explicitly modeling the vascular hierarchy as a set of tubes [80] and vascular exchange in a dedicated Blood-Tissue Exchange (BTEX) unit [6] as shown in Fig. 2.15. The commonly used implementation [158] includes capillary transport and exchange in up to 20 parallel pathways in order to account for flow heterogeneity. Despite an early application to clinical DCE-MRI data [79], determination of large sets of diffusion, flow and volume parameters from experimental data is limited by noise corruption. Therefore, the MMID4 is mainly used for forward simulation of tissue curves that may act as a physiological ground truth for simulation studies such as shown in Fig. 2.14. For clinical experimental settings, the physiologically meaningful parameters that are commonly used to characterize indicator distribution in DCE-MRI analysis are [134]:

- Perfusion flow (F_p or F_b) in units of mL/min/g, representing the total displacement of plasma or blood volume through a vascular system.

- The vascular permeability-surface area product (PS) in units of mL/min/g, representing a combination of average permeability and the total surface area of all vascular walls across which indicator exchange occurs.
- First-pass extraction fraction (E) in %, reporting the probability for an indicator particle to be extracted from the vascular space during its first passage through the tissue.
- Vascular volume (v_p or v_b) in %, representing the relative plasma or blood volume of indicator distribution with respect to the whole tissue volume.
- Extravascular-extracellular volume (v_e) in %, representing the relative extravascular distribution volume of indicator with respect to the whole tissue volume.
- Capillary/vascular transit time heterogeneity (CTH) in units of seconds, characterizing average flow heterogeneity within the tissue, usually defined as the standard deviation of transit times.

Depending on specific assumptions about tissue structure, most of the above parameters are connected to the others or may be expressed in terms of transit times through the individual distribution spaces. A detailed review on the most common tissue models and connections between their parameters can be found in [134].

In addition to the parameters above, a factor that affects all cardiac DCE-MRI data is the so-called bolus arrival time (BAT). It describes the constant time shift between AIF and tissue curve, which corresponds to the passage time of indicator from the LV cavity into the tissue through the arterial coronary circulation. While the BAT may be seen as somewhat independently informative on coronary morphology, it also represents the fact that the assumption of AIF sampling directly at the tissue entrance is fundamentally violated in the vast majority of quantitative perfusion measurements. While a neglect of the BAT significantly affects the deconvolution analysis [21], its influence on flow and other microvascular parameters may be contained by proper BAT estimation and incorporation into the modeling process [75]. For this, the BAT may be estimated either independently [30] or simultaneously during the deconvolution process. For stability reasons, estimation during the deconvolution process is usually not done by incorporating an additional shift parameter into the respective model, but either by iterative shifting of the AIF [85] or by a scout-fit with a simpler model [16]. While the BAT may be accounted for via linear shifting, the concomitant dispersion of the AIF shape during the coronary passage is one of the fundamental confounders to the accuracy of absolute estimation of microvascular parameters [129].

In the following, five tissue models of varying complexity that are relevant to this thesis are introduced and briefly discussed. Analytic closed-form solutions for response functions may be given both for time and Laplace domains. While solving Eq. 2.29 in the Laplace/Fourier domain has been shown to result in more efficient parameter estimation [45], not all models have representations in both domains.

The simplest conceivable way of modeling Gd-DTPA kinetics is to assume a single, well-mixed and homogeneous distribution volume in the tissue, which is in fact the correct

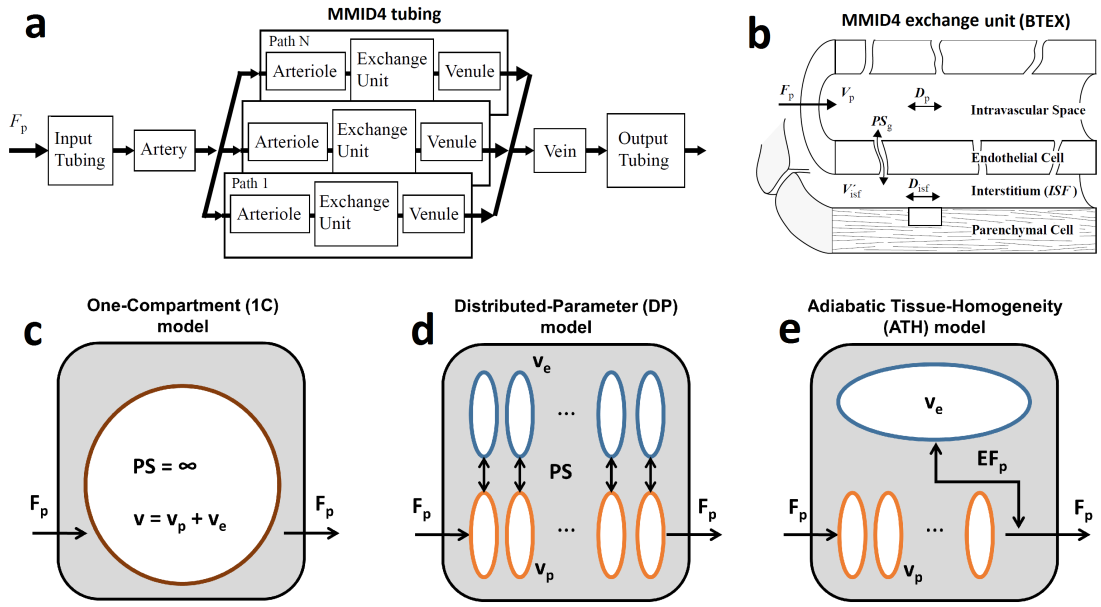

Figure 2.15: Tissue models of different complexity for DCE-MRI data analysis and simulation. The upper panel schematically shows constituents of the MMID4 model, i.e. the tubing architecture (**a**) and a detailed view of the exchange unit (**b**). Here, the extravascular space is referred to as the interstitial fluid (ISF), and parameters for diffusion inside vascular and interstitial spaces are defined as D_p and D_{isf} respectively. The lower panel (**c**-**e**) shows different simplifications made to the tissue structure in order to arrive at closed-form solutions for response functions.[11]

definition of a compartment. For this one-compartment (1C) model, flow is characterized by a single mean transit time T and the response function is a simple exponential:

$$\text{Time domain:} \qquad R_F^{1C}(t) = F_p \cdot e^{\frac{t}{T}} \tag{2.35}$$

$$\text{Laplace domain:} \qquad R_F^{1C}(s) = F_p \cdot \frac{1}{s + \frac{1}{T}} \tag{2.36}$$

Here, both extravascular and vascular distribution spaces are lumped together (v), and the overall mean transit time T is equal to the fraction v/F_p. Physiologically, the 1C model predicts a vascular wall that does not act as an effective barrier for indicator exchange, which is mathematically framed as an infinitely high and therefore unmeasurable permeability ($PS = \infty$). In order to avoid having to assume both an infinitely high permeability as well as instant mixing within the vascular space, a number of more complex two-region models have been developed. The first is the so-called Distributed-Parameter (DP) model [126], which predicts a finite vascular permeability and a concentration gradient of indicator in flow direction for both vascular and extravascular spaces as schematically

[11] Images (**a**) and (**b**) adapted with permission from [99], © National Simulation Resource.

shown in Fig. 2.15. Its Laplace domain response function is given below, while its time domain solution is too complex for computationally efficient implementation [134].

$$\text{Laplace domain:} \qquad R_F^{DP}(s) = F_p \cdot \frac{1 - e^{-s\frac{PSv_e + PSv_p + sv_e v_p}{F_p(PS + sv_e)}}}{s} \tag{2.37}$$

Note that the DP model does not predict any flow heterogeneity, i.e. indicator passes through all vascular pathways with the same transit time $T_p = v_p/F_p$ (plug flow). In order to avoid the previously challenging implementation of deconvolution in the Fourier/Laplace domain while still maintaining a realistic, two-region tissue structure, different approximations have been developed. The adiabatic Tissue-Homogeneity (ATH) model [136] differs from the DP model in that it assumes a well-mixed extravascular space - which is usually a much better approximation than a well-mixed vascular space - and allows vascular exchange only at the venous end of the exchanging vessel. With $\theta(t)$ as the Heaviside function and $k_{ep} = EF_p/v_e$, response functions for the ATH model can be given as:

$$\text{Time domain:} \qquad R_F^{ATH}(t) = F_p \cdot \left[\theta(T_p - t) + \theta(t - T_p) \cdot Ee^{-(t-T_p)k_{ep}}\right] \tag{2.38}$$

$$\text{Laplace domain:} \qquad R_F^{ATH}(s) = F_p \cdot \left[\frac{1 - e^{sT_p}}{s} + E\frac{e^{sT_p}}{k_{ep} + s}\right] \tag{2.39}$$

The derivations and underlying differential equations for both DP and ATH response functions may be found in [134]. In addition to a closed-form time domain response function, the core advantage of the ATH model is that vascular and extravascular kinetics are completely separated using Heaviside functions as shown in Eq. 2.38. This separability has been used to facilitate the introduction of a more realistic vascular flow heterogeneity into the ATH formalism, assuming either gaussian [82] or gamma-variate [127] transit time distributions. The latter has led to the definition of a so-called gamma capillary transit time (GCTT) model, which assumes the vascular transit time distribution function h_p to be a normalized gamma distribution $\mathcal{D}_\gamma$:

$$h_p^{GCTT}(t) = \mathcal{D}_\gamma(t; \alpha, \tau) = \frac{t^{\alpha-1}e^{-\frac{t}{\tau}}}{\tau^\alpha \Gamma(\alpha)} \quad \text{with} \quad \alpha - 1, \tau \geq 0. \tag{2.40}$$

Mean transit time and transit time heterogeneity are defined as distribution mean and standard deviation according to:

$$T_p = \alpha \cdot \tau, \qquad CTH = \frac{T_p}{\sqrt{\alpha}}. \tag{2.41}$$

A detailed derivation for the corresponding response function is given in [127]. It can be expressed in the time domain for vascular and extravascular spaces individually using the upper incomplete gamma function γ:

$$\text{Vascular:} \qquad R_p^{GCTT}(t) = \gamma\left(\frac{T_p}{\tau}, \frac{t}{\tau}\right) \tag{2.42}$$

$$\text{Extravascular:} \qquad R_e^{GCTT}(t) = \frac{Ee^{-k_{ep}t}}{(1-k_{ep}\tau)^{\frac{T_c}{\tau}}}\left[1-\gamma\left(\frac{T_p}{\tau}, \left(\frac{1}{\tau}-k_{ep}\right)t\right)\right] \tag{2.43}$$

In analogy to Eq. 2.38 for the ATH model, the full response function is given by addition of vascular and extravascular contributions:

$$\text{Time domain:} \qquad R_F^{GCTT}(t) = F_p \cdot \left[R_p^{GCTT}(t) + R_e^{GCTT}(t)\right] \tag{2.44}$$

While the four models described above are mathematically derived from basic physiology, the first and to this day most established model-constrained approach uses a heuristic shape function for R_F, taking into account only data corresponding to the first-pass of contrast agent. Use of this shape function, originally thought to describe purely vascular indicator kinetics [3], is widely-known as Fermi (-function) deconvolution [67]. It has been augmented for a more stable use in the context of extravascular contrast agent by a constant leakage term [61]. However, the assumption of negligible backflow from the EES makes its application less accurate if significant amounts of data from beyond the first pass are used in the analysis. Indicator transit is described as a logistic (Fermi-like) distribution, and the purely vascular response function as well as its augmented version can be given in the time domain as:

$$\text{Vascular only:} \qquad R_F^{Fermi}(t) = F_p \cdot \left[\frac{1}{1+e^{\frac{t-T_p}{\sigma}}}\right] \tag{2.45}$$

$$\text{Vascular + Leakage:} \qquad R_F^{Fermi+I}(t) = F_p \cdot \left[\frac{1-I}{1+e^{\frac{t-T_p}{\sigma}}} + I\right] \tag{2.46}$$

Here, I is the constant extravascular leakage term and the standard deviation of transit times is $\sigma\pi/\sqrt{3}$.

2.4 Quantitative Myocardial Tissue Characterization

2.4.1 MRI: T_1 and ECV mapping

While MRI may be used to quantitatively investigate a number of different functional parameters, the most obvious tissue properties for quantification are relaxation times T_1 and T_2/T_2^* on which all MR image signals depend in some form. The difficulty in measuring the latter is the fact that especially T_2^* times are usually very short, thereby strongly decreasing any image signal at longer echo times, ad exhibit a high sensitivity to local perturbations in magnetic susceptibility.

Conversely, the main difficulty for quantification of T_1 is its potentially long duration, reaching e.g. 2 s for blood at 3T. Accurate determination of T_1 from an experimentally

sampled relaxation curve would have to cover multiple durations of the time constant, which implies data acquisition over the course of at least 5 - 10 s. As this is longer than the time scales of both respiratory and cardiac motion, especially T_1 estimation in the heart has proven to be challenging. The most important innovation that facilitated widespread clinical use of cardiac T_1 mapping was the so-called modified Look-Locker inversion recovery (MOLLI) sequence [95]. On the basis of older techniques sampling T_1 relaxation curves multiple times after a single inversion [89], MOLLI sequences distribute a number of multipoint acquisitions into consecutive cardiac cycles during a single breathhold as shown in Fig 2.16(a). The shorthand notation for the originally proposed scheme is 3(3)3(3)5, which indicates three acquisition cycles after a first inversion followed by a waiting period of three cycles, three acquisition cycles after a second inversion followed again by three resting cycles before a final inversion with five acquisitions. Since characteristics of the sampled relaxation curve depend to some degree on the distribution of acquisition and recovery cycles, alternative schemes have been proposed [72] that are e.g. more robust to variations in heart rate (5(3)3) or more accurate for shorter T_1 times after administration of contrast agent (4(2)3(1)2).

In addition, an important confounding factor is residual respiratory motion, which, compared to the relatively mono-intense dynamic perfusion acquisitions based on saturation recovery, is harder to correct for retrospectively due to the changes of relative image contrast during inversion recovery. For estimation of T_1 from MOLLI data, the acquired measurement points are sorted across all inversions by their cumulative inversion time TI as shown in Fig. 2.16, yielding a final recovery curve that is related to T_1 according to:

$$SI = A - B \cdot e^{-\frac{t}{T_1^*}}, \qquad T_1 = T_1^*((B/A) - 1). \tag{2.47}$$

The second equation describes the so-called Look-Locker correction, expressing actual T_1 in terms of an apparent T_1^* that includes the influence of multiple measurements on the recovery curve itself. Fig. 2.16(b) shows an example for inversion signals from a 3(3)3(3)5 MOLLI scheme, reordered according to TI, as well as the corresponding fit for T_1^* according to Eq. 2.47. As all signals with negative polarity that occur early after inversion are mapped to positive values during acquisition, original polarities may be restored by iterative fitting approaches [107]. Executing the described fit procedure for all image voxels results in a mapping of T_1 relaxation across the myocardium and LV blood as shown in Fig. 2.16 both for the native state as well as after contrast agent administration.

Concerning contrast agent, the most established application of myocardial tissue characterization in MRI is so-called Late Gadolinium Enhancement (LGE) imaging. It can be understood as a qualitative version of quantitative T_1 mapping, for which T_1 weighted images are acquired a certain time after CA injection in order to highlight potential increases in relative CA distribution volume, i.e. for common Gadolinium-based agents an increase of the extracellular space. While qualitative techniques may suffice to assess the extent of focal increases in ECV, absolute quantification may benefit the assessment of focal severity or detection of diffuse disease processes [2]. An absolute extracellular volume fraction may be calculated by combining both native and post-contrast T_1 estimates. For each image

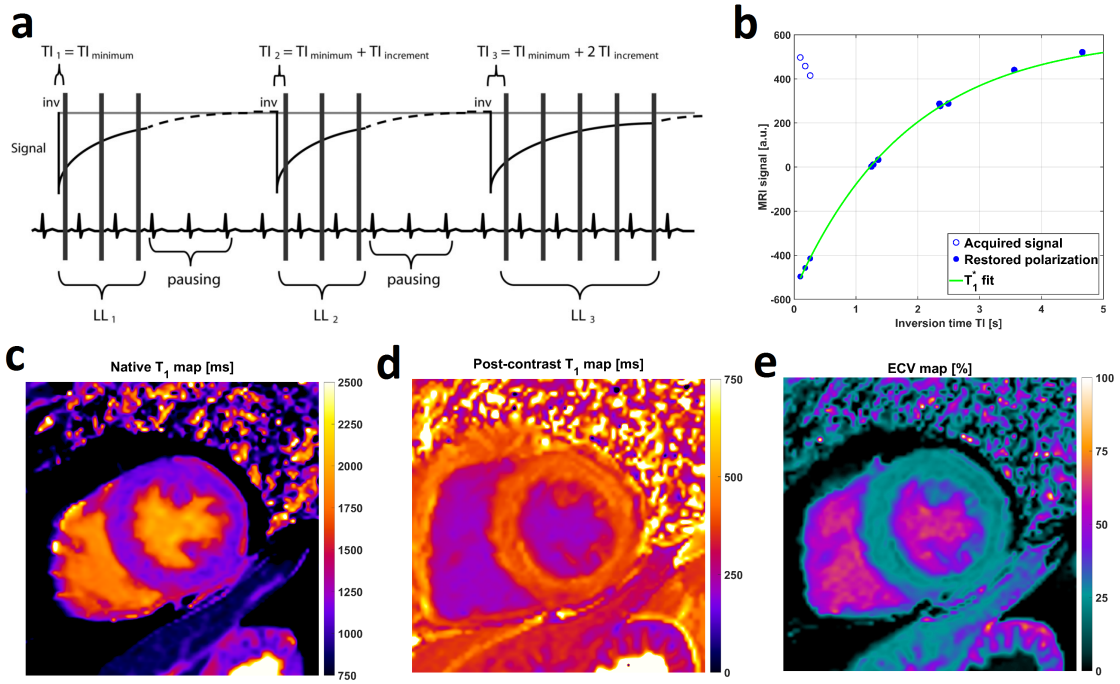

Figure 2.16: Acquisition scheme and mapping examples for T_1 and ECV estimation based on MOLLI. For the depicted 3(3)3(3)5 scheme, acquisition is distributed across three sets of inversions ($LL_{1\text{-}3}$) separated by two pausing periods (**a**). The fit for T_1^* on the basis of reordering according to inversion times TI and the concomitant restoration of signal polarity is shown in (**b**). Resulting native (**c**), post-contrast (**d**) and ECV maps (**e**) are shown in the lower panel for one short-axis slice position in a subject with no apparent cardiac pathology.[12]

voxel of native and post-contrast T_1 maps, relaxation may be expressed in terms of R_1 for cellular (c) and extracellular (ec) subspaces according to equation 2.12:

$$R_{1,native} = v_c \cdot R^c_{1,native} + (v_p + v_e) \cdot R^{ec}_{1,native}$$
$$R_{1,post} = v_c \cdot R^c_{1,native} + (v_p + v_e) \cdot (R^{ec}_{1,native} + r_1 \cdot [Gd]^{ec})$$

In the same way for an additional region of interest covering LV blood with plasma (p) and cellular (rbc) subspaces:

$$R^{blood}_{1,native} = hct_a \cdot R^{rbc}_{1,native} + (1 - hct_a) \cdot R^p_{1,native}$$
$$R^{blood}_{1,post} = hct_a \cdot R^{rbc}_{1,native} + (1 - hct_a) \cdot (R^p_{1,native} + r_1 \cdot [Gd]^p)$$

Assuming equal native relaxation rates for subspaces within the tissue, i.e. $R^c_{1,native} = R^{ec}_{1,native}$ as well as $R^c_{1,p} = R^{rbc}_{1,native}$, relative differences in R_1 can be defined as:

[12] Image (**a**) reproduced with permission from [93], © Wiley-Liss, Inc.

$$\Delta R_1 = R_{1,native} - R_{1,post} = (v_p + v_e) \cdot r_1 \cdot [Gd]^{ec}$$
$$\Delta R_1^{blood} = R_{1,native}^{blood} - R_{1,post}^{blood} = (1 - hct_a) \cdot r_1 \cdot [Gd]^{p}$$

If gadolinium concentration between blood plasma and the extracellular subspace is equilibrated - or at least in a transient pseudo-equilibrium - ECV can be directly expressed by R_1 differences and hematocrit:

$$ECV = v_p + v_e = (1 - hct_a) \cdot \frac{\Delta R_1}{\Delta R_1^{blood}} \tag{2.48}$$

The necessary equilibrium condition is generally accepted to be sufficiently achieved 10-15 min after injection [100], which is the same delay that is usually applied to maximize contrast in LGE imaging. An example of a so-derived ECV map is shown in Fig. 2.16(e).

Based on the development of cardiac T_1 mapping, ECV mapping is being increasingly applied in investigations of diffuse fibrotic disease processes [74]. With respect to avoidance of Gd-based contrast agents, also native T_1 without the extension to LGE/ECV mapping has received increasing interest in clinical studies. Native T_1 has been shown to be sensitive to an array of different disease processes, as alterations may occur in response to increased iron (Hemorrhage, Anderson-Fabry disease), free water (acute infarct) or fibrotic (LV hypertrophy) tissue content. One of the major confounding factors to the applicability of native T_1 as a quantitative biomarker is the significant variation in absolute values published for a number of different circumstances: Besides obvious differences pertaining to scanner field strengths, significant disagreement exists between MOLLI and alternative methods, e.g. based on saturation recovery (SASHA), as well as between different vendor implementations of the same method. Despite the normalization of R_1 in Eq. 2.48 and the link of ECV to basic physiology, global reference values for normal extracellular volume (range: 20-30%) may therefore vary with T_1 acquisition methods [147].

2.4.2 PET: Viability and Inflammation

While myocardial tissue characterization using MRI may be seen as visualizing rather mechanistic tissue properties such as distribution volumes or tissue composition, PET is generally more sensitive to metabolic tissue properties. Clinically established applications of cardiac tissue characterization with PET mostly rely on ^{18}F-FDG acting as a marker of cellular glucose metabolism. While myocardial cells may use a number of different substrates for energy supply, the most common ones are long-chain fatty acids and glucose. Under normal aerobic conditions the main energy source is fat, but ischemia may result in a switching of myocyte metabolism to glucose as a more efficiently convertible energy source under oxygen-deprived conditions [36]. In combination with reversible ventricular dysfunction, both short-lived stunning after acute myocardial events [60] or so-called hibernation as a result of repetitive ischemic episodes [117] are associated with a local upregulation of glucose metabolism. The corresponding findings from combined ^{18}F-FDG and $^{13}NH_3$-ammonia PET imaging have therefore been initially described as an apparent mismatch between perfusion and metabolism [130]. However, differentiation of stunning

and hibernation in patients with CAD is difficult in practice due to the existence of a continuum of structural and metabolic alterations in response to chronic ischemia [49].

With respect to such structural tissue alterations, the most common diagnostic application of ^{18}F-FDG PET in clinical practice is so-called viability imaging. It aims to asses the density of metabolically functional myocytes in the context of irreversible cellular damage, to which the described phenomena of post-ischemic upregulation of glucose consumption may contribute. In order to achieve the desirable high levels of FDG uptake also in normal myocardium, patients are usually metabolically prepared e.g. by intravenous insulin loading prior to ^{18}F-FDG injection and PET imaging [38]. An example for a patient exhibiting a viability defect due to fibrotic tissue alterations is shown in Fig. 2.17 with corresponding LGE images confirming an expansion of the extracellular matrix.

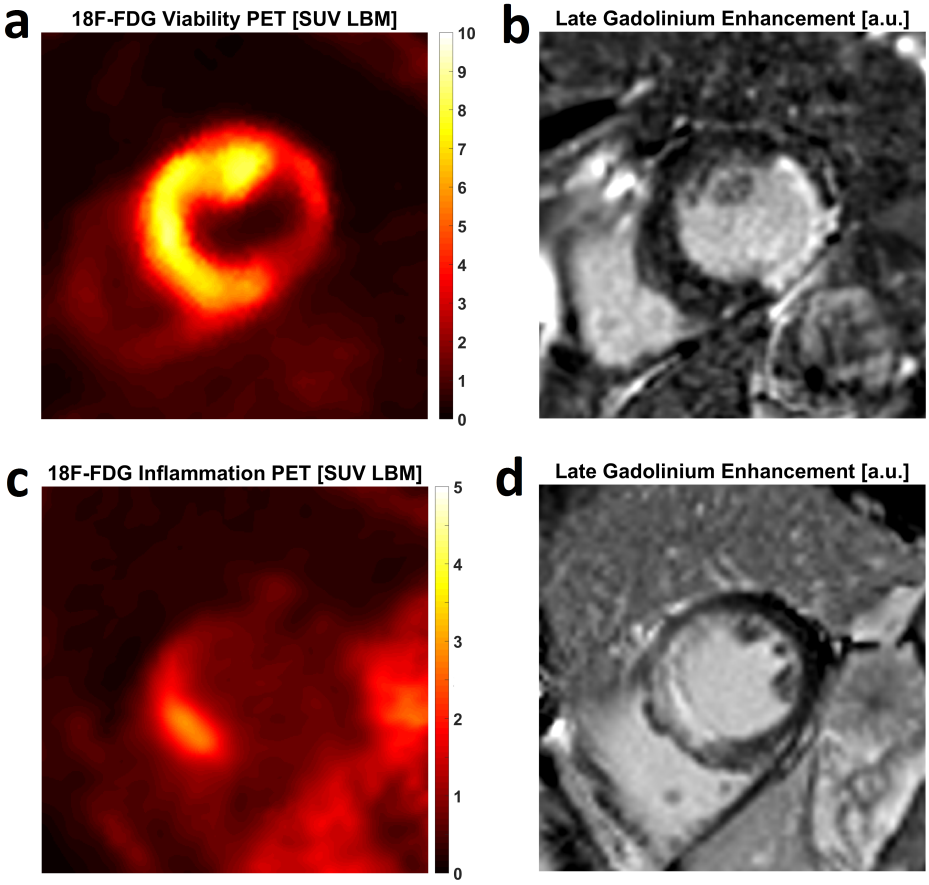

Figure 2.17: Examples for short-axis ^{18}F-FDG PET images corresponding to different ways of metabolic patient preparation. Stimulation of glucose consumption via intravenous insulin infusion induces high FDG uptake everywhere apart from an inferolateral region (**a**) with fibrotic tissue alterations as confirmed by LGE imaging (**b**). A suppression of normal metabolic glucose uptake by fasting and Heparin administration (**c**/**d**) is supposed to highlight the presence of inflammatory cells, here after acute myocardial infarction.

More recently, a cardiac ^{18}F-FDG application that has received increased interest is the targeting of infiltrative inflammatory cells post AMI [86]. While the role of the immune system after myocardial infarction is not well understood, it is believed that the healing process involves a dedicated balance in the activity of pro- and non-inflammatory monocyte subsets [105,142]. These are recruited to the site of infarction according to different timelines [105], first supporting the removal of cellular debris and subsequently the synthesis of the extracellular matrix. Due to upregulation of glucose uptake in activated inflammatory cells, ^{18}F-FDG has been proposed as a marker of inflammatory activity for a number of circumstances [90]. In cardiac applications, this involves the suppression of normal myocytic uptake, which may be achieved in a clinical setting by a low-glucose diet and additional administration of heparin prior to PET imaging [119,123]. However, despite reliable suppression of normal myocytic glucose metabolism, the potential presence of post-ischemic glucose consumption represents an uncertainty with respect to the quantitative interpretation of PET results [119], and the relationship between different signal contributions may additionally depend on the time of imaging post AMI [132]. A clinical example for inflammatory ^{18}F-FDG imaging is shown in Fig. 2.17.

Part II

Clinical Application

Chapter 3

Tissue Characterization with DCE-MRI: Measuring Vascular Permeability, ECV and Flow Heterogeneity Using an Hierarchical Fit Approach

Based on the work published in:
KP Kunze et al., Magnetic Resonance in Medicine 77 (6) 2320-2330, 2017.

3.1 Motivation

Quantitative dynamic contrast-enhanced perfusion MRI has been suggested as a promising diagnostic procedure for the characterization of coronary artery disease [31]. Recent years have seen an increasing interest in quantitative DCE-MRI measurements of microvascular perfusion characteristics beyond myocardial blood flow F_b. This includes the investigation of changes in vascular volume during adenosine stress testing [16,68,88] or estimation of the myocardial extracellular volume fraction [111]. However, many studies [64,88,111] are limited by making use of perfusion models similar or identical to the (extended) Tofts model. Depending on the time resolution of the perfusion data, such models usually oversimplify the vascular tissue region, leading to a well-documented inapplicability in a number of circumstances [135]. This notion is supported by increasing evidence that extravasation of Gd-DTPA in the myocardium is usually not flow-limited [16], which reinforces the need for more sophisticated models with a vascular substructure [82,127,134]. One such model is the distributed-parameter model, which assumes a uniform transit time for the vascular space [134]. It has been successfully applied to myocardial perfusion data in healthy volunteers [16] and, most recently, also in ischemic pathology [112]. However, the assumption of a uniform vascular transit time is also known to be inaccurate, because there is a finite degree of capillary transit time heterogeneity in myocardial tissue [124]. With the exception of an early application to myocardial residue curves [84], models assuming a finite CTH have mainly been used for forward modeling to simulate realistic tissue curves, as they usually imply explicit formulation of multiple capillary pathways. Although different modeling approaches exist incorporating CTH as a parameter for capillary flow distribution

(see Section 2.3.4), there have not yet been systematic applications to myocardial perfusion data. The concept of CTH, its physiological implications, and thus its measurement may become relevant, given recent evidence suggesting that transit time heterogeneity is a key determinant in the regulation of myocardial tissue oxygenation [109]. It has also been hypothesized that assessment of CTH may offer the possibility to better understand the involvement of perfusion and ischemia in different microvascular disorders.

Seeing the potential importance of measuring CTH, as well as the increasing interest in assessing myocardial ECV with T_1 mapping-based methods [100], this study had two main goals: First, to investigate the ability of myocardial perfusion MRI to measure myocardial ECV simultaneously with myocardial blood flow and capillary permeability-surface area product in patients with AMI. Second, to examine to what degree model-based estimation of myocardial CTH is feasible using clinical DCE-MRI perfusion data, and how the introduction of CTH as a model parameter affects the estimation of other perfusion characteristics. For these purposes, three perfusion models of different complexity were implemented in a hierarchical fashion. A two-parameter 1-compartment (1C) model, a four-parameter Adiabatic Tissue Homogeneity (ATH) model, and a five-parameter Gamma Capillary Transit Time (GCTT) model featuring a CTH parameter. The corrected Akaike Information Criterion was used to determine which model was best supported by the data, and thus to what extent microvascular kinetics could be resolved. The approach was tested by examining a group of patients shortly after myocardial infarction and subsequent revascularization. However, only patients without remaining flow deficits were considered, as any persistent, flow-limiting macro- or microvascular obstruction would arguably lead to different degrees of dispersion of the arterial input function [129], hampering comparability of perfusion parameter estimates between obstructed and non-obstructed tissue. As an alternative measure of tissue damage, reference equilibrium ECV measurements based on T_1 mapping were acquired during the same imaging session for comparison with perfusion results.

3.2 Methods

3.2.1 Patient Cohort

All imaging was performed on a clinical 3T PET/MRI tomograph (Biograph mMR, Siemens Healthcare GmbH, Erlangen, Germany). A total of 44 patients underwent examination in resting state 5 ± 1 days after successful revascularization of an acute coronary obstruction. Of those 44 patients, 24 were included in the final study cohort after exclusion of all patients exhibiting signs of microvascular obstruction (six), other severe perfusion defects (eight) or non-diagnostic data quality (six). Non-diagnostic data quality was found mostly in the MOLLI data, where three cases were excluded due to failure of the retrospective motion correction and two due to susceptibility artifacts extending across more than two myocardial segments. One dataset was discarded due to a very thin lateral wall, for which segmentation was deemed impossible. Mean age in the final patient group was 57 ± 11 years. Written consent was given by all patients, and the study was approved by the local Ethics Board.

3.2.2 Perfusion MR Image Acquisition

MR perfusion imaging was performed using a 2D ECG-triggered saturation-recovery FLASH sequence. A dual-sequence approach [46] included acquisition of an additional series of low-resolution images for dedicated assessment of the AIF. During 90 consecutive RR intervals, high-resolution perfusion images were acquired in three short-axis slices in the left-ventricular myocardium. Immediately preceding the high-resolution images, the aforementioned low-resolution acquisition with altered imaging parameters was performed at the most basal of the three perfusion slice positions in each RR interval in order to generate the AIF image series. A bolus injection of 0.05 mmol/kg Gd-DTPA (Magnevist, Bayer Healthcare, Leverkusen, Germany), followed by a 20-mL saline flush, was started at an injection speed of 4 mL/s after the first 10 RR intervals, ensuring accurate measurement of a pre-contrast baseline signal. A non-selective saturation pulse train was applied, followed by a delay time T_D, defined as the time between end of the saturation pulse and beginning of k-space acquisition. Typical imaging parameters for high-resolution perfusion acquisitions were: FOV $400 \times 300\,mm^2$, matrix size 192×144, 85% phase resolution, slice thickness 8 mm, in-plane resolution $2.08 \times 2.08\,mm^2$, T_D 5.14 ms, T_R 2.33 ms, T_E 1.03 ms, flip angle 15°, recovery time to center of k-space (T_I) 100 ms, receiver bandwidth 744 Hz/Px, 65 acquired lines per k-space in linear ordering. Typical imaging parameters for the low-resolution AIF acquisitions were: FOV $400 \times 300\,mm^2$, matrix size 64×48, slice thickness 10 mm, in-plane resolution $5.62 \times 5.62\,mm^2$, T_D 10 ms, T_R 1.12 ms, T_E 0.65 ms, flip angle 8°, 36 acquired lines per k-space in centric ordering. GRAPPA was used with an acceleration factor of 3 and 36 integrated reference lines per k-space that were used both for calibration and during image reconstruction. For each slice, the first three of the 90 repetitions were acquired without saturation pulses and with the flip angle reduced to 5°, resulting in proton density-weighted images.

3.2.3 Perfusion MR Image Analysis

All perfusion data were acquired in free breathing, and image-based motion correction was performed retrospectively once all repetitions were acquired. High-resolution perfusion images were motion corrected on the scanner, low-resolution AIF images were motion corrected offline. All images that were not acquired in matching parts of the cardiac cycle due to mis-triggering were removed from the time series. The myocardial wall was manually segmented prior to surface coil intensity correction (SCIC) and signal-to-concentration modeling (Fig. 3.1). For the high-resolution perfusion images, an approach similar to the one presented by Cernicanu et al. [28] was implemented. It essentially combines SCIC and signal to concentration modeling, using the first PDW image to derive the spatially varying normalization constant S_0. The surface coil bias field was estimated for the previously segmented portion of the PDW image as a two-dimensional surface fit [28]. Since the deviation between PDW image signal and true S_0 depends only negligibly on R_1 for a flip angle of 5°, the ratio of true S_0 to PDW image signal was assumed to be a global constant. It was calculated using Eq. 2.27 with T_D set to infinity and assuming a constant native myocardial T_1 of 1.2 s during acquisition of the PDW images. After estimation of S_0, R_1 for the tissue curves was ultimately estimated by numeric inversion of Eq. 2.27.

A very similar approach was used to estimate R_1 from low-resolution AIF images [11]. In this case, due to significant partial-volume effects with the myocardial wall and papillary muscles, usually only one to five voxels could be assumed to represent uncontaminated LV blood signal. However, the volume of a voxel in the low-resolution images corresponded to a volume of about seven voxels in the high-resolution images. Of those voxels, the one with the highest area under its dynamic signal curve was chosen as the AIF, which marks the voxel that was most successfully motion corrected. Due to the central k-space ordering of the AIF acquisition, S_0 was assumed to be identical to PDW image signal and R_1 was estimated by direct inversion of Eq. 2.27 assuming $N = 1$ [11]. Estimation of R_1 was calibrated with previously acquired phantom data against reference spin-echo R_1 measurements resulting in a reduction of nominal flip angles for all calculations. Gd-DTPA concentrations for AIF and tissue curves were calculated from R_1 estimates according to Eq. 2.12 assuming a Gd-DTPA relaxivity of $4\,s^{-1}M^{-1}$. Deconvolution was executed in the plasma reference frame ($AIF = AIF_p$), and individually measured arterial hematocrit values were used for plasma to blood conversion of the AIF and vascular parameters according to Eq. 2.28. Equal tissue and arterial hematocrit as well as fast water exchange between all subspaces in blood and tissue was assumed.

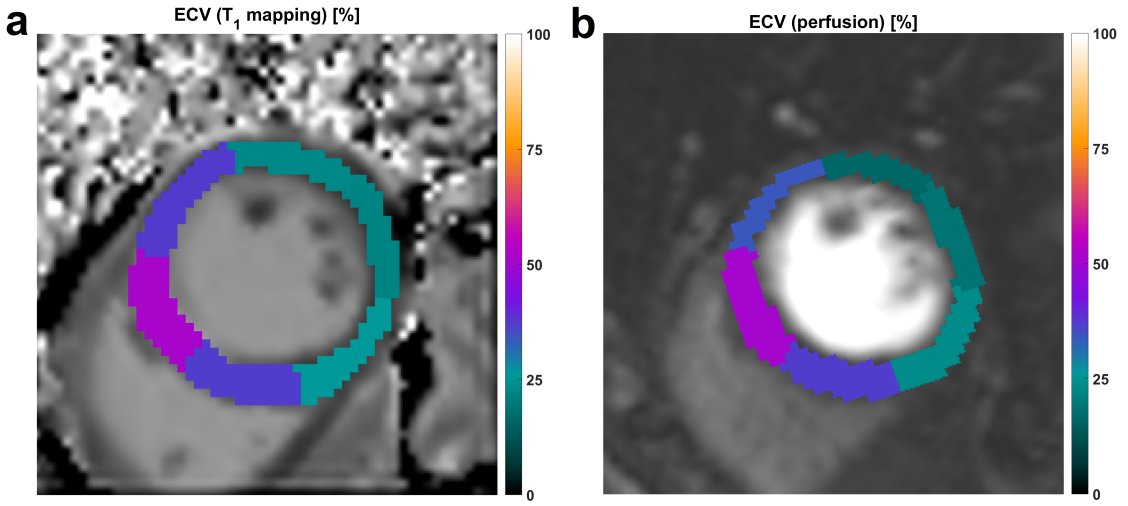

Figure 3.1: Examples for separate segmentation of ECV measurements acquired with the MOLLI equilibrium method (**a**) and perfusion modeling (**b**). ECV maps were generated from MOLLI data and segmented afterwards, perfusion images were segmented before modeling.

3.2.4 Perfusion MRI Data Modeling

AIF and tissue curves were linearly interpolated to uniform increments of 0.5 seconds, which ensured that the actual data were not undersampled by the interpolation. For model-constrained deconvolution, three different tissue models were used: First a 1C model, representing a situation in which extravasation of Gd-DTPA across capillary walls is flow-limited, and its distribution volume can be seen as a single well-mixed space. Second, the

two-region ATH model, assuming permeability-limited extravasation as well as a single uniform transit time for the vascular and an exponential distribution of transit times for the extravascular-extracellular space. Third, as a direct extension to the ATH model, a two-region GCTT model assuming a gamma-variate distribution of vascular transit times with CTH defined as its standard deviation. Deconvolution of Eq. 2.29 was performed in the Fourier domain for 1C and ATH models, using the closed-form Laplace-domain representations of response functions R_F shown in Eqs. 2.36 and 2.39 respectively. GCTT deconvolution analysis was executed in the time domain using the response function shown in Eq. 2.44.

With the three described models, a two-stage fitting approach was implemented. Therein, a decision concerning support for a more complex tissue model was first made between 1C and ATH models, and in a second stage between ATH and GCTT models. For this decision, corrected Akaike factors (cAIC), weighing fit residuals against the number of model parameters, were calculated as previously demonstrated for DCE-MRI data (Eq. 4 in [15]). In both stages, the model better supported by the data was assumed to be the one yielding the lower cAIC factor. The only exceptions were cases where the ATH fit estimated an extraction fraction E $>$ 99%. In such cases, PS was also deemed not measurable and the 1C fit results were used irrespective of cAIC factors. For 1C and ATH fits, the effective bolus arrival time (BAT), representing passage time of contrast agent through the coronary arteries, was not added as an additional parameter. Instead, fitting was iterated for all possible BAT values by advancing the measured AIF in steps of 0.1 s between zero and the initial difference of rising points between AIF and tissue curve. Parameters corresponding to the BAT showing the smallest fit residual were taken as final modeling results.

In the second stage, a decision between the ATH and the GCTT model was made by applying the GCTT model to all datasets for which the two-region ATH model was favored in the first stage. For stability reasons, both BAT and T_p were now constrained to a window equal to the time resolution of the scan (1/heart rate), centered around the values previously determined using the ATH model. The GCTT model - and thus estimation of CTH - was assumed to be supported if it yielded a lower cAIC factor than the ATH model. As in the first stage, the final modeling parameters were taken from the fit favored by the cAIC factors. Examples for fits and response functions from all models are shown in Fig. 3.2.

3.2.5 Equilibrium ECV Image Acquisition and Analysis

For equilibrium ECV mapping, native and post-contrast T_1 maps were acquired using a prototype Modified Look-Locker Inversion Recovery (MOLLI) sequence [95] at the same slice position and with the same spatial resolution as the perfusion images. Native T_1 maps were acquired directly before the perfusion scan. After the perfusion scan, but at least 15 minutes [100] before post-contrast T_1 map acquisition (average 25 $\pm$ 4 minutes), another Gd-DTPA bolus was given (0.2 mmol/kg). Identical 3(3)3(3)6 acquisition schemes were used for both maps. Typical imaging parameters were: FOV 400 x 300 mm^2, matrix size 192 x 144, slice thickness 8 mm, in-plane resolution 2.08 x 2.08 mm^2, T_R 2.8 ms, T_E 1.01 ms, flip angle 35°, Fourier factor 7/8, minimum inversion time 105 ms, inversion

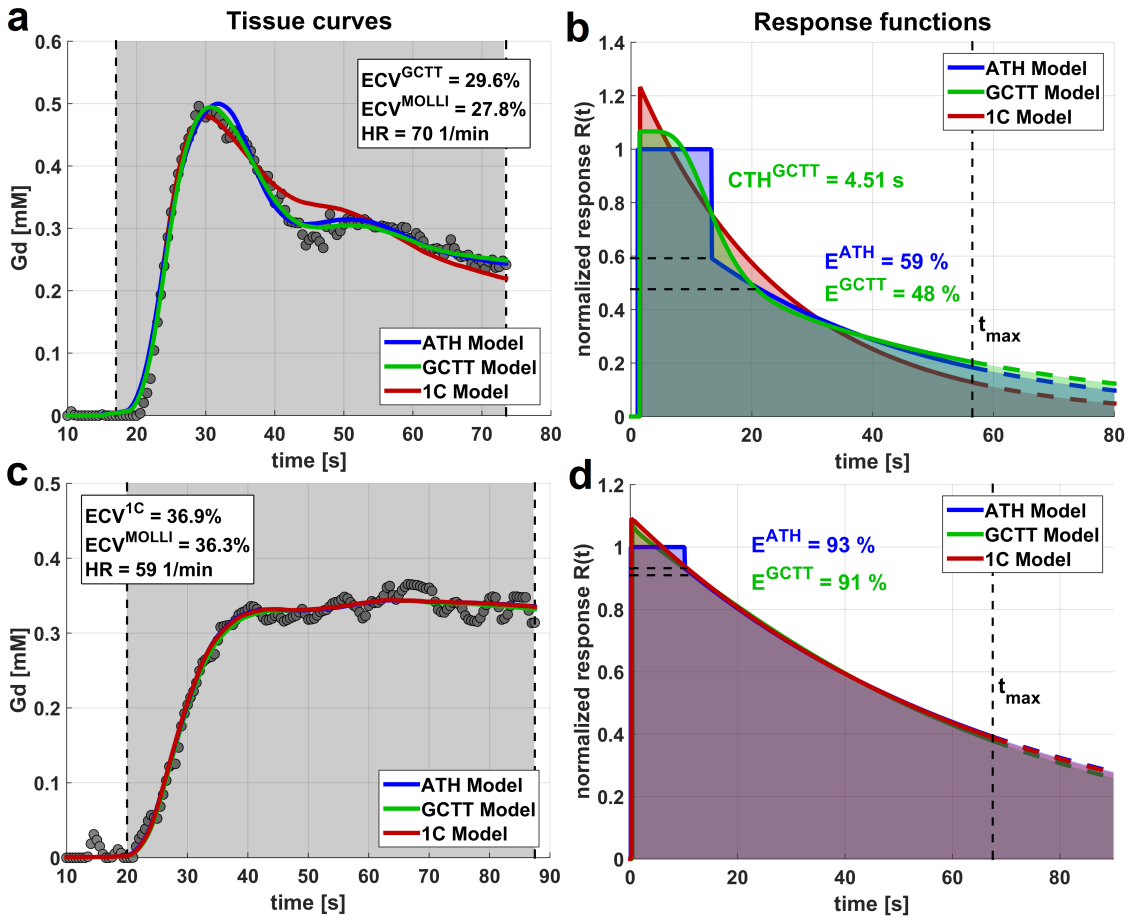

Figure 3.2: Representative tissue curves, fits and response functions for one remote (**a**/**b**) and one pathologic sector (**c**/**d**). According to the corrected Akaike criterion, estimation of CTH was feasible only for the remote segment, while not even PS was deemed measurable in the pathologic sector. For the latter case, the underlying ambiguity between 1C, ATH and GCTT response functions can be seen in (**d**), while the response functions shown in (**b**) underscore the measurable differences between modeling results for the first case. The time tmax during which indicator transit was observed is highlighted in grey (**a**/**c**).

time increment 80 ms. All MOLLI images were acquired in free breathing, patients were instructed to breathe shallowly to minimize respiratory motion. For each native and post-contrast MOLLI series, individual motion correction was performed on the scanner as implemented by the vendor of the tomograph. Native to post-contrast registration was performed offline. For this purpose, all 24 images of the native and post-contrast series were sorted into two groups according to the relationship of contrast between LV blood and myocardium. Images were registered within both groups individually, and groups were registered with respect to each other in a final step. Registered native and post-contrast MOLLI images were separated and fitted using a three-parameter model and the conventional Look-Locker correction according to Eq. 2.47 to generate both T_1 maps. Individual

hematocrit measurements from the day of examination (average: 0.39 ± 0.03) were used to calculate ECV maps [74] according to Eq. 2.48.

In each patient, one basal or mid-ventricular slice was chosen for analysis and divided into six segments according to standard 17-segment AHA segmentation [29]. Care was taken to morphologically align segmentation of ECV maps with the segmentation of perfusion data (Fig. 3.1). Offline motion correction for ECV mapping as well as for low-resolution AIF images was performed using precompiled C++ code (prototype) provided by the vendor of the MR tomograph [150], all other software for data post processing was custom written in Matlab R2015a (Mathworks, Natick (MA), USA). Data fitting for perfusion and T_1 evaluations used a Trust-Region-Reflective least-squares algorithm with constant initial parameter estimates across all sectors.

3.3 Results

Analysis of one mid-ventricular slice for each of the 24 patient datasets resulted in a total of 144 segments, of which four were discarded. Three were discarded due to small susceptibility artifacts in the T_1 maps confined to one segment and one due to blood contamination from the outflow tract. Concerning modeling of the perfusion data, the proposed approach using the Akaike criterion favored ATH model fits in 92 (65%), GCTT fits in 22 (16%) and 1C fits in 26 (19%) sectors. ECV and F_b are the only parameters reported for all 140 sectors, since none of the others were measurable using a 1C model.

Fig. 3.3 shows the comparison of equilibrium ECV and ECV estimates from the hierarchical perfusion analysis. A good correlation ($R^2 = 0.76$) between the two sets of values was observed, the range of ECV was 19 - 62% as determined by the equilibrium method. In regions with higher ECV, for which less data were available, perfusion-derived values tended to be even lower than average compared with the equilibrium values. This can also be seen in the Bland-Altman analysis shown in Fig. 3.4, which reports a mean difference of 1.14% and a standard deviation of 4.53%. The 95% limits of agreement were ±8.9%.

For comparison purposes, Fig. 3.5 shows ECV results for all sectors and all three models, where – apart from two outliers – GCTT and ATH models yielded very similar results. ECV results for the 1C model were slightly lower and subject to higher variability, however, fit quality was often worse than for the other two models (see Fig. 3.2(a)). Fig. 3.3 also shows EES volume v_e (b) and blood volume v_b (c) individually as a function of equilibrium ECV. The correlation of v_e with equilibrium ECV was very similar ($R^2 = 0.76$) to the one between ECV from both methods. The mean of v_b estimates was 9.9 ± 2.8%, and no correlation with ECV was observed.

GCTT fits, for the 22 sectors where they were favored by the Akaike criterion, yielded slightly higher v_b values than those obtained via the ATH model. Differences between parameter estimates from these two models are highlighted in all plots using green (GCTT) and red (ATH) points. Note that ATH results marked in red are only displayed to highlight the changes between both fits, and the cAIC-favored GCTT results marked in green were the final results of the hierarchical approach. The largest differences between ATH and GCTT estimates were observed for first-pass extraction (Fig. 3.6(a)), which decreased on average from 74.7% with the ATH fits to 61.1% with the favored GCTT fits. Figs. 3.6(b/c)

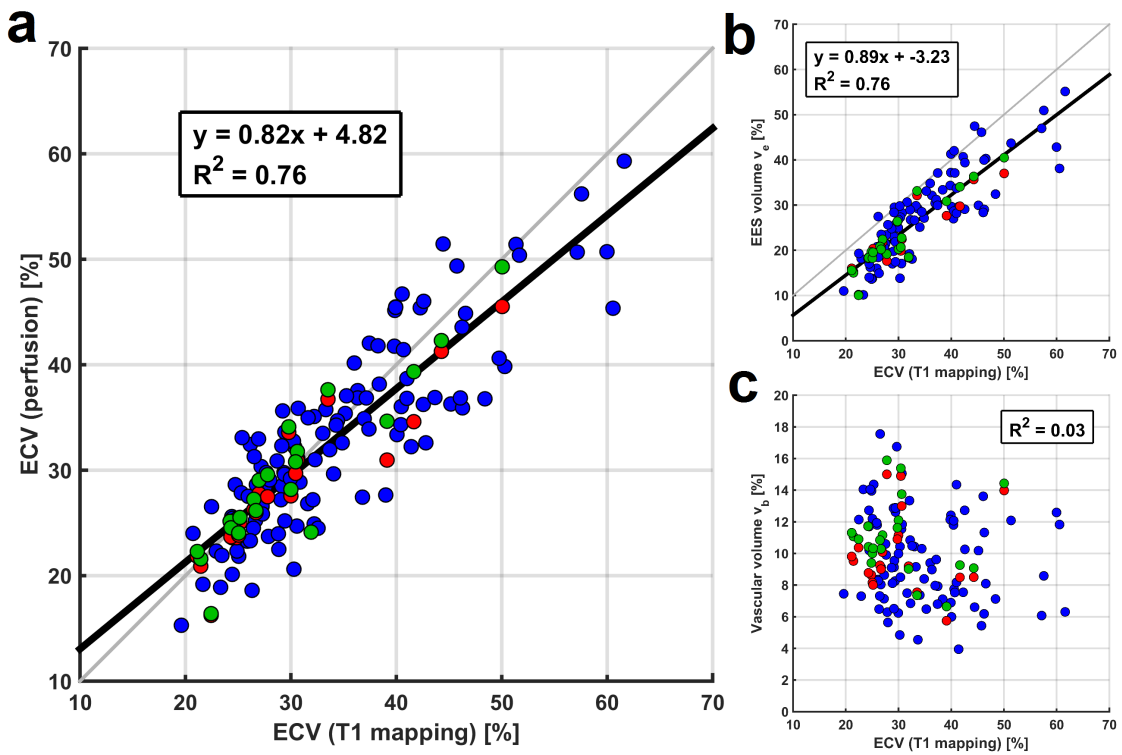

Figure 3.3: Comparison of T1 mapping-based ECV with perfusion-derived ECV (**a**) as well as with EES volume fraction ve (**b**) and blood volume fraction vb (**c**). Differences between ATH (red) and GCTT fit results (green) are highlighted for cases in which the latter were preferred by the Akaike criterion. These differences are largest for vb and relatively modest for ECV and ve. Note that all red points, representing the overturned ATH results, are only displayed for the purpose of visual comparison. Thus, the result of the proposed Akaike-based hierarchical approach as well as the basis for all linear regressions is represented by the combined number of blue and green points

show that no correlations were found between ECV expansion and PS nor F_b, mean blood flow and PS were 0.67 ± 0.15 and $0.62 \pm 0.20\,\mathrm{mL/min/g}$ respectively.

For those 22 sectors in which heterogeneity effects were measurable, the absolute differences in corrected Akaike factors (ΔcAIC) between the favored GCTT and the respective ATH fits was on average 14.6 ± 14.2.Measurable effects of CTH were found predominantly in sectors with lower ECV. A total of ten patients had at least one sector with measurable CTH, with one single case presenting with ECV $> 30\%$ and measurable CTH in all sectors. A typical pattern is illustrated by the six-segment evaluation in Fig. 3.7, where indeed only the remote sectors exhibit significant differences between GCTT and ATH fits. However, a direct inter-patient correlation between CTH and ECV estimates was not observed. Mean CTH was $5.45 \pm 2.04\,\mathrm{s}$, the mean ratio of T_p/CTH was 2.04 ± 1.11.

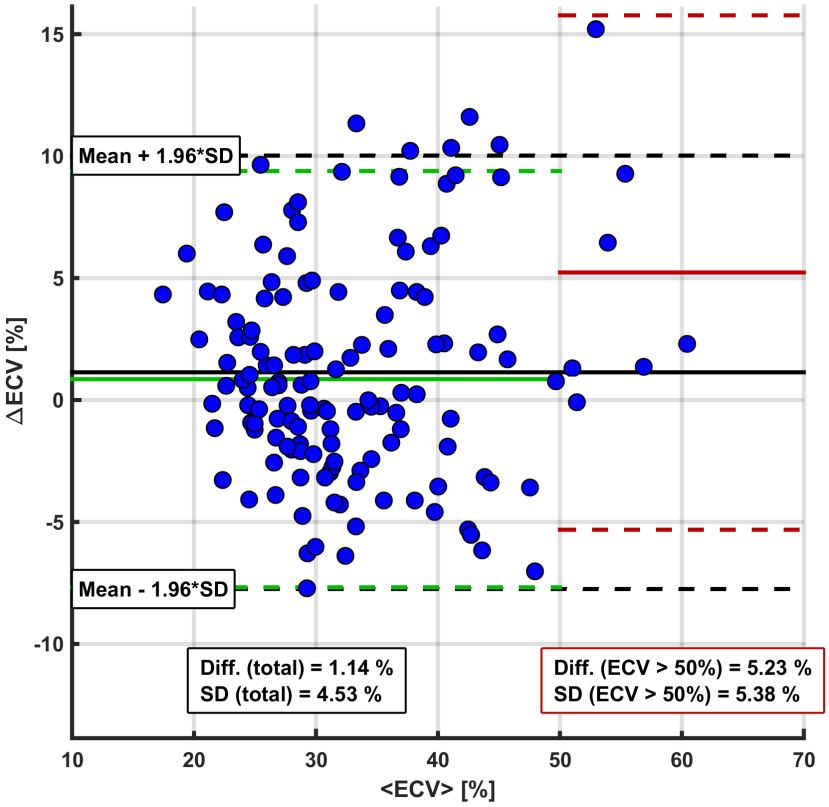

Figure 3.4: Bland-Altman plot for the comparison of T_1 mapping-based ECV with perfusion-derived ECV. Mean differences and limits of agreement are shown for all points (black lines), and separately for points with ECV smaller than (green) as well as larger than (red) 50%.

3.4 Discussion

The study presented here demonstrates the application of an hierarchical approach for model-selection involving three perfusion models with increasingly complex physiological implications. A corrected Akaike Information Criterion was used to determine to what degree it was possible to resolve myocardial microvascular Gd-DTPA kinetics with the DCE-MRI perfusion data at hand.

3.4.1 Measurability of PS and CTH

The main question for any model assuming a dedicated substructure of the vascular space is whether information from vascular space and EES can be sufficiently separated by the fit. That is, besides noise contamination, usually the question of whether extravasation of Gd-DTPA is flow-limited or permeability-limited. The flow-limited case is characterized by an extraction fraction approaching 100% and a subsequent impossibility to study vascular characteristics, because vascular space and EES become a single functional re-

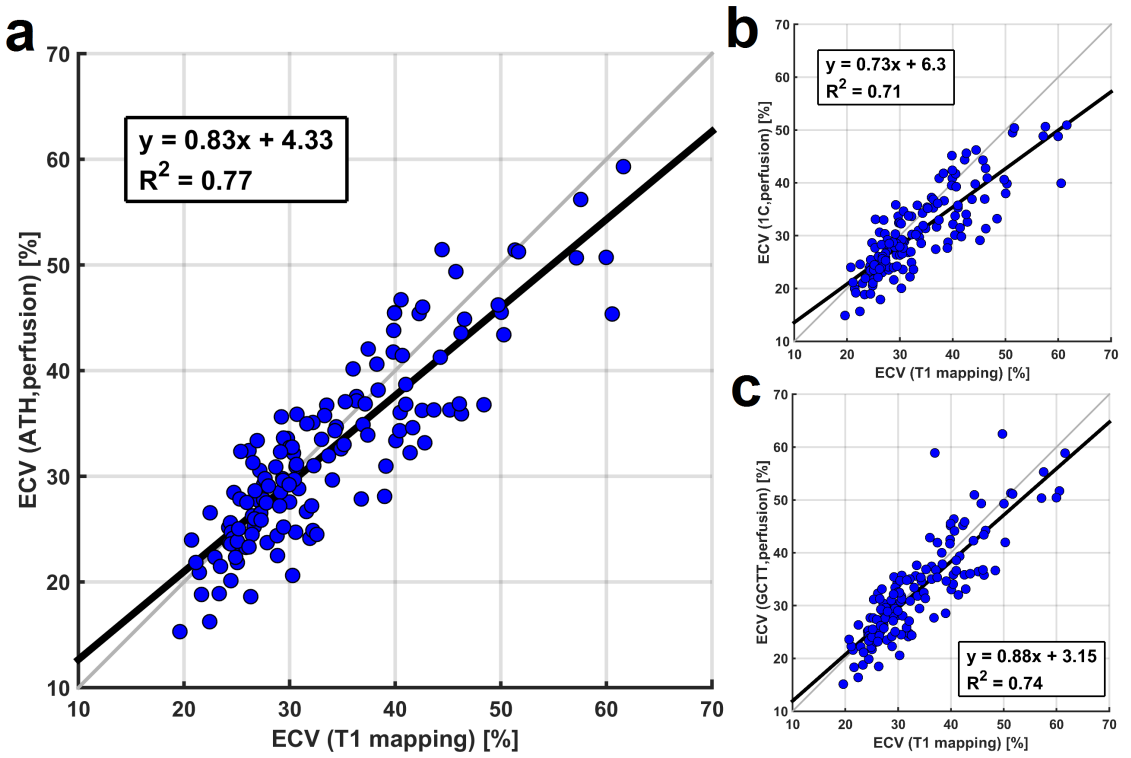

Figure 3.5: Correlations between ECV as derived by T_1 mapping and ECV estimates from all perfusion models in all sectors irrespective of cAIC factors. Apart from two outliers, ATH (**a**) and GCTT (**c**) estimates were very similar, while 1C (**b**) estimates were lower at the higher end of ECV values and generally more variable.

gion as pertaining to indicator kinetics. Results from our study comparing 1C and ATH models suggest that Gd-DTPA kinetics at rest, as studied in revascularized myocardial infarction patients, are in most cases permeability-limited. Similar observations were also documented for healthy volunteers by Broadbent et al. [16]. Concerning first-pass extraction, previous studies in healthy volunteers have resulted in estimates ranging from 82% with the ATH model [19] to 66% with the distributed-parameter model [16]. Values found in this study for fits with the ATH model lie within that range.

The observed decrease in E between ATH and GCTT models is equivalent to the combined observation of a slight increase in F_b and a more pronounced drop in PS. To what degree these changes represent physiological reality cannot be said with absolute certainty. A systematic increase of F_b in some proportion to the ratio of T_p/CTH can actually be expected, as significant parts of h may be assigned to very small transit times with the gamma-variate distribution. In fact, it is a feature of the GCTT model to become mathematically equivalent to a 2-compartment model in the limit of CTH $\rightarrow T_p$. This can lead to the inadvertent assumption of the vascular region as a well-mixed compartment and thus to a fundamentally different interpretation of the same data as with the ATH model. The problems of that assumption are known, and have already been referred to in the

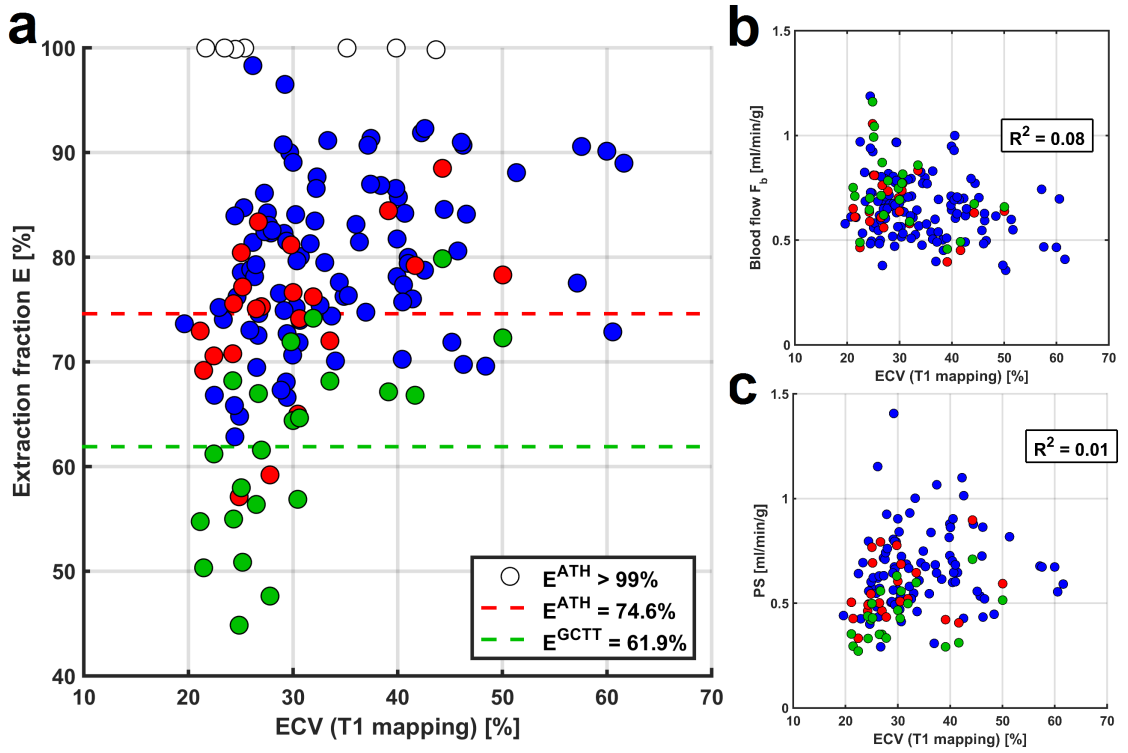

Figure 3.6: Comparison of T_1 mapping-based ECV with first-pass extraction E (**a**) as well as with blood flow F_b (**b**) and capillary permeability surface area product PS (**c**). Changes between ATH (red) and GCTT fit results (green) are highlighted for all three parameters as in Fig. 3.3, and they are most clearly visible as a significant drop in E (**a**) as indicated by the dashed lines. Again, all red points are only displayed for visualization purposes, while the final result of the proposed Akaike-based approach is the combination of blue and green points. The seven white points in (**a**) show the positions of sectors with an ATH estimate of $E > 99\%$, which were discarded and fit with the 1C model irrespective of cAIC values.

introduction in the context of the Tofts-model, one of them being the existence of a non-zero probability for indicator transit at $t = 0$, i.e. a non-zero value for $\partial_t R_F(0)$. Despite this being somewhat unphysiological (no indicator particle can traverse the vascular space with infinite velocity), it is also not possible to measure the transit time distribution for arbitrarily small transit times, given the time resolution of usual DCE-MRI data. However, closed-form models that respect the constraint of a minimum observable transit time do not exist without also applying the constraint of a minimum ratio of $T_p/\mathrm{CTH} > 1$. Note that this also relates to the reason why BAT and T_p where kept close to ATH estimates for the GCTT fits, namely in order to maintain comparability concerning the interpretation of parameter estimates.

Still, the results show that essentially all shapes of transit time distributions that are attainable by the GCTT model were observed in the patient data, which has also been

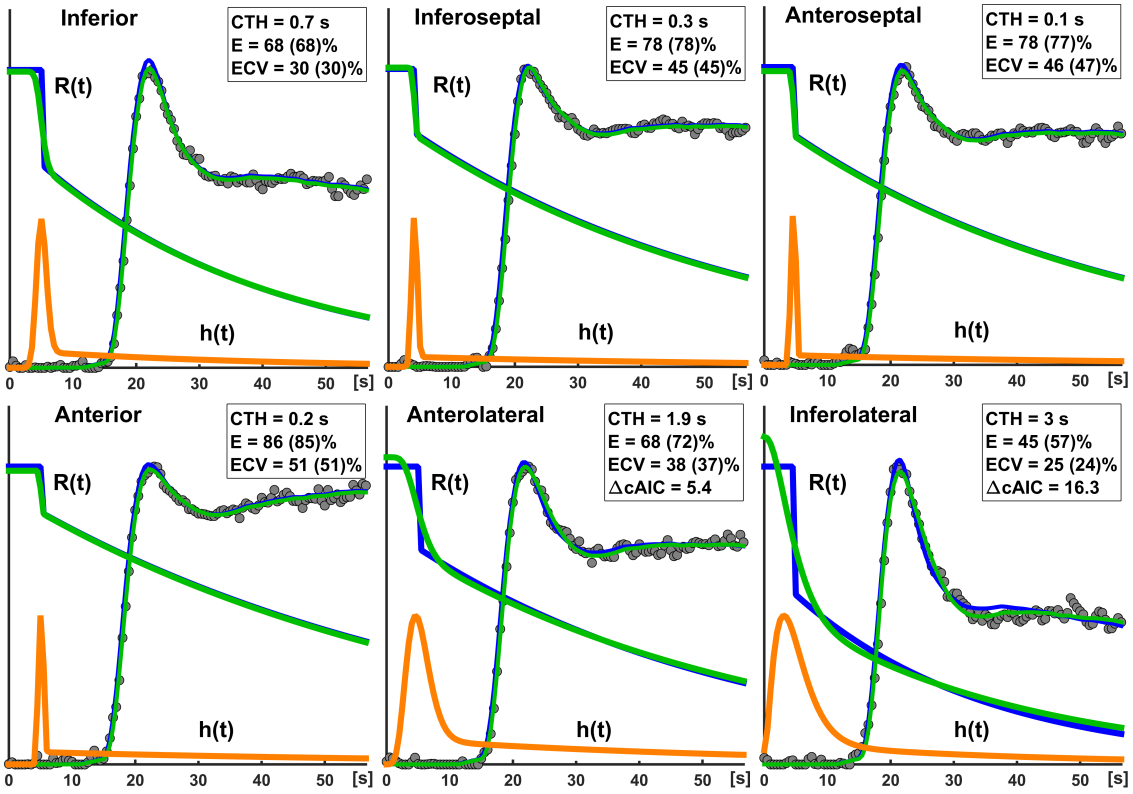

Figure 3.7: Perfusion analysis for all six sectors from a patient showing a typical pattern concerning the measurability of CTH in relation to pathology. All curves are scaled arbitrarily for visualization purposes. The ATH model fits and response curves ($R(t)$) are shown in blue, the respective GCTT curves are shown in green and the corresponding transit time distributions ($h(t)$) for the GCTT fits are shown in orange. Estimates of E and ECV are shown for the GCTT model, with the respective ATH estimates in brackets. Note that GCTT fits were only favored for the antero- and inferolateral sectors (ΔcAIC shown). For the other four sectors, CTH estimates were smaller and ΔcAIC values ranged from - 1.3 (inferior) to - 4.3 (anterior).

noted by Schabel for different tumor tissues [127]. These shapes are exponential distributions for CTH $\rightarrow T_p$, gamma-distributions for $T_p >$ CTH > 0 and delta-distributions for CTH $\rightarrow 0$. As expected, GCTT results with CTH $\rightarrow 0$ were rejected by the Akaike criterion, because they usually matched ATH results while carrying an additional fit parameter. Where measurable, CTH was found to be between 2 - 9 s, which is in the range of values seen in cerebral studies [103] and theoretically considered for the myocardium in [109]. Despite no direct inter-patient correlation between ECV and CTH, the observed pattern, in which significant effects of CTH were often only found in remote sectors, may have two explanations: The first would be physiological, namely that CTH is in fact lower in regions with cell damage/post-infarct trauma. This could e.g. suggest that flow heterogeneity is down-regulated in the infarcted areas to achieve a higher oxygen extraction

efficacy. A more probable explanation may however be methodological, namely that CTH may or may not be actually different between infarcted and remote regions, but the impact that either situation has on the dynamic curves of the infarcted region are largely attenuated by the predominant EES kinetics. This situation is visualized in Fig. 3.8, where GCTT results from the bottom panel of Fig. 3.7 are reproduced using the same AIF and fit parameters apart from CTH, which is varied between 0 and T_p. The resulting curves show that the effect of CTH is indeed much smaller for the anterior region, exhibiting higher ECV and first-pass extraction. In theory, the required SNR for observing a measurable, non-zero CTH becomes in fact arbitrarily high as E goes to 100%. Thus, although one might be tempted to embrace the physiological explanation given above, the authors hesitate to make such a claim based on the DCE-MRI data at hand and the subgroup of patients for which this pattern was observed.

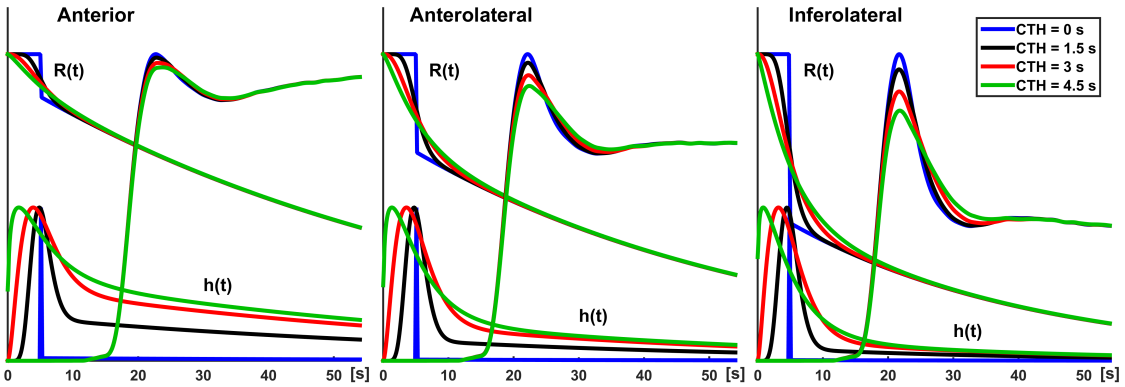

Figure 3.8: Visualization of the effects of varying flow heterogeneity at different tissue conditions. All three curves from the lower panel of Fig. 3.7 were reproduced using the same GCTT parameter estimates, but a variable CTH parameter. Extraction and v_e decrease significantly from left to right as already shown in Fig. 3.7, T_p was 5.1/5.1/4.9 s and v_p was 3.9/4.5/5.7% respectively. It can be seen that the effects of potential changes in CTH on the tissue curve are much less pronounced in cases of high first-pass extraction and large interstitial volume.

3.4.2 Extracellular Volume

Concerning the comparison of equilibrium ECV with the corresponding perfusion results, the lower perfusion-derived estimates at the high end of values may be explained by the fact that perfusion data was acquired for only 90 RR intervals: Since the response function R_F is only sampled for a time t_{max} between first inflow of indicator and the end of acquisition, the remaining outflow kinetics, i.e. the shape of R_F, need to be extrapolated from the tissue model on the basis of all previously observed indicator outflow. Thus, even the assumption of an apt model is no guarantee for correct volume estimates, as the actual acquisition time might not be long enough to sample a sufficient amount of transit time data to which to base the extrapolation. This has already been documented by Pack et al. [111], albeit with only four pathologic cases and a simpler model. Our data indeed

suggests that the perfusion method may estimate ECV up to 50% without a significant bias compared to the equilibrium MOLLI method (Fig. 3.4). Still, the observed variability between the two was quite large (Figs. 3.4/3.5) if compared to changes in ECV expected for diffuse diseases such as aortic stenosis or dilated/hypertrophic cardiomyopathy [125]. It should be noted however, that some significant sources for this variability may not lie within either method but within the comparison itself, e.g. the separate segmentation and motion correction. This aspect is important, because scan-time efficiency arguments favoring a perfusion method may become more relevant in these diffuse diseases, where the added diagnostic value of ECV assessment is assumed to be greatest [100], but absolute differences in ECV are relatively modest [125]. For these cases, the smaller the expected distribution volume, the less actual sampling time would be needed to assess it with a perfusion method according to the central volume theorem [151].

3.4.3 Limitations

Concerning the comparison of ECV measurements between perfusion and MOLLI equilibrium methods, the potential sources of error within the perfusion analysis probably outnumber the ones for the equilibrium method - despite shortcomings of the MOLLI sequence especially concerning estimation of T_1 in the blood pool [72]. Especially correct measurement of low-resolution AIF signals after the first pass and subsequent motion correction has proven challenging with the dual-sequence approach. In general, even small inaccuracies lowering the area under the AIF, e.g. due to insufficient motion correction, partial-volume effects or errors in estimation of the signal normalization constant S_0, may lead to overestimation of distribution volume parameters [151]. It is thus believed that, despite overall agreement with equilibrium ECV estimates, reported ECV values represent an upper limit for the perfusion method. Concerning CTH, no quantitative reference was available. Since the described deconvolution fit only accounted for bolus delay but not for concomitant bolus dispersion [129], reported CTH results are likely to include some overestimation. Further limitations concerning CTH are that the data at hand only allowed to investigate it under resting conditions, and that the assumption of gamma-distributed vascular transit times may still represent an oversimplification of reality. This, and the fact that small CTH estimates, leading to small differences between GCTT and ATH fits, were usually rejected by the Akaike criterion, may have limited the number of sectors for which CTH was deemed measurable. Also, the fast water exchange condition assumed herein might not be fulfilled at all times during the first-pass of Gd-DTPA, especially across capillary and cellular walls within the myocardial tissue.

3.4.4 Conclusion

This study presents the first simultaneous assessment of extracellular volume, blood flow, capillary permeability and myocardial transit time heterogeneity using perfusion imaging in patients after myocardial infarction. There are two core findings:

Myocardial capillary PS and CTH can be estimated simultaneously with F_b and ECV using DCE-MRI perfusion modeling. While PS was measurable in most cases, estimating CTH by introduction of an additional fit parameter was often only possible in remote

sectors, and therefore a relatively modest portion of the data. Nevertheless, hierarchical approaches such as the one presented herein may become important tools for identifying and resolving situations in which the use of a single tissue model implies a measurable under- or oversimplification of reality.

Secondly, myocardial ECV estimates derived from DCE-MRI data using a dual-sequence AIF correlated well with estimates from a conventional equilibrium method based on T_1 mapping. Thus, perfusion MRI using advanced modeling approaches may be a scan-time and contrast media dose-efficient alternative to methods based on T_1 mapping, despite higher implementation effort and post-processing complexity.

Chapter 4

Characterization of Coronary Morphology Using a Fourier Phase Method to Estimate Bolus Arrival Time

Based on the work published in:
KP Kunze et al., Proceedings of the 25th Annual Meeting of ISMRM, 3238 (2017).

4.1 Motivation

Bolus arrival time (or BAT) represents the path length of blood through the coronary arterial vasculature, and in the context of DCE-MRI is usually identified with the time shift between arterial input function and corresponding tissue enhancement curves. As described in Section 2.3.3, accurate estimation of the BAT is an important step in the process of model-constrained deconvolution analysis, and a neglect of arrival time effects is known to cause significant variations in flow estimates [21,75]. Methods estimating the BAT from time domain curve shapes by e.g. linear regression of baseline and upslope [30] have been shown to somewhat stabilize DCE-MRI deconvolution analysis [75], but lack precision especially in the presence of noise. Alternative approaches for iteratively extracting BAT estimates from the same deconvolution fit from which the response function R itself is calculated exist [16], but may introduce model-dependent biases. Due to these potential systematic differences between models concerning BAT estimation during the deconvolution process, independent estimation of arrival times is desirable especially for an hierarchical approach as described in Chapter 3 of this thesis. To that end, this section proposes an elegant and robust way of mapping the time shift between the two curves to a shift in the Fourier phase spectrum of R, instead of determining and comparing specific points (maximum/foot) of AIF and tissue curve.

The proposed approach is tested in a simulation study as well as in a small clinical control group, and a proof of principle combining DCE-MRI data with ^{18}F-FDG viability imaging is provided for a patient with collateralized coronary total occlusion (CTO). Proceeding in this fashion, this section proposes an understanding of PET as inherently quantitative in the signal magnitude domain and dynamic MRI with its superior time resolution as inherently quantitative in the time/frequency domain.

4.2 Methods

4.2.1 Low-Frequency Fourier Phase Reconstruction

A new technique is introduced to estimate bolus delay using the low-frequency phase spectrum of a direct Fourier deconvolution of AIF and tissue curve. It contains the following steps:

First, the tissue curve is padded to double length with a (linearly) decreasing tail to avoid discontinuity effects and shifted a further 10 s from the AIF for stability. Both curves are subsequently Fourier transformed and deconvolved analytically, i.e. divided in Fourier space, which results in phase and magnitude deconvolution spectra. In order to avoid high-frequency noise amplification, the phase spectrum is zero-padded for frequencies > 0.1 Hz, so that only the low-frequency components are examined, which contain the time-domain shift in the same way as all other phase components. As the shift information is contained solely in the Fourier phase spectrum, all components of the magnitude spectrum are set to unity. An inverse Fourier transform of the padded phase spectrum with all magnitudes set to unity is performed, resulting in a low-frequency phase reconstruction of the convolution kernel, i.e. the impulse response R_F. The bolus arrival time can be calculated from its main oscillation peak by subtracting positive and negative peak position (Fig. 4.1).

4.2.2 Simulations and Patient Study

A simulation study was performed testing accuracy, precision and superiority to similar approaches such as Time-To-Peak (TTP) analysis also in the presence of bolus dispersion. In order to better control the simulated degrees of arrival time and dispersion, only the blood-tissue exchange unit of the MMID4 model shown in Fig. 2.15(a/b) was used to create a reference tissue curve, and convolved afterwards with a gamma-variate kernel that simulated different BAT with and without dispersion. Simulations were performed for 100 iterations across a BAT range of 0 - 8 seconds at SNR = 40 (regional curves), SNR = 30 (single-voxel curves) and without the addition of noise to detect potential biases. If dispersion was included, it was set using a standard deviation for the gamma-variate kernel of ⅓ of the respective simulated BAT.

In order to provide an in-vivo proof of concept, five subjects without known cardiac disease and one patient with an LAD main branch coronary total occlusion (CTO) were scanned on a 3T PET/MRI scanner (Biograph mMR, Siemens, Erlangen). MRI imaging was performed using a 2D SR-FLASH sequence as described in Section 3.2 including motion correction, SCIC and signal non-linearity correction. The CTO patient received an additional simultaneous ^{18}F-FDG PET scan to test for myocardial viability with metabolic preparation by intravenous insulin loading [120]. Assessing the argument of post-processing simplicity, the motion corrected in-vivo DCE-MRI data were evaluated once with SCIC and full nonlinearity correction and once without any additional post processing.

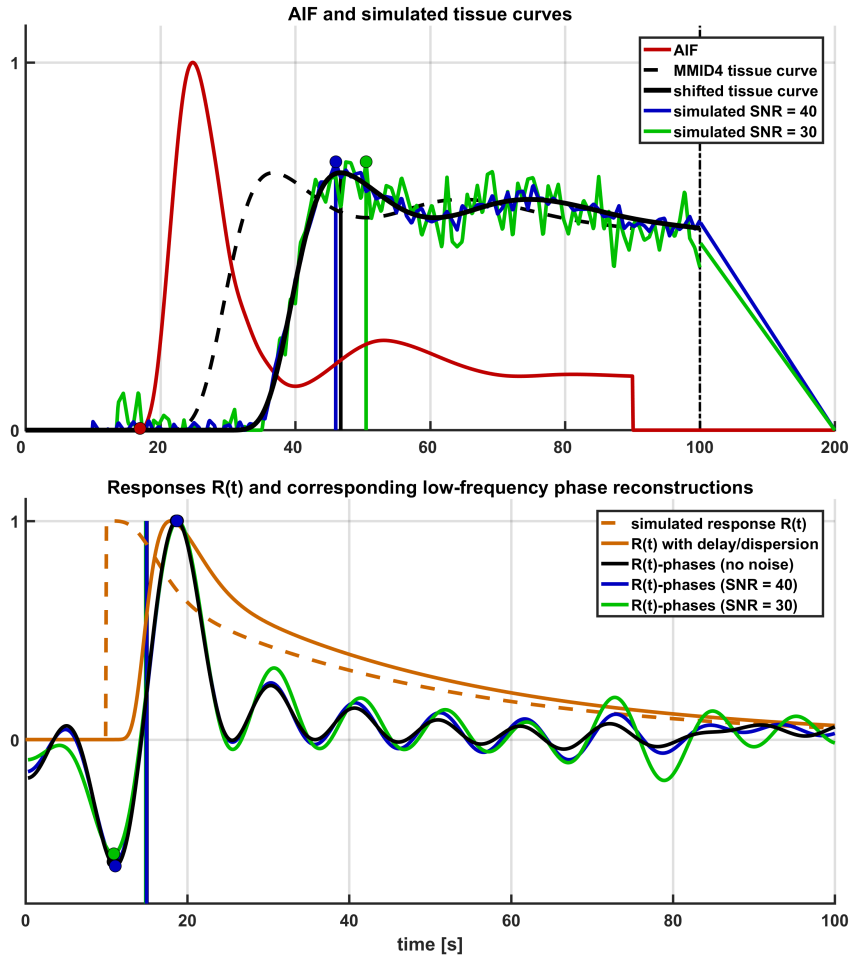

Figure 4.1: Calculation of the bolus arrival time from a low-frequency phase reconstruction of the response function R_F. The upper panel shows the measured and smoothed AIF, the MMID4 tissue curves simulated at two noise levels as well as an example for the variability of Time-To-Peak (TTP) estimates in the presence of noise. The bottom panel visualizes the appearance and analysis of the low-frequency phase reconstruction ("R(t)-phases") and its stability to different noise levels. Magnitudes of all curves are scaled in arbitrary units.

4.3 Results

Figures 4.2 and 4.3 visualize the simulation results. It can be seen that TTP analysis was not able to distinguish between delay and dispersion, introducing a bias proportional to the simulated dispersion factor. BAT estimates from the proposed Fourier technique remained virtually unaffected by dispersion (Fig. 4.2).

The standard deviations from all 100 simulation runs shown in Fig. 4.3 underscore the higher robustness of BAT measurements to TTP analysis at both noise levels. The clinical results from the control group showed a regionally homogeneous distribution of arrival

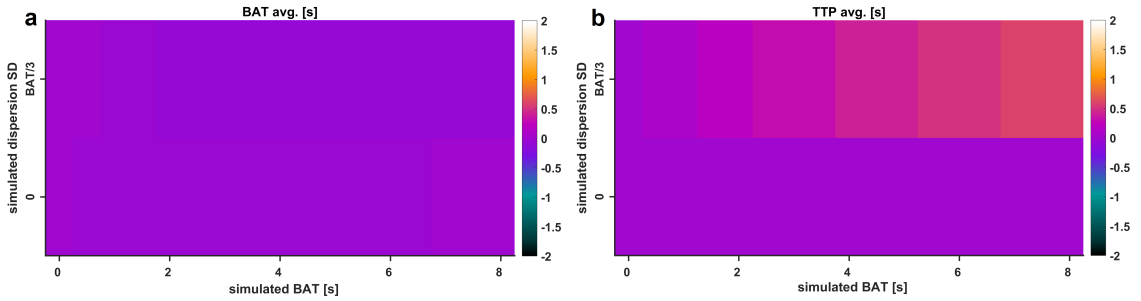

Figure 4.2: Noise-free simulation results visualizing a comparison of the proposed Fourier BAT estimation technique and TTP analysis with respect to distinguishing bolus delay and dispersion. Both plots (**a**/**b**) show simulation results without dispersion in the lower panel, and with dispersion in the upper one. While the average difference between simulated and estimated BAT is vanishing irrespective of concomitant dispersion (**a**), results of the TTP analysis are clearly dependent on both dispersion and delay (**b**).

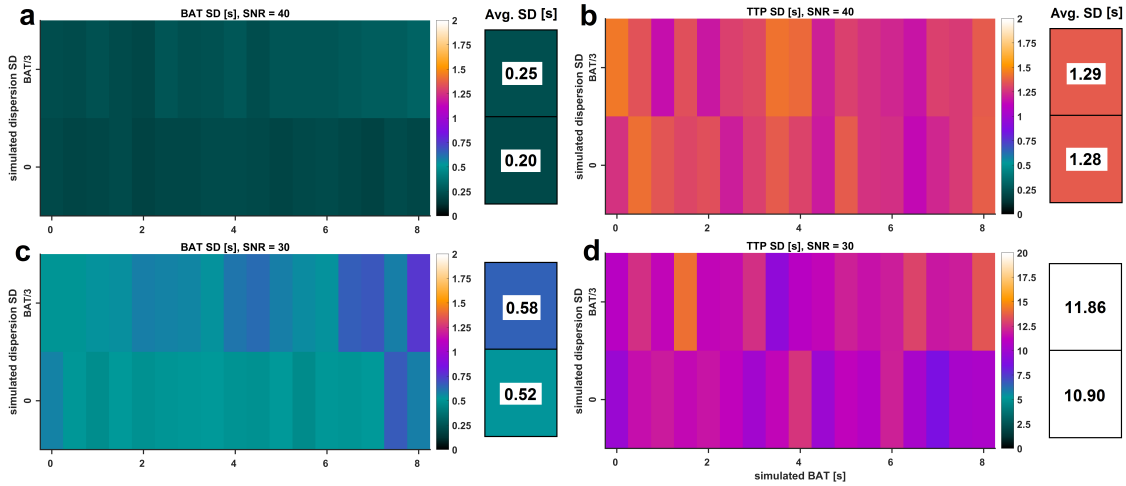

Figure 4.3: Summary of the simulation results with respect to precision at noise levels of SNR = 40 (**a**/**b**) and SNR = 30 (**c**/**d**). All color-coded values as well the numbers on the right represent the standard deviation of BAT (**a**/**c**) and TTP (**b**/**d**) estimates across all 100 simulation runs in seconds. Irrespective of dispersion and noise level, the proposed method for BAT estimation outperformed TTP analysis by almost an order of magnitude with respect to noise robustness.

times despite some longer BAT estimates in the inferior and lateral territories, leading to slightly higher averages there (Fig. 4.4(a)). The range of per-sector average BAT values for the control group was 2.53 s (anterior) to 3.55 s (inferior).

The CTO patient presented with a highly inhomogeneous BAT distribution ranging from 2.0 s (anterolateral) to 5.0 s inferoseptal). ^{18}F-FDG PET confirmed metabolic integrity of all regions despite a small inferior deficit (Fig. 4.5(a)). Invasive angiography results confirmed collateralization of the septum, bypassing an occluded LAD main branch and

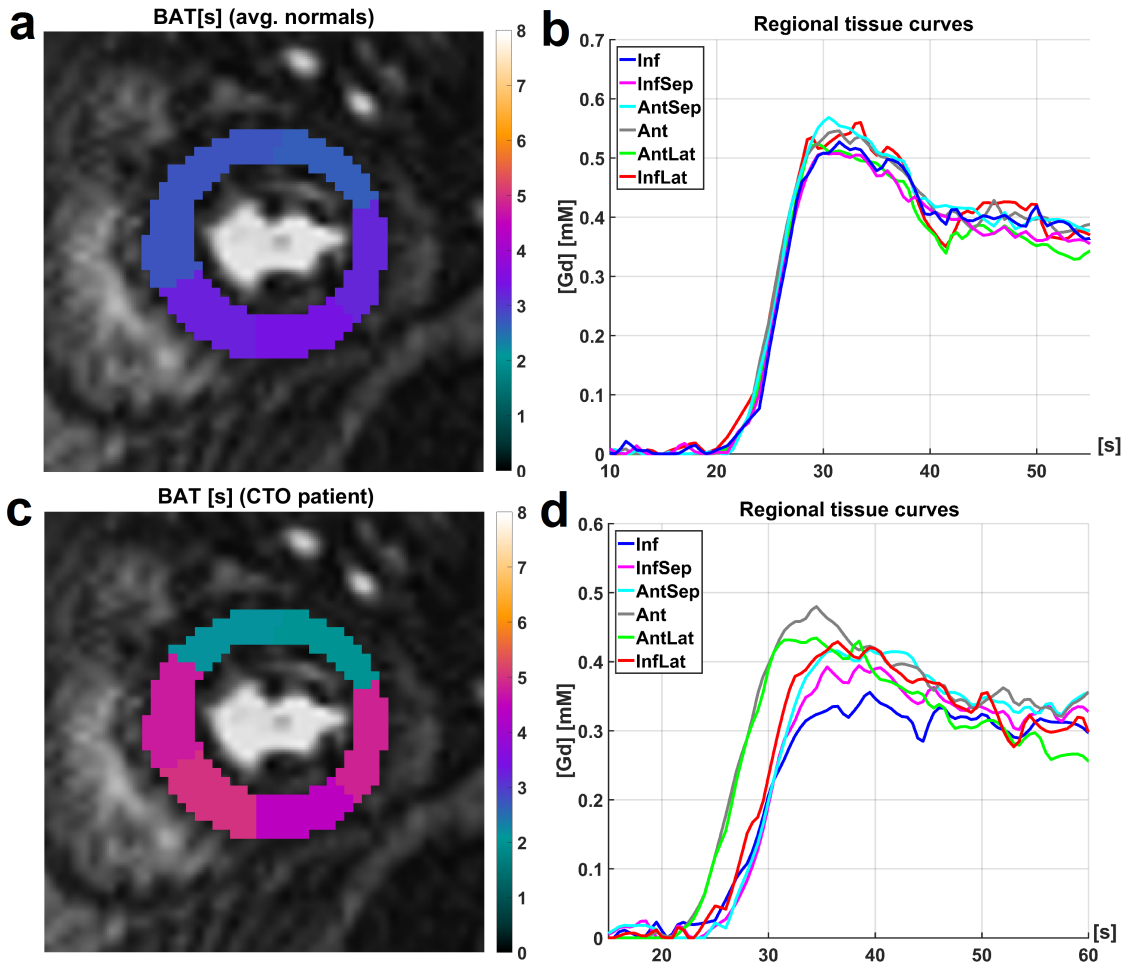

Figure 4.4: Results from regional analysis of the clinical data, showing sector-wise BAT results from the control group (**a**) and the CTO patient (**c**) as well as the six regional tissue curves for one example of the control group (**b**) and the patient (**d**). The color-coded segmentation in (**a**) represents an average BAT from all 5 controls for each respective segment.

thus leading to a longer coronary path length for blood reaching the septum. The previously reopened LAD diagonal branch conversely led to a shorter path length for blood reaching the anterior wall.

Fig. 4.5 also highlights the independence of the proposed method from SCIC and saturation correction, whereas the distribution of quantitative flow estimates greatly depended on these additional post-processing steps. Absolute perfusion flow F_p as calculated without SCIC and with saturation correction was globally overestimated and exhibited a significant septal-to-lateral gradient. BAT results, depending only on the low-frequency phase information, were unaffected by missing SCIC or signal saturation.

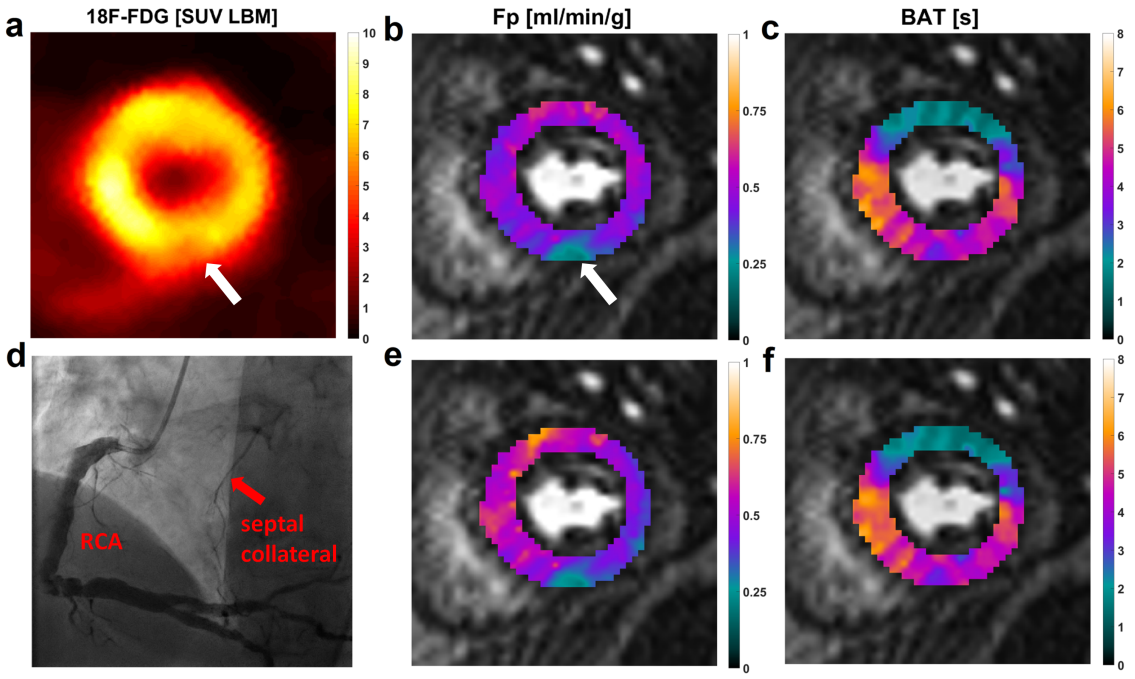

Figure 4.5: Results of the 18F-FDG PET scan (**a**) confirming metabolic integrity of the collateralized septal territories with the exception of a small inferior region, also exhibiting a small defect in plasma flow F_p (**b**). Panels on the right show results of the DCE-MRI analysis with (**b**/**c**) and without SCIC and saturation correction (**e**/**f**). Angiography results show the septal collateralization (**d**).

4.4 Discussion

A new method has been proposed to extract quantitative information from the phase spectra of DCE-MRI data with minimal additional post-processing. Understanding BAT estimation as a Fourier phase problem has highlighted the fact that it is a parameter essentially independent of linear (SCIC) and moderately non-linear (signal saturation) confounders to the quantitativeness of the DCE-MRI signal. Correcting for these in the context of absolute perfusion flow estimation involves significant user-interaction and post-processing complexity, which is an important obstacle for robustness and clinical applicability of quantitative DCE-MRI. This investigation has provided clinical evidence for the independence of BAT estimates from SCIC and correction of signal saturation when obtained using only Fourier phase components of DCE-MRI data. Conversely, quantitative voxel-wise flow results reported herein depended strongly on these corrections.

As a proof of principle, it has been shown herein that BAT and perfusion flow can be independently attributed to distinctly different physiological correlates: For BAT, invasive angiography confirmed the predicted prolongation of the coronary pathway for septal/inferior regions of the CTO patient. Here, only a small subregion of the one showing a BAT prolongation also presented with an actual perfusion deficit. The location and extent of this

smaller perfusion deficit was however co-localized with a decrease in metabolic activity as indicated by ^{18}F-FDG PET.

With respect to the robustness of BAT estimates, simulation studies presented herein have shown superiority of the proposed BAT estimation approach when compared to measures based on time-domain curve shapes. This has been shown with respect to noise contamination and especially with respect to the distinction between bolus delay and dispersion. In addition to the simulation study, homogeneity of BAT estimates from a control group without known CAD has confirmed the sensitivity of the parameter in a clinical setting.

4.4.1 Conclusion

Bolus arrival time estimates obtained using a low-frequency Fourier phase approach have been shown to robustly characterize path lengths within the coronary vasculature. The BAT represents a quantitative and robust DCE-MRI counterpart to tissue characterization using PET in the context of quantitative multimodality imaging. It is expected that more accurate assessment of the BAT will also benefit model-constrained deconvolution analysis of MRI perfusion data.

Chapter 5

Estimating Microvascular Perfusion Characteristics from Myocardial DCE-MRI Data with a Model-Independent Spline Approach

Based on the work published in:
KP Kunze et al., Proceedings of the 24th Annual Meeting of ISMRM, 2609 (2016).

5.1 Motivation

The relevance of parameters such as vascular transit time T_p and transit time heterogeneity CTH is given by the fact that their relationship is thought to play an important role in regulating the availability of oxygen to the myocardium, and that different ischemic (non-CAD) disease patterns may affect them [109]. As pertaining to the estimation of CTH, an important limitation of the investigation documented in Chapter 3 of this thesis is that the proposed fitting approach could only be tested in patients at rest. Therein, estimation of CTH using a gamma-capillary transit time model has been described as challenging, mainly due to the fact that information about the vascular space may not always be easily extracted from DCE-MRI data. As visualized in Fig. 3.8, the measurability of vascular parameters such as T_p or CTH depends to a large degree on the relative contribution of vascular signal to the overall tissue curve. A conceivable way to artificially increase this vascular signal contribution is pharmacological vasodilation, as it leads both to a lower first-pass extraction fraction [16] as well as to a measurably higher relative vascular volume [16,88]. While model-based estimation of CTH has proven challenging with resting-state data, the investigation of vasodilation stress states exhibiting higher vascular signal contributions may also enable model-independent assessment of microvascular flow characteristics. Model-independence would additionally address another important limitation referenced in Chapter 3 of this thesis, namely that the assumption of gamma-variate transit time distributions with the GCTT model may represent a significant oversimplification of reality.

This section therefore proposes a new B-spline based approach for deconvolution analysis of myocardial DCE-MRI perfusion data and reconstruction of the vascular transit time distribution h. It allows the model-independent quantification of vascular mean transit time and vascular transit time heterogeneity, assuming separability of vascular and extravascular DCE-MRI signal contributions (adiabatic exchange [82]). The presented algorithm was tested in simulations with respect to stability for the range of perfusion parameters expected under stress conditions, and 12 DCE-MRI patient datasets from adenosine stress examinations were analyzed.

5.2 Methods

5.2.1 Reconstruction of *h* from Spline-Based SVD

In addition to standard Tikhonov regularization, model-independent deconvolution techniques using singular value decomposition support the application of further constraints (see Section 2.3.4). These may include the requirement that SVD solutions be represented in terms of a 4th degree B-spline basis [69]. By controlling the placement and overall number of knots, i.e. the grid on which the resulting spline (the response function R) is evaluated, different portions of that spline may be forced to exhibit different degrees of smoothness or monotony.

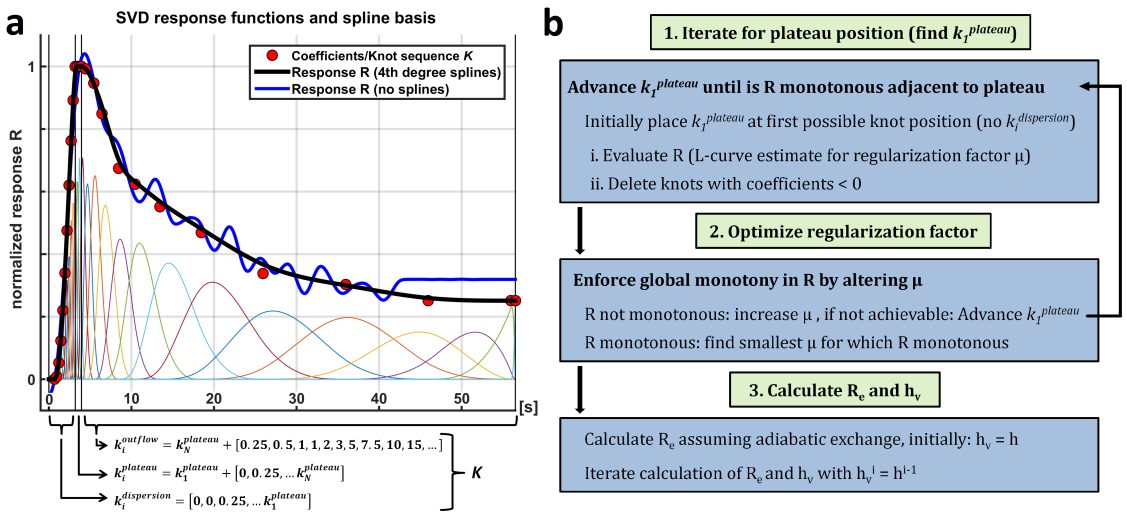

Figure 5.1: Iterative, spline-based reconstruction scheme for DCE-MRI response curve R and transit time distribution h. (**a**) Partitioning of the knot sequence is illustrated with the corresponding coefficients (red dots) and B-splines (narrow lines) constituting the resulting spline curve for the response R. Both the less oscillatory behaviour and the underlying sparsity of knots placed at the later phase of the outflow are shown in cmparison to a standard SVD. (**b**) Flow chart for the determination of knot sequence K and iterative reconstruction of the vascular transit time distribution h_v.

The approach presented herein is based on a sequence with varying knot density, ac-

commodating the expected features of a response curves in DCE-MRI data. The exact placement of knots was determined using essentially two criteria: First, the assumption of a global minimal transit time (0.5 s). It is supposed to represents a lower boundary to transit time information contained in data with the time resolution of usual DCE-MRI measurements. Second, the constraint that the outflow portion of the response curve be monotonous as required by basic indicator-dilution theory. Both criteria were met by partitioning the knot sequence K into three main constituents as shown in Fig. 5.1: First the subsequence $k^{dispersion}$, which characterizes the arrival time shift and the concomitant dispersion as a monotonous upslope. Second, the subsequence $k^{plateau}$ starting with a knot of multiplicity 3, essentially implying monotony and therefore no transit during the length of the plateau. Finally $k^{outflow}$, consisting of a dense distribution of knots during the vascular outflow phase adjacent to the plateau and a gradual decrease in knot density towards the slow-changing extravascular portion of R. As depicted in the flow chart in Fig. 5.1, the final knot sequence was determined by an iterative search for the optimal position of the plateau. The response was evaluated for the final knot sequence, and oscillations in h, i.e. the negative derivative of R, were minimized by adjusting the corresponding (Thikonov) regularization parameter.

After finding a suitable spline representation of R, an iterative method was implemented in order to separate vascular (R_v) and extravascular (R_e) contributions. Application of the recursion formula shown below using the adiabatic exchange condition (Eq. 5.1 [82]) was executed for 20 iterations:

$$R_e^i = Ee^{-\frac{EF_p}{v_e}t} \int_0^t h_v^i(t') e^{\frac{EF_p}{v_e}t'} dt' \tag{5.1}$$

$$h_v^{i+1} = -\frac{\partial}{\partial t} R_v = -\frac{\partial}{\partial t}(R - R_e^i) \tag{5.2}$$

For the recursion, extraction fraction E and EES volume v_e were globally fixed to values of $E = 55\%$ and $v_e = 18\%$ as expected at pharmacological stress [16]. The part of h_v corresponding to vascular indicator kinetics was integrated to yield T_p and CTH, which are defined as mean and standard deviation of h_v respectively. Mean and standard deviation of the preceding negative part of h corresponding to bolus dispersion were calculated to correct T_p for the BAT. The described iterative calculation of h_v is visualized in Fig. 5.2.

5.2.2 Simulations and Patient Study

To validate the resulting parameters, a simulation was executed varying parameters T_p and CTH using the GCTT model [127]. Parameters v_p, v_e, and E were fixed at 8, 18 and 55% respectively as expected at stress [16]. The simulated GCTT response was convolved with a measured input function after convolution with a gaussian kernel to simulate bolus dispersion and delay. Noise was added to the resulting tissue curve for an SNR of 50. In order to test the proposed approach in vivo, 12 DCE-MRI stress perfusion datasets were analyzed using slice average perfusion data from a mid-LV slice. Data were acquired using an ECG-gated SR-FLASH sequence on a 3T PET/MRI scanner (Biograph mMR, Siemens,

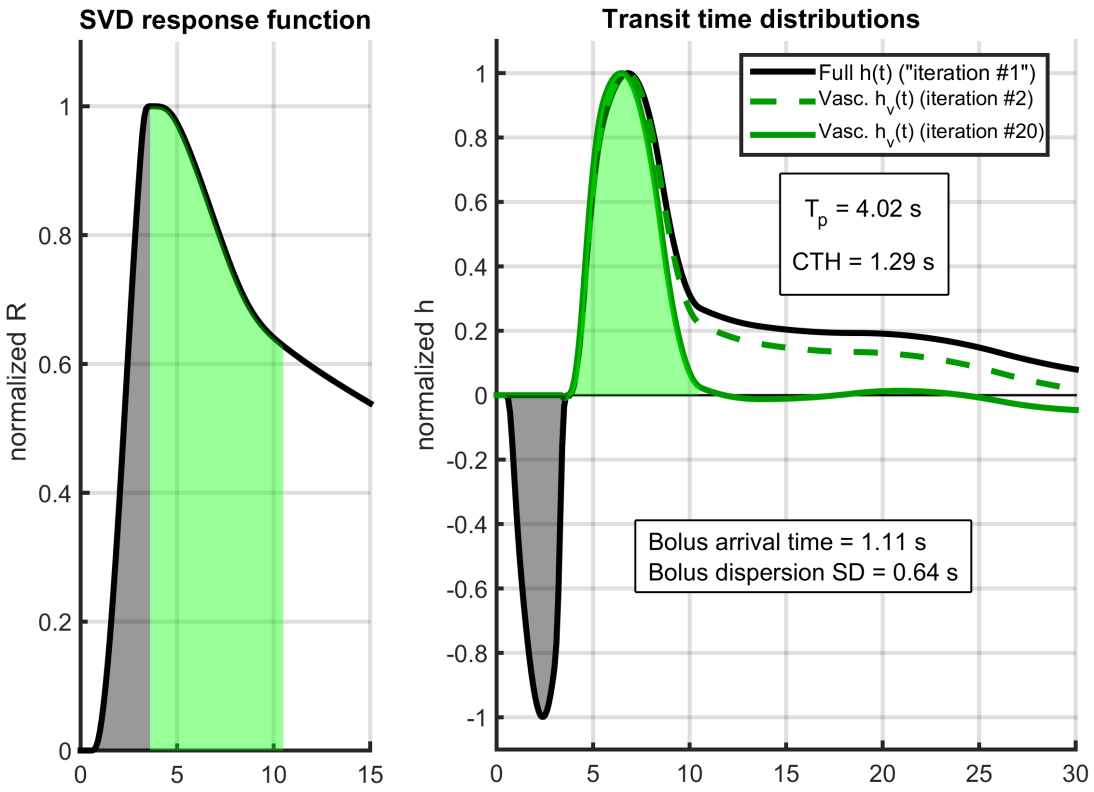

Figure 5.2: Visualization for the calculation of vascular transit time distributions h_v (green) by iteratively subtracting extravascular contributions from the full distribution h (black). Under exclusion of the dispersion phase (shaded black), the iterative approach effectively subtracts EES kinetics ($>10\,$s) with usually minor influences on the shape of the vascular portion (shaded green). The shaded areas represent the portion of the distribution from which mean and standard deviation are calculated by integration yielding T_p, CTH or dispersion characteristics.

Erlangen), with MRI sequence parameters, motion correction, SCIC and correction for signal saturation as described in section 3.2.

5.3 Results

The results of the simulation are summarized in Fig. 5.3. The algorithm was reliable for CTH as low as 1 s, however more likely to overestimate very small CTH. The algorithm was least reliable if confronted with combinations of much higher T_p and CTH than seen in the patient data. Estimation of v_p, which was not explicitly varied during the simulation, showed high stability with respect to variations in T_p and CTH.

The average results from the patient study for vascular transit time and transit time heterogeneity were $T_p = 3.10 \pm 0.55\,$s and CTH $= 1.21 \pm 0.36\,$s respectively, leading to an average T_p/CTH ratio of 2.55 ± 0.63. The individual results in Fig. 5.4 show a relatively

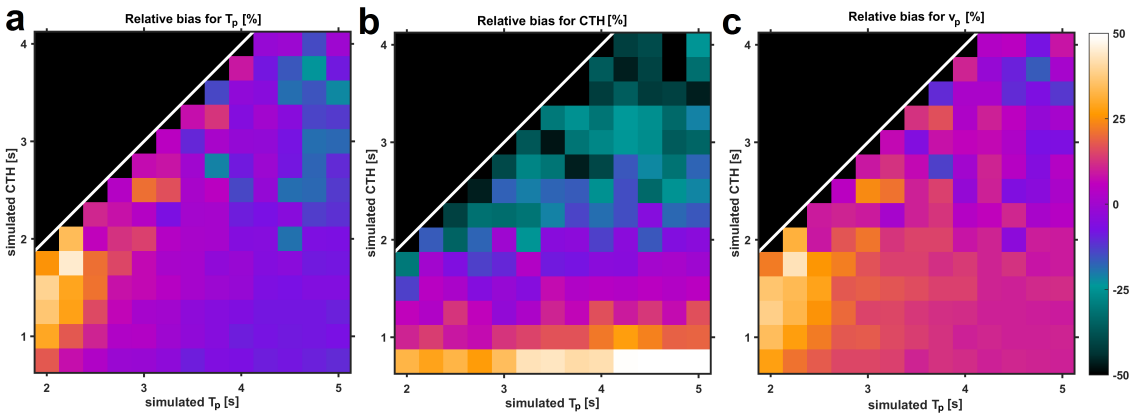

Figure 5.3: Simulation results for estimation of biases in the spline-based analysis of T_p (**a**), CTH (**b**) and v_p (**c**). Matrix values represent the relative bias in each parameter with variation of T_p (x - axis) and CTH (y - axis). Especially for higher values of CTH (**b**), underestimation of simulated values were observed. Note that v_p was fixed to 8% for the whole simulation study.

stable increase of CTH with T_p for the investigated range. One dataset was rejected due to a CTH estimate lower than the time resolution of the scan.

5.4 Discussion

5.4.1 Reconstruction of *h* from Spline-Based SVD

One of the main features of the presented spline-based approach is the iterative determination of a knot sequence that specifically accommodates DCE-MRI outflow data. While the impact of overall knot density has been studied for cardiac DCE-MRI data [69], the concept of taking into account fast-changing (vascular) and slow-changing (extravascular) portions of the response curve is novel. For the presented approach, this concept was combined with a separation of dispersion, plateau and outflow portions of the response curve. Therefore, the stabilized spline approach may also serve as a way to calculate bolus dispersion by effectively quantifying the deviation between a potential linear BAT shift and the actually observed dispersed upslope of R. However, quantification of bolus dispersion was not the focus of the simulation study, and the general limitations with respect to temporal resolution of DCE-MRI data apply to time parameters associated with the short pre-plateau phase of the dispersed response function.

In order to facilitate the calculation of vascular parameters from h as the negative derivative of the so-obtained response R, a recursive algorithm has been presented to extract the vascular portion h_v of the total transit time distribution. The recursion was based on iterative subtraction of an extravascular contribution R_e that was expressed under the adiabatic assumption originally formulated by St. Lawrence and Lee [136] and adapted for this study from Koh et al. [82]. As the vascular portion is the dominant part of h at least for stress data (Fig. 5.2), alternative approaches calculating mean (T_p) and standard

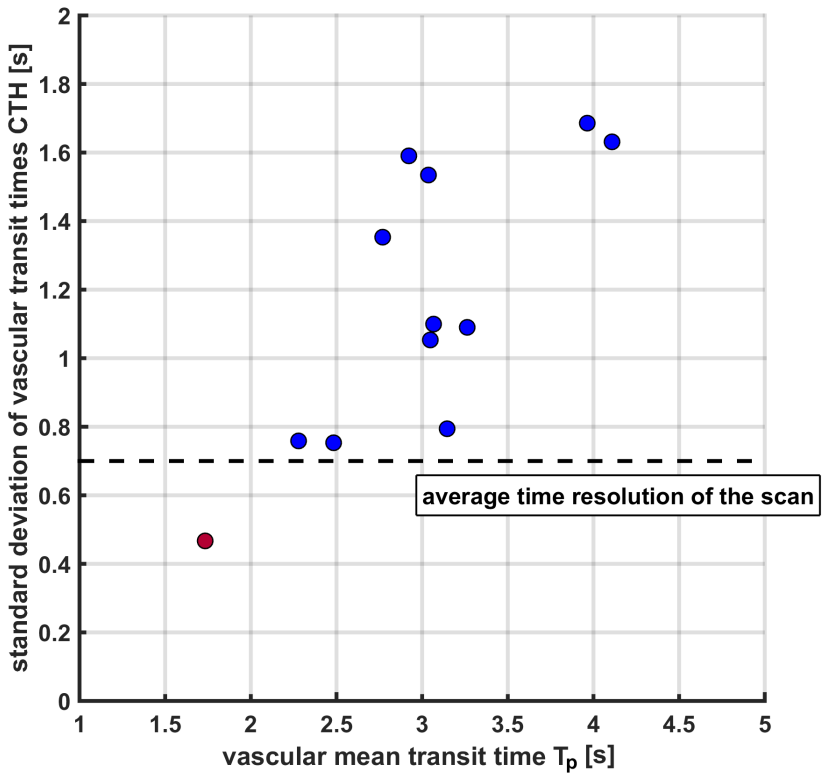

Figure 5.4: Comparison of vascular transit time heterogeneity CTH and mean transit time T_p for the 12 investigated vasodilator stress datasets. A gradual increase of CTH with T_p in a limited range between 1 - 2 s can be seen, with one case marked red exhibiting a lower CTH estimate than supported by the time resolution of the scan, i.e. 1/patient heart rate.

deviation (CTH) directly from h instead of explicitly calculating a vascular contribution may also be justified. Depending on the accuracy of estimates for E and v_e going into the recursion, explicit calculation of h_v may be favorable if extravascular contributions to h become significant. Note that higher relative extravascular contributions may pose a general limit to the measurability of vascular properties, and explicit model-based approaches such as the one evaluated in Section 3 may be unavoidable for separating vascular and extravascular contributions in resting-state perfusion data.

5.4.2 Simulations and Patient Study

The simulation studies have shown generally favorable results with respect to measurement biases for the range of parameters expected in patients at stress. However, especially for CTH, higher values exhibited more significant negative bias, which precluded application of the proposed approach to resting state data where such higher values can be expected. For the simulation study, the GCTT model was used instead of the MMID4 model, because the former characterizes CTH using only a single parameter, thereby simplifying a quantitative comparison of resulting vascular transit time distributions to the

simulated ground truth. Note that this does not necessarily infer a limitation on the ability of the proposed approach to aptly characterize vascular transit time distributions other than the simulated gamma-variate shape.

Results from the patient study have shown a gradual increase of CTH with T_p for the relatively small number of patients under investigation. The spectrum of absolute CTH values may be seen as concordant to the higher resting-state results reported in Section 3, as a shortening of transit times and their heterogeneity can in fact be expected at stress [109,124]. However, while the resting state values for CTH from Section 3 can be seen as reflecting an actual physiological state, the values reported herein correspond to the use of an exogenous vasodilating agent. It is therefore debatable to what degree findings from such data are clinically informative, given that they are obtained by creating an non-physiological dilation state of the vasculature. While vasodilator stress testing is established for investigating the potential maximum volumetric throughput of the myocardial vascular bed, vascular states exhibiting hypothetical maladaptive or "malignant" CTH [109] may be better characterized in resting state or in combination with actual patient exercise.

5.4.3 Conclusion

A new, model-independent algorithm has been presented to estimate myocardial mean transit time and transit time heterogeneity from DCE-MRI perfusion data without the necessity to assume a specific vascular model. Simulation results as well as clinical data suggest the possibility for model-independent estimation of microvascular perfusion characteristics beyond flow at vasodilator stress. Higher values of T_p and CTH may however require support by explicit vascular models, if they are at all retrievable from clinical DCE-MRI data, that also exhibit significant extravascular signal contributions.

Chapter 6

Myocardial Perfusion Quantification Using Simultaneously Acquired $^{13}NH_3$-Ammonia PET and DCE-MRI

Based on the work published in:
KP Kunze et al., Magnetic Resonance in Medicine, doi: 10.1002/mrm.27213, 2018.

6.1 Motivation

Myocardial perfusion imaging plays an important role in clinical decision making today. Its capabilities in the assessment of coronary artery disease using nuclear medicine techniques such as SPECT and PET are the current reference standard for clinical practice and research. In addition, numerous studies have shown the added clinical value of absolute quantification of blood flow or myocardial perfusion ratios in clinical ischemia [48]. While magnetic resonance perfusion imaging is continuously gaining acceptance [31], the clinical aptitude of MRI methods for absolute quantification of myocardial perfusion has not yet been established in a way comparable to PET [63,106]. Therefore, this study provides an assessment of comparability, systematic differences, as well as potential synergies of Dynamic Contrast-Enhanced MRI and $^{13}NH_3$-ammonia PET with respect to quantitative myocardial perfusion imaging. Both methods are discussed for the first time on the basis of simultaneously acquired PET/MRI perfusion data in a cohort of patients with known or suspected CAD.

The manuscript investigates a number of aspects related to quantitative DCE-MRI analysis, including acquisition of the arterial input function and signal nonlinearity modeling using dual-sequence [46] and theory-based [17] methods, as well as a discussion of the widely-used Fermi deconvolution method [61] with respect to regional perfusion quantification. Potentially useful combinations of simultaneously acquired PET and MRI perfusion data are highlighted for clinical example cases as well as by application of DCE-MRI tissue models allowing for estimation of microvascular parameters beyond perfusion flow [16], such as myocardial plasma volume, capillary permeability-surface area product, first-pass extraction fraction and extracellular volume [88].

Additionally, a discussion of some usually underappreciated systematic differences between flow estimates from DCE-MRI and PET is given. Besides time resolution and data structure, this refers mostly to the fact that all conventional MRI contrast agents distribute extracellular, which makes DCE-MRI flow estimates sensitive to microvascular hematocrit [134]: Although the exchange of water across cellular walls in DCE-MRI leads to an interaction of all tissue compartments with the extracellular agent, the dynamic reference volume for flow estimation is still blood plasma. Conversion between plasma flow (F_p) and blood flow (F_b) is often executed implicitly by ignoring hematocrit normalization and producing blood flow estimates under the assumption of equal tissue ($\mathrm{hct_t}$) and arterial hematocrit ($\mathrm{hct_a}$). While this may not necessarily present an important limitation for MRI perfusion quantification, this manuscript additionally explores the possibility of combining simultaneously acquired MRI-derived plasma and PET-derived blood flow in order to estimate tissue hematocrit, which may be relevant for all imaging applications using extracellular contrast agents.

6.2 Methods

6.2.1 Study Protocol

A total of 29 patients with known or suspected CAD were prospectively recruited. Exclusion criteria were any contraindications to undergoing contrast-enhanced MRI examinations at 3T. Written and informed consent was given by all patients, the study was approved by the local ethics board and performed in accordance with the declaration of Helsinki. All patients underwent simultaneous PET/MRI stress/rest perfusion examination on a clinical 3T PET/MRI scanner (Biograph mMR, Siemens Healthcare, Erlangen, Germany), the imaging protocol is shown in Fig. 6.1. For patient comfort and logistical reasons, adenosine-induced stress scans were executed first followed by scanning at rest.

Table 6.1: Patient Characteristics

Total	29 (100)
Male	23 (79)
Diabetes	11 (38)
Insulin dep.	2 (7)
Smoker	3 (10)
Age [y]	66 ± 10
HR stress [bpm]	86 ± 11
HR rest [bpm]	67 ± 11
Sys. BP [mmHg]	132 ± 16
Dia. BP [mmHg]	76 ± 9

Values are n (%) or mean ± SD. HR = heart rate, BP = blood pressure.

6.2.2 PET Image Acquisition

For both rest and stress, dynamic list mode imaging with 3D PET mode started briefly before a slow (30 s) bolus injection of 233 ± 81 MBq $^{13}NH_3$. Attenuation and scatter correction were applied as previously described [91]. In addition to a standard Dixon fat-water separation technique for generation of attenuation maps, potentially missing attenuation data from the arms due to a smaller MRI field of view were recovered using the maximum likelihood reconstruc-

tion of attenuation and activity (MLAA) method [108]. Image reconstruction used a 3D attenuation-weighted ordered-subsets expectation maximization (AW-OSEM 3D) iterative reconstruction algorithm with three iterations and 21 subsets, Gaussian smoothing with 4 mm FWHM, matrix size 344 x 344, and zoom 1. Dynamic frames were reconstructed as follows: 12 x 10 s, 4 x 30 s, 4 x 1 min, 1 x 2 min.

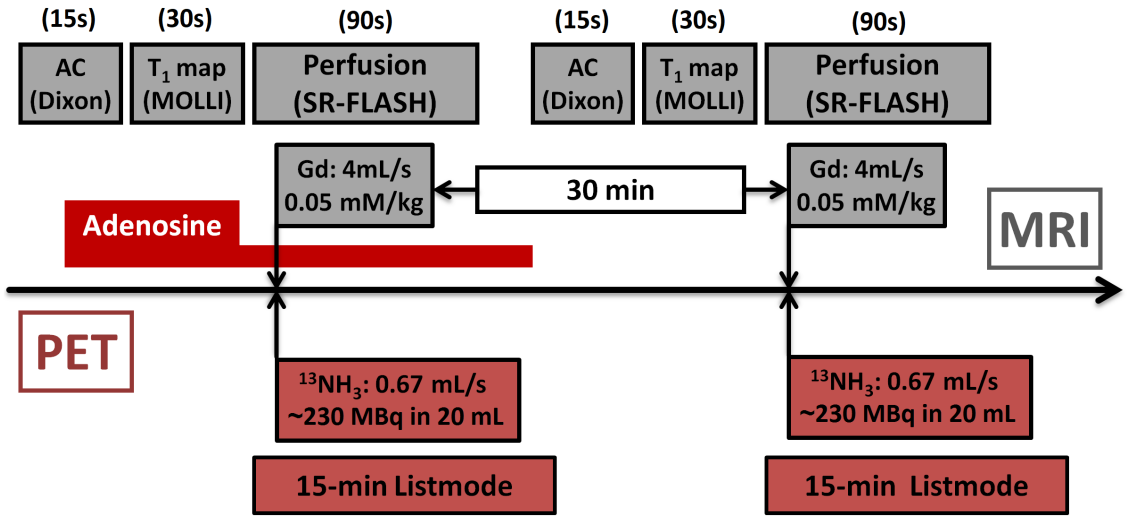

Figure 6.1: Schematic representation of the simultaneous PET/MRI perfusion protocol.

6.2.3 PET Image Analysis

A previously validated [104,106] three-compartment model including corrections for motion, partial volume and spillover [63] was used to analyze dynamic $^{13}NH_3$ data. Blood flow was estimated directly from K_1 assuming no significant difference in $^{13}NH_3$ extraction between rest and hyperemia for the limited range of clinically observed blood flow rates. No explicit correction for $^{13}NH_3$ blood metabolites was executed as these have limited impact on extraction rates [104]. Absolute regional flow values were generated as a transmural volume model of the complete left ventricle. DICOM images delineating blood flow, spatially matched to the original PET data, were created to facilitate the comparison to MRI results as accurately as technically achievable.

6.2.4 MR Image Acquisition

For MRI perfusion data acquisition, the same 2D Saturation Recovery FLASH prototype sequence was used in combination with a dual-sequence approach as used in Chapter 3. High-resolution perfusion images were acquired during 90 consecutive RR intervals in three short-axis slices in the left-ventricular myocardium. Each stack of high-resolution acquisitions was preceded by a single low-resolution acquisition with altered imaging parameters at a basal slice position [46]. Bolus injection of 0.05 mmol/kg Gd-DTPA (Magnevist, Bayer Healthcare, Germany) at 4 mL/s was started after the first 10 RR intervals with image ac-

quisitions and followed by a 20-mL saline flush. Typical imaging parameters for high- and low-resolution perfusion acquisitions were used as reported in Section 3.2.2. Prior to all perfusion measurements, myocardial and blood T_1 were estimated using a MOLLI prototype sequence [95] with a 3(3)3(3)6 scheme [93] and parameters as reported in Section 3.2.5.

6.2.5 Perfusion MR Image Analysis

Retrospective motion correction for MOLLI T_1 data was performed inline on the scanner as implemented by the vendor. Motion correction for both high- and low-resolution image series and Surface Coil Intensity Correction were executed as described in Section 3.2 and shown in Fig. 6.2. T_1 and Gd-DTPA concentration curves were calculated from enhancement curves similar as described in [9] and [16]. Therefore, SR-FLASH signal equations were numerically inverted to correct for signal saturation in both blood pool and myocardium via Bloch-equation simulations of the SR-FLASH k-space acquisition. Normalization constants S_0 between MRI signal and R_1 evolution were calculated using pre-injection baseline signals and corresponding MOLLI R_1 estimates. S_0 was calculated only for the rest scan in order to avoid potentially less reliable native baseline signals [17] and used for all myocardial signal curves from both rest and stress scans after normalizing SCIC reference values. Signal-to-concentration modeling for low-resolution AIF images was executed as described earlier using only proton-density-weighted image signal and no externally measured T_1 estimates [11]. An additional AIF was taken from the high-resolution images using a comparable region of interest from a similar slice position as the low-resolution AIF and corrected for signal saturation in the same way as the myocardial curves. Flows and AIFs were converted between whole blood and plasma reference volumes using arterial hematocrit ($\mathrm{hct_a}$) and tissue hematocrit ($\mathrm{hct_t}$) fractions [13,134], and a tissue-to-arterial hematocrit ratio (d_{hct}) was defined in analogy to Eq. 2.28:

$$AIF_p = \frac{AIF_b}{1 - hct_a}, \quad F_b = \frac{F_p}{1 - hct_t}, \quad d_{hct} = \frac{hct_t}{hct_a} = (1 - \frac{F_p}{F_b})/hct_a \tag{6.1}$$

Deconvolution was executed with plasma as reference volume (AIF = $\mathrm{AIF_p}$, Flow = F_p), explicitly emphasizing the dependence of DCE-MRI blood flow estimates F_b on tissue hematocrit [134]. Arterial hematocrit was globally assumed to be 0.42 [16] and both the assumptions of $\mathrm{hct_t} = 0$ ($d_{hct} = 0\%$, $F_b = F_p$) and $\mathrm{hct_t} = \mathrm{hct_a}$ ($d_{hct} = 100\%$, $F_b \approx 1.72 \cdot F_p$) were tested against PET blood flow results. In an additional step, tissue hematocrit fractions were calculated directly from the cohort-wide comparison of MRI-derived F_p and PET-derived F_b results according to Eq. 6.1.

6.2.6 Perfusion MRI Data Modeling

All AIFs and tissue curves were linearly interpolated to uniform time steps of 0.5 s, and bolus arrival times were determined by iterative deconvolution analysis across all possible values as described in Section3.2. In addition to a simple upslope analysis [14], model-free deconvolution of Eq. 2.29 was implemented based on singular-value decomposition using standard Tikhonov regularization and a first-order differential operator as a side

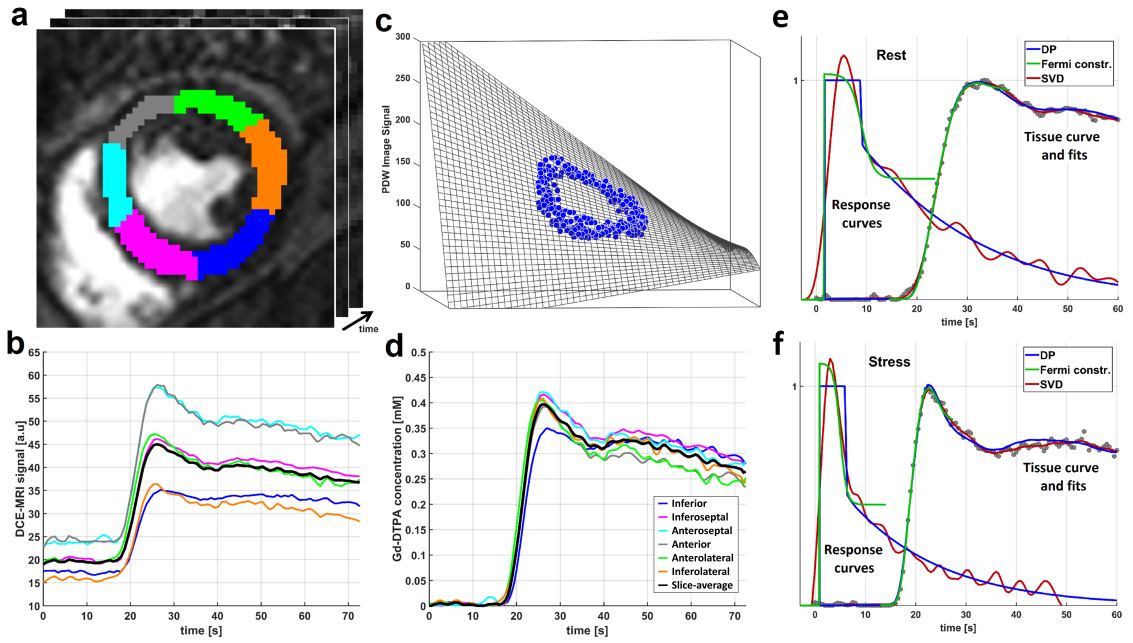

Figure 6.2: Visualization of MRI surface coil intensity correction and deconvolution modeling. Segmented stack of short-axis images after motion correction (**a**) and 2D surface fit to the corresponding segmented portion of the proton-density-weighted image (**c**) are shown with corresponding enhancement curves before (**b**) and after (**d**) SCIC and signal-to-concentration modeling. Typical examples for fits and response curves are shown for rest (**e**) and stress (**f**) states on a normalized scale.

constraint in combination with an L-curve criterion [57]. Model-constrained deconvolution was executed using three different approaches: First, the two-region Distributed-Parameter (DP) [134] model was applied in combination with a single-compartment (1C) model as previously described [16], replacing DP with 1C fit results in cases where the former yielded vascular transit times smaller than the temporal resolution of the scan. Second, an unconstrained Fermi-function model [3,67] was implemented using an interstitial loading term to account for extravasation [61]. Thirdly, the same Fermi analysis was implemented without allowing indicator transit at $t = 0$ to ensure physiological plausibility and fit stability. Implementation of Fermi shape functions representing the response R_F, augmented by a constant I-term for extravasation of contrast agent [61], was executed as described in Eq. 2.46. Here, the leakage term represents indicator extraction into the extravascular space assuming no backflow, i.e. infinite transit times. A so-defined Fermi model may be seen as a direct extension to previously described compartmental- or plug flow uptake (CTU/PTU) models [134]. Vascular outflow statistics are governed by a cumulative logistic distribution with a mean T_p and a standard deviation $\sigma\pi/\sqrt{3}$. The underlying distribution of transit times h, being the negative derivative of R_F [151], contains about 99% of indicator transit events in the interval of three standard deviations around the mean, i.e. $\pm 3\sigma\pi/\sqrt{3}$ around T_p. Therefore, the physiological constraints that there be (close

to) no indicator transit at time zero, i.e. $h(t = 0) \approx 0$, and that 99% of transit time events occur for $t > 0$ may be implemented by changing the parameterization in Eq. 2.46 according to:

$$R_F^{Fermi+I}(t) = F_p \cdot \left[\frac{1-I}{1+e^{\frac{t-T_p}{\sigma}}} + I \right] \quad \rightarrow \quad F_p \cdot \left[\frac{1-I}{1+e^{\alpha(\frac{t}{\tau}-1)}} + I \right] \tag{6.2}$$

Setting a lower bound for the parameter $\alpha = \tau/\sigma$ of $3\sigma\pi/\sqrt{3}$ leads to a mean transit time that is always larger than 3 times the standard deviation of transit times, fulfilling the physiological plausibility constraints described above. Akin to the described approach, a constraint for the similar Gaussian distribution has already been proposed by Koh et al. in combination with a more complex adiabatic tissue homogeneity model [82].

6.2.7 Data Fusion and Statistics

$^{13}NH_3$-ammonia data and DCE-MRI images were processed separately and combined in a final step, in which volumetric 3D flow values from PET were fused with corresponding 2D MRI perfusion slice positions and manually aligned if necessary. From the so-obtained 2D PET slices, $^{13}NH_3$ blood flow estimates were taken at the locations of the DCE-MRI segmentation (Fig. 6.2(a)) either as an average of each individual sector ("sector-wise") or as an average of across all sectors ("slice-average"). Comparisons of the so-obtained and co-registered flow results were executed for one mid-ventricular short-axis slice per patient. MRI segmentation was performed according to the standard 17-segment AHA model, the described fusion and segmentation therefore resulted in six regional and one slice average flow estimates per patient per modality. All significance tests were executed as two-sample t-tests with 5% significance level. All code for data post-processing was custom written in IDL 8.1 (Harris, Melbourne (FL), USA) and Matlab R2016a (Mathworks, Natick (MA), USA).

6.3 Results

Baseline characteristics of the patient cohort are shown in Table 6.1. Stress and rest datasets were rejected for one patient due to irregular ECG triggering and one stress dataset was rejected due to no apparent reaction to adenosine according to heart rate and blood pressure. Three of the remaining patients did not complete the scan at rest, leading to a total of 25 rest and 27 stress datasets. Perfusion flow results from both modalities were compared on a cohort-average, slice-average and sector-wise basis. All reported DCE-MRI results correspond to the use of the high-resolution, saturation-corrected AIF if not stated otherwise.

6.3.1 Cohort-Average

All cohort-average results are summarized in Table 6.2. DCE-MRI flow results are shown as plasma flow F_p and blood flow F_b, the latter converted under the common assumption of equal tissue- and arterial hematocrit. DCE-MRI approaches yielded overall similar

Table 6.2: Cohort-Average Results for Flow, Hematocrit, and Microvascular Parameters

	F_p Rest	F_p Stress	F_b Rest $\mathbf{hct_t = hct_a}$	F_b Stress $\mathbf{hct_t = hct_a}$	MPR	Diff. to $^{13}NH_3$
$^{13}NH_3$			0.78 ± 0.23	1.89 ± 0.41	2.53	$p = 1.000$
SVD	0.59 ± 0.14	1.22 ± 0.31	1.02 ± 0.25	2.11 ± 0.31	2.05	$p = 0.012$
Fermi	0.57 ± 0.15	1.26 ± 0.43	0.98 ± 0.25	2.17 ± 0.74	2.17	$p = 0.074$
Fermi$_c$	0.54 ± 0.13	1.15 ± 0.30	0.94 ± 0.23	1.98 ± 0.49	2.09	$p = 0.022$
DP	0.54 ± 0.14	1.13 ± 0.30	0.93 ± 0.24	1.94 ± 0.51	2.11	$p = 0.036$
	d_{hct} Rest	**d_{hct} Stress**	**Diff. S/R**			
SVD	53%	82%	$p = 0.003$			
Fermi	61%	80%	$p = 0.053$			
Fermi$_c$	67%	92%	$p = 0.005$			
DP	70%	95%	$p = 0.008$			
Avg.	63%	89%				
(DP)	**Rest (SD)**	**Stress (SD)**	**Diff. S/R**			
PS	0.70 (0.20)	0.93 (0.27)	$p < 0.001$			
v_p [%]	7.4 (1.6)	9.2 (1.8)	$p < 0.001$			
v_e [%]	16.8 (3.2)	18.2 (4.7)	$p = 0.2$			
E [%]	71.6 (7.4)	55.5 (8.4)	$p < 0.001$			

Values are mean ± SD, all flows and PS in units of mL/min/g. PET results are shown as blood flow F_b, DCE-MRI results are shown both as plasma and blood flow under the assumption $hct_t = hct_a$. Significance levels are provided for differences to PET MPR, between stress and rest values of tissue hematocrit, and for additional DP model parameters.

flow estimates, and were higher than PET F_b especially at rest if converted under the assumption of $hct_t = hct_a$. Consequentially, DCE-MRI perfusion ratios were significantly lower than for PET. Higher MPRs for the unconstrained Fermi approach were observed in combination with very a high standard deviation of stress results and a number of high-flow outliers in slice-average and regional results. Combining MRI-derived F_p and PET-derived F_b estimates, cohort-average plasma-to-blood conversion factors at rest and stress were calculated according to Eq. 6.1 on the basis of slice-average results. The obtained estimates of tissue-to-arterial hematocrit ratios were significantly different between rest and stress for all DCE-MRI models, averaging at $d_{hct} = 63\%$ and $d_{hct} = 89\%$, respectively. Due to the global assumption of arterial hematocrit $hct_a = 0.42$, this is equivalent to the finding of a myocardial tissue hematocrit of 0.26 at rest and 0.37 at adenosine stress. Additional data

shown in Table 6.2 represent cohort-average results for microvascular parameters from the DP model analysis. In response to adenosine stress, significant increases in plasma volume and PS were observed. First-pass extraction fraction decreased significantly while myocardial extracellular-extravascular volume did not change significantly.

6.3.2 Slice-Average

High correlation factors between slice-average flow results from PET and all DCE-MRI deconvolution approaches were observed, which were $R^2 = 0.80/0.79/0.76/0.82$ for SVD/DP/Fermi/constrained Fermi analysis respectively. Correlations and Bland-Altman plots are shown for the latter as a representative example in Figure 6.3. Conversion of MRI-derived plasma to blood flow is visualized using correlation plots for the two extreme cases of assuming $hct_t = 0$ and $hct_t = hct_a$. For $hct_t = 0$, equivalent to assuming no red blood cells in the vascular bed, flow values vastly underestimated PET-derived blood flow (Fig. 6.3(a)). Assumption of equal tissue and arterial hematocrit yielded an overestimation of PET-derived F_b at rest and better agreement with the respective stress results. Figures 6.3(a/b) also contain correlation regressions for using the state-specific hct_t estimates calculated before, i.e. $hct_t = 0.26$ at rest and $hct_t = 0.37$ at stress. The Bland-Altman analysis in Figure 6.3(c) visualizes the lower PET resting F_b results for the case of $hct_t = hct_a$. Independent of hematocrit, it also shows a smaller absolute variability and a similar relative variability between PET and MRI flow estimates at rest and stress.

Concerning perfusion ratios, Figure 6.4(a) shows the ratio of stress and rest upslopes, exhibiting a sublinear and narrowly significant ($p < 0.02$) relationship to PET. Figs. 6.4(b) and 6.4(c) show the corresponding comparison for absolute blood flows from the constrained Fermi analysis as a representative example. MRI-derived perfusion ratios from flows F_b converted assuming $hct_t = hct_a$ at both rest and stress (Fig. 6.4(b)) yielded a sublinear but highly significant ($p = 0.002$) relationship to PET. Using the previously calculated, state-specific hct_t estimates for conversion of F_p to F_b, an almost linear relationship between MPRs from PET and DCE-MRI was recovered (Fig. 6.4(c)).

Plots showing the corresponding results for using the low-resolution AIF are given in Appendix B (Fig. B.1). Flow results were on average similar, but especially at stress more variable than results with the high-resolution AIF. In cases with large differences to PET results, unstable and high baseline signals were often observed with the low-resolution AIF at stress, i.e. the native state without prior contrast injection.

6.3.3 Regional

Figure 6.5 shows correlation plots comparing absolute sector-wise flow results of PET with constrained (a) and unconstrained (b) Fermi deconvolution as well as with SVD (c) in a pooled fashion. Conversion of F_p to F_b for DCE-MRI flows was executed using state-specific hct_t conversion factors as calculated before. SVD exhibited the lowest overall variability when compared to PET ($R^2 = 0.72$) and a slightly sublinear regression due to higher resting flows. Constrained Fermi analysis yielded a similarly good agreement with PET ($R^2 = 0.70$) whereas unconstrained Fermi analysis resulted in a number of high-flow outliers ($R^2 = 0.59$). The underlying difference in constrained and unconstrained Fermi

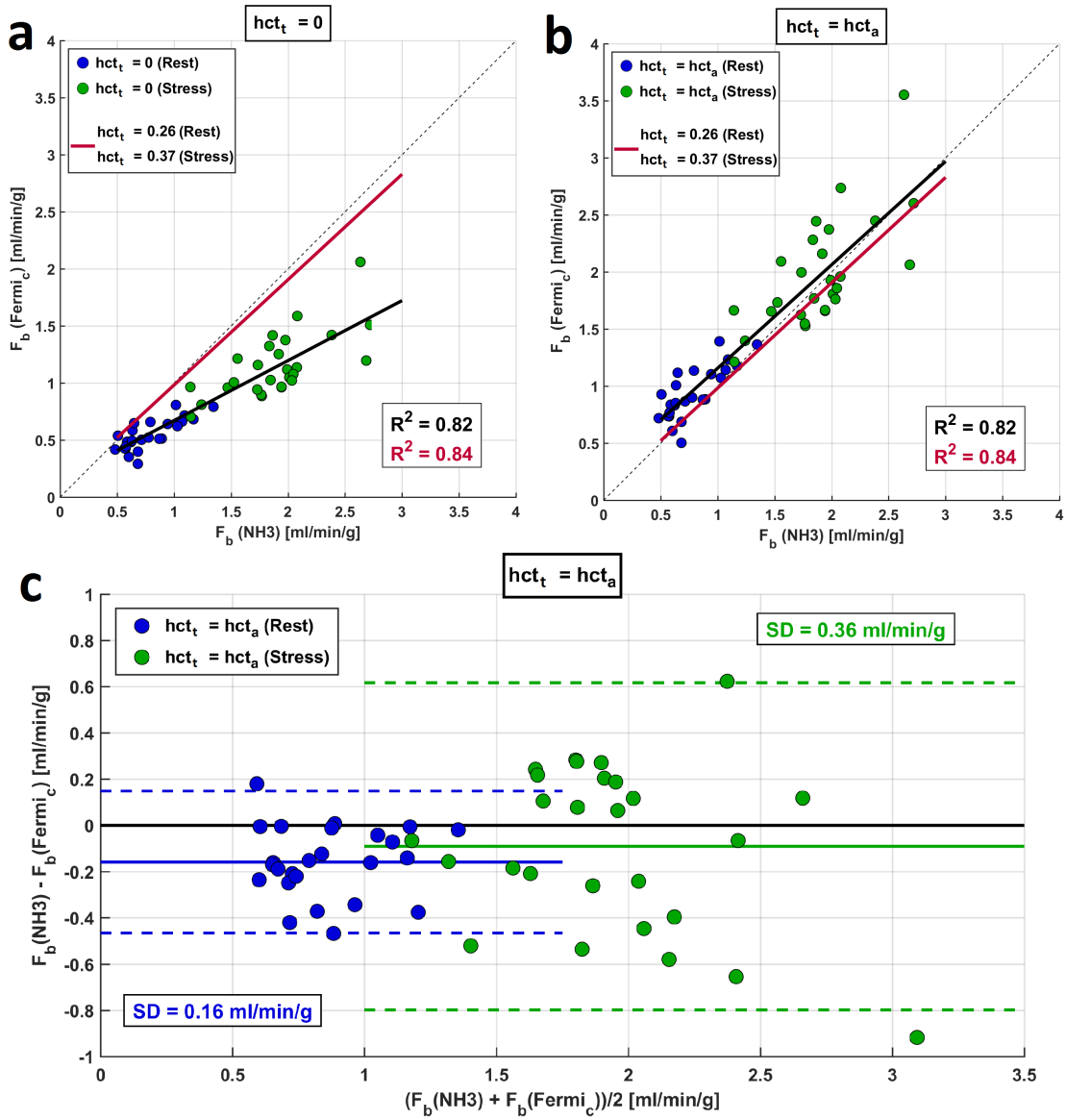

Figure 6.3: Slice-average comparison of $^{13}NH_3$ PET and constrained Fermi analysis. All rest (blue) and stress (green) slice-average results from the constrained Fermi analysis are shown assuming either $hct_t = 0$ (**a**) or $hct_t = hct_a$ (**b**) for conversion of F_p to F_b. (**c**) Bland-Altman plot for the case of $hct_t = hct_a$ shows the higher MRI resting flows compared to PET despite low variability. For state-specific adjustment of hct_t calculated from PET and MRI flow results only the regression line is shown in red (**a**/**b**).

response curves is visualized for one example sector in Figure 6.5(d). There, the initial plateau of the response curve for the unconstrained Fermi fit was usually shifted far into negative time, implying that the highest relative rate of indicator transit be at $t = 0$. This led to strong increases of flow estimates over Fermi analysis constrained to assume

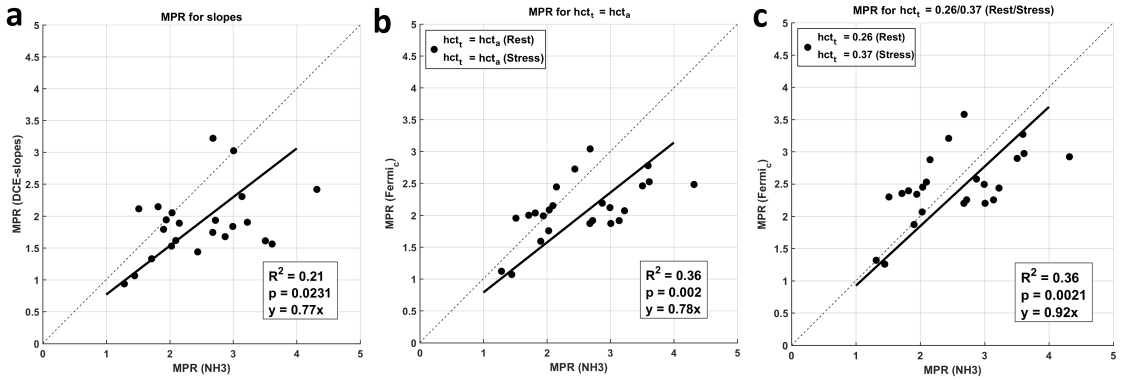

Figure 6.4: Comparison of myocardial perfusion reserve estimates between PET and DCE-MRI. A weak correlation with PET was observed for the slope analysis (**a**). Absolute quantification yielded higher correlation factors (**b**) despite showing a sublinear relationship under the global assumption of $\mathrm{hct_t} = \mathrm{hct_a}$. A regression slope closer to unity was recovered using state-specific $\mathrm{hct_t}$ estimates (**c**).

no indicator transit at $t = 0$. These differences in flow estimates were usually observed without differences between the corresponding fits to the tissue curve.

6.3.4 Example Cases

The two cases displayed in Figs. 6.6 and 6.7 provide examples for combining PET and MRI perfusion data in the context of a simultaneous acquisition. Patient A exhibited a subtle inferior perfusion defect 6 months after myocardial infarction following occlusion of the proximal RCA, but without a high-grade stenosis at the time of the scan. While PET data would have suggested a stenosis-related inducible defect, simultaneously acquired DCE-MRI curves revealed an increase in extracellular volume already at rest. This was consistent with Late Gadolinium Enhancement, pointing towards a perfusion difference due to post infarction fibrosis. Patient B was clinically classified as a case of apparent left ventricular cavity dilatation (LVCD) on the basis of $^{13}NH_3$ perfusion data, however lacking a morphological reference for the dilatation. Simultaneously acquired MRI data revealed both ventricular hypertrophy and an endo- to epicardial perfusion gradient at stress matching the pattern of apparent dilatation .

6.4 Discussion

Cohort-Average Flows and MPR. This study has compared quantitative estimates of myocardial perfusion flow between simultaneously acquired $^{13}NH_3$-ammonia PET and DCE-MRI data in a clinically relevant patient cohort. An overall good agreement between the two methods with respect to absolute flow results is contrasted with a trend of DCE-MRI underestimating PET perfusion ratios irrespective of the MRI deconvolution method. The observed underestimation of MPRs was equivalent to an overestimation of absolute

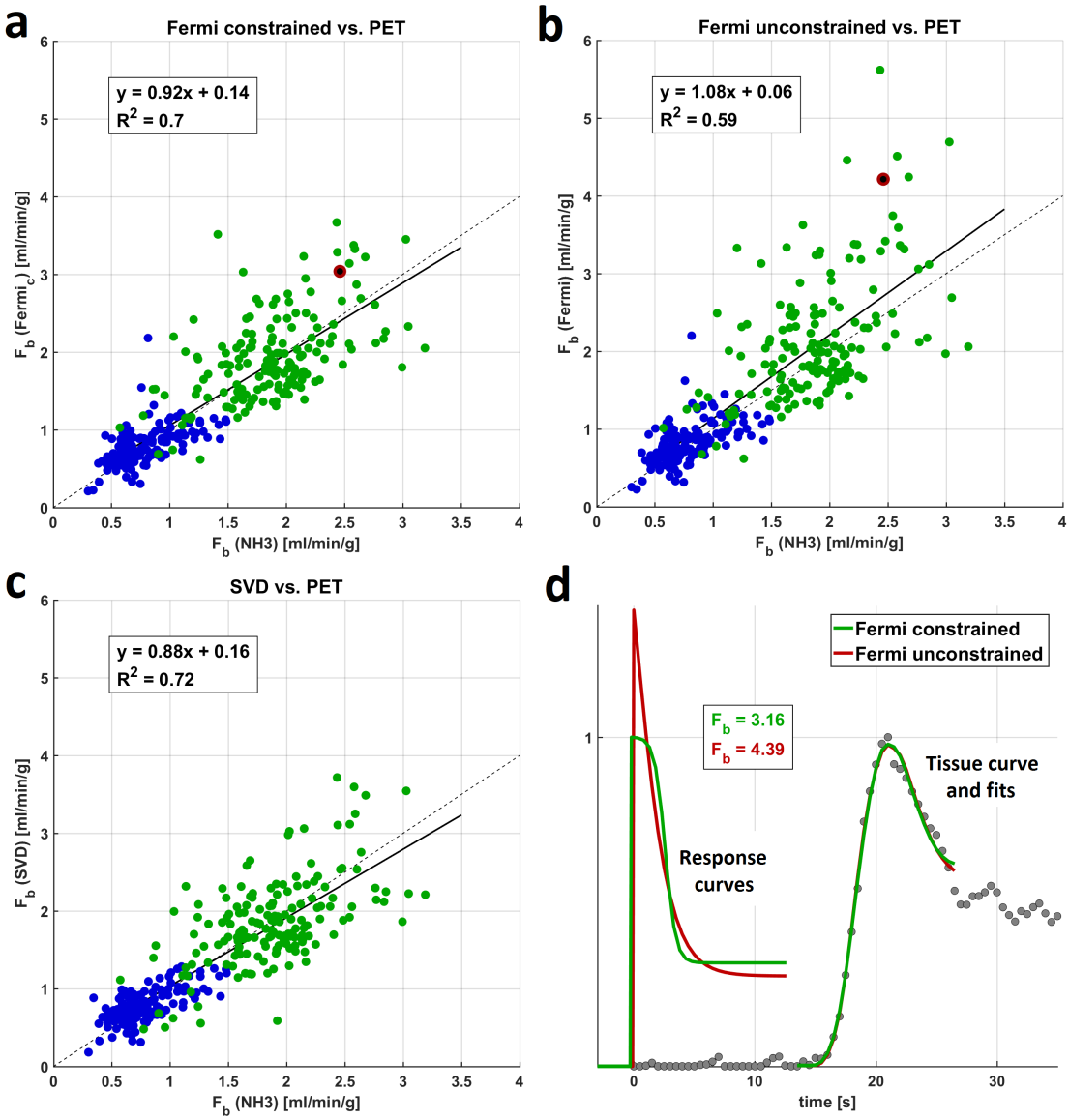

Figure 6.5: Comparison of absolute regional flow estimates between PET and DCE-MRI. Regional flow is compared between PET and constrained (**a**) and unconstrained (**b**) Fermi deconvolution as well as SVD (**c**). (**d**) Response functions and fits for both Fermi implementations in one example sector whose position is highlighted in the correlations (**a**/**b**). Note the difference in flow estimates and response curve appearances despite indistinguishable fit results between unconstrained and constrained Fermi models.

PET flows at rest when calculating blood flow from DCE-MRI data under the most common assumption of equal tissue and arterial hematocrit. Despite there being no other studies to date with both comparable methodology and patient cohort, and none with a simultaneous acquisition approach as described herein, most earlier studies have shown

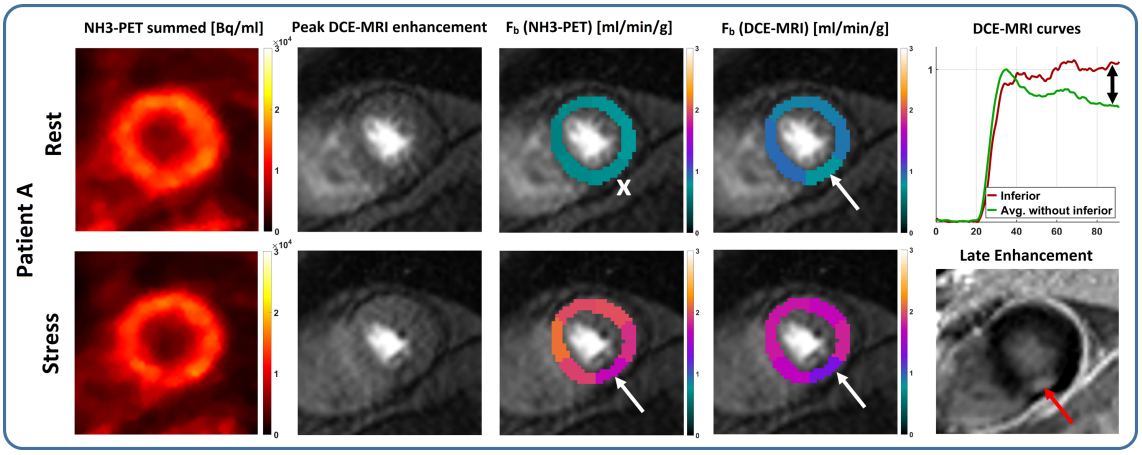

Figure 6.6: Clinical example case for integration of PET, DCE and LGE data for a patient 6 months after myocardial infarction following an occlusion of the proximal RCA. The highlighted inferior perfusion defect appeared as stress-inducible in PET, which would have led to a misclassification of the deficit as being indicative of a high-grade RCA stenosis. While invasive coronary angiography did not reveal a potential culprit stenosis, both the resting state DCE-MRI exam as well as LGE revealed an increased extracellular volume consistent with fibrotic tissue alterations.

similar patterns of DCE-MRI underestimating PET flows in some form. Pack et al. [110] have found an overestimation of resting flows and concordance of stress flows using comparable modeling approaches for both PET and MRI, examining healthy volunteers. More recently, Miller et al. [98] and Qayyum et al. [116] showed a similar pattern of underestimation for the relationship of PET and DCE-MRI flow results at rest and stress using ^{82}Rb-PET and SVD analysis in patients with CAD. The largest clinically-oriented study to date by Morton et al. [102] has reported good agreement in MPR despite a large variability in absolute flows, using however a simplistic single-compartment model for $^{13}NH_3$ data modeling.

6.4.1 Tissue Hematocrit Adjustment

Akin to the studies cited above, the majority of publications reporting DCE-MRI-derived values of myocardial blood flow do not make explicit references to hematocrit normalization. Neglecting the use of correct reference volumes during DCE-MRI analysis does not necessarily lead to errors with respect to flow quantification, it is however equivalent to assuming equal tissue- and arterial hematocrit [134]. It also obscures the fact that blood flow and plasma flow are two different quantities whose relationship may be complex especially in the capillary space [115]. Even if the difference between F_p and F_b is assumed to be given solely by a shift in reference volume as Eq. 6.1 suggests: The deduction of tissue hematocrit for the very particular case of an image voxel - containing all parts of the subarterial vascular tree with different hematocrit levels in different volumetric proportions – is not easily made from basic physiology. In the few studies that explicitly reference

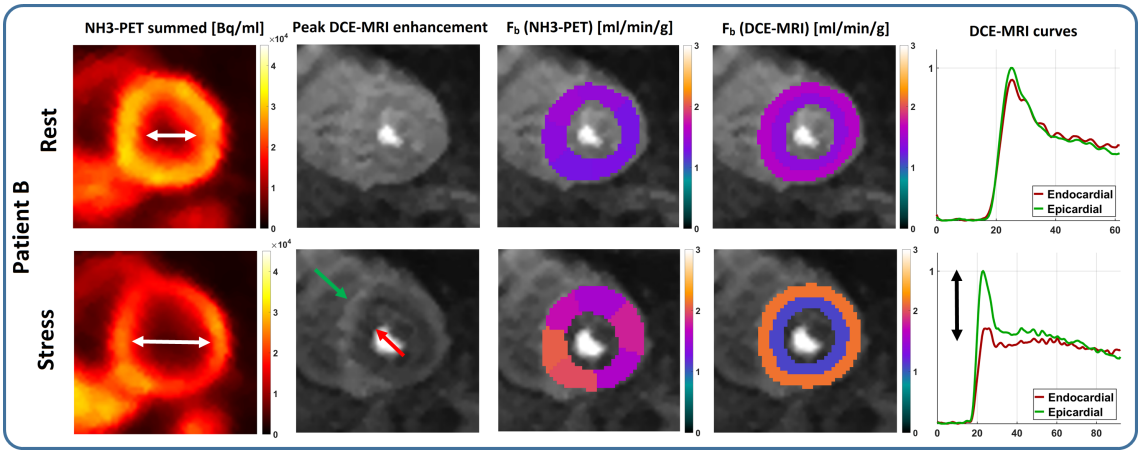

Figure 6.7: Clinical example case for combination of PET and DCE-MRI in a patient with stable angina, significant left-ventricular hypertrophy, but without any high-grade stenosis in either RCA or LAD at the time of the scan. PET data suggested classification as a case of apparent left-ventricular cavity dilatation (LVCD), however lacking a true morphologic reference with respect to the dilatation. The latter is provided from simultaneously acquired MRI data, where DCE-MRI revealed strong endo- to epicardial perfusion gradients at stress concordant with microvascular disease and disproving an actual cavity dilatation.

this issue, assumptions for $\mathrm{hct_t}$ range from 25% [13] to 100% [16] of arterial hematocrit, while for the vast majority of studies the latter case is inadvertently assumed. With respect to the difference between blood and plasma flow, this manuscript has proposed a combination of simultaneously acquired MRI and PET perfusion data to yield estimates of tissue-to-arterial hematocrit fractions. Under the explorative assumption that there be no systematic differences between PET and MRI flow estimates other than vascular tracer/indicator distribution volume, estimates of $d_{hct} = 63\%$ ($\mathrm{hct_t} = 0.26$) at rest and $d_{hct} = 89\%$ ($\mathrm{hct_t} = 0.37$) at stress were obtained. An increase in $\mathrm{hct_t}$ between rest and stress is at least in part plausible, considering the documented increase of microvascular hematocrit between rest and vasodilator stress [81]. In addition, already an increasing relative volume fraction of coronary arterioles during adenosine vasodilatation may appear as an effective increase of $\mathrm{hct_t}$ within DCE-MRI voxels covering myocardial tissue.

6.4.2 Water Exchange Effects

It is important to emphasize at this point that tissue hematocrit adjustment on one hand, and MRI water exchange effects on the other hand, are two separate issues: Hematocrit adjustment according to Eq. 6.1 simply extends the reference volume of flow (or "dynamic" volume in the indicator-dilution sense [151]) from plasma to blood, irrespective of how indicator concentrations were initially calculated from MR image signal. The water exchange condition only influences the latter, i.e. it determines how relaxation rates from different tissue regions constitute the overall MRI voxel signal. The extreme cases are represented by a single mono-exponential relaxation rate (fast exchange limit) or by individual

relaxation rates for each compartment resulting in multi-exponential behavior (limited/no exchange) [40]. Violations of the commonly (as well as herein) assumed fast exchange limit between vascular/extravascular or interstitial/cellular spaces would globally lead to a decrease in tissue signal and therefore a decrease in DCE-MRI flow estimates [40,70,88]. The degree to which water exchange has an impact on DCE-MRI signal during the first pass depends in large part on the respective sequence parameters, and sequences with short repetition times/high flip angles as used herein are known to be less sensitive to exchange effects [18,40,88]. However, first-pass extraction fractions observed in this study were significantly lower at stress than at rest, leading to a larger effective difference between vascular and extravascular relaxation rates during the first pass, and therefore a potentially different impact of exchange effects [70] at the two states. It is therefore conceivable that some part of the observed difference in PET and DCE-MRI flow estimates between rest and stress, which in this study has been projected onto a state-dependent tissue hematocrit, is also due to a difference in exchange conditions.

6.4.3 AIF and Signal Normalization

Considering alternative explanations for systematic biases between MRI and PET, the nonlinearity between image signal and contrast agent (signal saturation) on the DCE-MRI side can probably be considered more as a source of variability since it relies on baseline MRI signal and corresponding MOLLI T1 estimates. In this study, saturation correction was executed using a single normalization constant for both rest and stress scans, deliberately avoiding differences in reliability between DCE-MRI baseline signals at rest and stress, e.g. due to imperfect saturation efficiency [17]. Also, the overall similar results obtained using the low-resolution AIF with a different signal normalization approach do not suggest this as a source for systematic error. The larger variability observed with the dual-sequence approach has reproduced findings of recent studies investigating the influence of ROI placement [66] and unreliable (native) baseline signals in the context of potentially imperfect saturation [17]. Both of these problems are closely related to the originally proposed [46] centric k-space acquisition used herein, which has been avoided in more recent implementations [73]. Results from this study therefore do not imply a general inferiority of dual-sequence approaches, but only provide further evidence for the inaptitude of centric k-space acquisition strategies in this context. Concerning plausibility of DCE-MRI results, also the additional microvascular parameters – being a product of the same deconvolution process as the flow estimates – have reproduced results from comparable studies with respect to absolute values and changes in parameters such as first-pass extraction and vascular volume in response to adenosine stress [16,73,88].

6.4.4 Data Structure and Temporal Resolution

Apart from indicator/tracer biodistribution, other systematic differences between dynamic PET and MRI data structure potentially play a role concerning flow estimation: Dynamic PET is represented by images showing an integration over all tracer radioactivity extracted from the vascular space across retrospectively defined time windows $\geq 10\,\mathrm{s}$. In DCE-MRI, the distribution of indicator is assessed from ECG-gated images representing the current

state of vascular and extravascular indicator accumulation in the tissue as a snapshot. Unlike PET, where flow is estimated from tracer extraction, established DCE-MRI approaches estimate perfusion flow via indicator convection using the initial amplitude of a response function resulting from a discrete deconvolution of tissue curve and AIF. From a mathematical perspective, this deconvolution result is not unique for transit times smaller than the temporal resolution of the scan (e.g. 1/heart rate). As it is not clear whether such small transit times at all exist, e.g. in the form of shunt channels, this does not necessarily pose a general limitation to DCE-MRI flow estimation. It does however suggest a more careful examination of the stability of flow results as exemplified by the discrepancy between the constrained and unconstrained Fermi analysis reported herein. Figure 6.6(b/c) shows that, especially at high flows, unconstrained Fermi response curves were observed proposing large rates of indicator transit during the first second(s), leading to significantly higher flow estimates that were contradicted by the corresponding PET results. The fact that DCE-MRI data effectively do not contain information on this part of the response curve is reflected in the virtually indistinguishable fit results produced by these strongly differing assumptions about tissue perfusion (Fig. 6.6(d)). Despite the conceivability of very fast (shunt) channels that may also lead to systematic differences between PET and MRI perfusion flows, estimating their weight from standard DCE-MRI data is not possible, and proper modeling constraints are advised for stability. Note that this does not only apply to the Fermi model, but also to more complex two-region models, for which careful examination of fit results with respect to very small vascular transit times has already been suggested by Broadbent et al. [16] as well as in Chapter 3 of this thesis.

6.4.5 Limitations

With respect to PET, it is known that the relationship between $^{13}NH_3$-ammonia extraction rate and blood flow depends to some degree on the latter, although it can usually be assumed as linear for the limited flow range that is seen clinically ($\leq 3\,\mathrm{mL/min/g}$) [104,106]. With respect to DCE-MRI, the impact of T_2^* effects on AIF at peak signal enhancement was not explicitly modeled during correction for signal saturation [47]. The effect was however too small to introduce a significant bias between low- and high-resolution AIF flow results despite a difference in echo time between both acquisition schemes. Therefore, effects of T_2^* relaxation were smaller than effects of the aforementioned variability in low-resolution AIF baseline signals or factors such as ROI placement. Additionally, the assumption of nominal flip angles during signal-to-concentration modeling for high-resolution AIFs and tissue curves represents an oversimplification of reality, as the non-uniformity of slice excitation profiles leads to an accumulation of spatial variations in actual flip angle distributions during k-space acquisition [140,145]. This may have caused some additional bias when comparing perfusion results to PET, especially in the context of combining high-resolution tissue curves (linear k-space ordering) with dual-sequence AIFs (centric k-space ordering), because signal-to-concentration modeling for the latter does not rely on the inclusion of excitations after the first k-space line [11]. Note however that inaccuracies with respect to flip angles would affect rest and stress perfusion quantification in a similar fashion, and therefore most likely not pose a significant limitation with respect to the reported differences in MPR between MRI and PET.

With respect to arterial hematocrit, individual measurements were not available from the day of the exam. However, the reported relative d_{hct} fractions are essentially insensitive to absolute arterial hematocrit, and the use of an established, global assumption may be seen as increasing the comparability of absolute results to earlier studies, where individual hematocrit sampling has rarely been reported.

6.4.6 Conclusion

Using simultaneously acquired PET/MRI data, an overall good agreement of absolute myocardial perfusion flow estimates from both modalities was observed in a clinically relevant patient cohort. However, significant differences in stress/rest perfusion ratios concordant with previous investigations suggest that absolute thresholds for ischemia classification may not be directly tradable between PET and MRI. The combination of clinical data from both modalities has demonstrated the unique potential of integrated PET/MRI, both for individual patient cases as well as on a cohort-wide basis with respect to tissue hematocrit . Additionally, a physiologically motivated constraint to the widely-used Fermi deconvolution method has been introduced and validated against PET for regional perfusion quantification.

Chapter 7

Quantitative Extracellular Volume, Native T_1 and ^{18}F-FDG PET/MR Imaging in Patients after Revascularized Myocardial Infarction

Based on the work pubished in:
KP Kunze et al., Journal of Cardiovascular Magnetic Resonance 20:33, 2018.

7.1 Motivation

The development of quantitative cardiovascular magnetic resonance imaging techniques as a means for myocardial tissue characterization has seen a number of advances in recent years. Due to their relative robustness [71], especially extracellular volume mapping and contrast media free native T_1 (nT_1) mapping are being translated into clinical applications [100,148] and both have shown promising results with respect to infiltrative and fibrotic cardiac diseases [52,74,125]. For acute myocardial infarction, equivalence or superiority of quantitative mapping approaches over qualitative techniques with respect to the delineation of the Area At Risk (AAR) [20,143] and the prediction of functional outcome have been shown for native T_1 [34,42] and ECV [77] mapping. While there is ongoing discussion about the limits of detection for absolute changes of ECV in more subtle disease processes [24,141], studies involving ECV and T_1 mapping often make only limited use of absolute values. Both mapping techniques have usually been evaluated as more sensitive or accurate versions of late gadolinium enhancement or T_2-weighted imaging for the determination of infarct size or AAR in the context of AMI [20,42,77,96,143]. This however neglects part of the quantitative potential of ECV and T_1 mapping, which for the first time allow non-invasive MR imaging of the local severity of myocardial injury and edematous processes as opposed to only measuring their extent.

The assessment of post-AMI inflammatory processes have recently also come into the focus of PET imaging, where ^{18}F-FDG is used in combination with metabolic preparation to target cardiac infiltration by inflammatory cells [119,149]. However, there is still uncertainty with respect to the contribution of infiltrative inflammatory cells and altered

metabolism by post-ischemic but viable cardiomyocytes to the ^{18}F-FDG imaging signal when applied in a clinical setting [119]. In this context, simultaneous PET/MR imaging offers the potential for a deeper understanding of quantitative methods from both modalities and their relation to physiology [121,131].

The study at hand employs PET/MR imaging to quantitatively investigate the relationship of the three imaging markers ^{18}F-FDG uptake, native T_1 and ECV in the context of a complex tissue state consisting of diverse processes including inflammation, edema and cellular tissue damage after revascularized AMI. In addition, blood markers of myocardial damage and blood counts of inflammatory cells have been obtained following the acute event. Consequently, quantitative regional results from the three imaging methods under investigation are compared among themselves as well as with peripheral blood parameters. It is investigated to what degree the three imaging methods indicate independent features of the post-ischemic healing process, and to what degree these features are co-localized. Proceeding in this fashion, it is the goal of this manuscript to highlight the potential in making full use of available quantitative information from cardiac multimodality imaging for a better understanding of image signals and their relation to pathophysiology.

As an extension to the originally published manuscript, an additional, explorative analysis combining imaging results from MRI and PET is presented on the basis of the observed correlations of imaging and blood markers. It aims at an estimation of cohort-average weights for different signal contributions to the ^{18}F-FDG signal by using a linear model, constructing measured ^{18}F-FDG uptake values from myocytic (100 - ECV) and inflammatory (nT_1) pathways.

7.2 Methods

7.2.1 Patient Cohort

Patients that were retrospectively enrolled for this investigation ($n = 25$) represent a large subgroup of a cohort from a previously published study [119], which has focused on global measures of ^{18}F-FDG uptake and LGE and their relationship to functional outcome. All patients underwent examination on a clinical 3T PET/MRI scanner (Biograph mMR, Siemens Healthcare GmbH, Erlangen, Germany) 5 ± 1 days after myocardial infarction and subsequent, successful revascularization (TIMI grade ≥ 2, average: 2.9). The study was approved by the local ethics committee, performed in agreement with the Declaration of Helsinki, and all participants gave written and informed consent. Criteria for retrospective enrollment were membership in the final study cohort reported in [119] and availability of native and post contrast T_1 data. Additionally, patients showing signs of microvascular obstruction (MVO) in LGE images were excluded from quantitative analysis, as the necessary contrast agent equilibration for ECV mapping is not attainable. Also, segmentation of MVO border zones was deemed not practicable in these cases due to the differences in spatial resolution between PET and MRI images, and quantitative values would not have been comparable to results from transmural segmentation. A detailed description of the criteria for retrospective enrollment similar to the corresponding statements in [119] is given in Table 7.1.

7.2.2 PET Imaging

^{18}F-FDG PET was performed with patients receiving a low-carbohydrate diet the day before imaging, followed by a 12-hour fasting period in order to suppress physiological myocardial FDG uptake.

30 minutes before ^{18}F-FDG injection, patients received unfractionated Heparin (50 UI/kg body weight intravenously) to further suppress physiological myocardial FDG uptake [119]. A list-mode PET scan in 3D mode was started 144 ± 39 minutes after intravenous injection of 311 ± 72 MBq of ^{18}F-FDG. Correction of emission data was performed for randoms, scatter, dead time and attenuation. Attenuation correction was accomplished using 2-point Dixon MRI sequence as previously described [91]. Parts of the body truncated in the attenuation map due to the limited MRI field-of-view were recovered from PET emission data using the maximum likelihood reconstruction of attenuation and activity (MLAA) technique [108]. For reconstruction, a 3D attenuation-weighted ordered-subsets expectation maximization iterative reconstruction algorithm (AW-OSEM 3D) was used with three iterations and 21 subsets, Gaussian smoothing at 4 mm FWHM, matrix size 344 x 344, zoom 1 and a resulting spatial resolution of 5 mm. For quantitative analysis, ^{18}F-FDG image signals were expressed as standardized uptake values based on lean body mass (SUV LBM) or - for comparison to blood markers - also as tissue-to-background ratios (TBR) normalized to blood signal taken from an LV-centric region of interest.

Table 7.1: Criteria for Retrospective Enrollment

	n
Original cohort in [119]	49
Received ^{18}F-FDG imaging and T_1 mapping	45
Exclusion due to	**n/45**
Unsuccessful suppression of physiological ^{18}F-FDG uptake	3
Previous infarctions revealed during imaging	2
Para-venous ^{18}F-FDG injection	1
Acute pneumonia	1
Non-diagnostic T_1 data	2
MVO at infarct core	11
Restrospectively enrolled	25

7.2.3 MR Imaging

As part of a comprehensive resting-state MRI exam, native and post-contrast T_1 maps were acquired using a MOLLI prototype sequence in three short axis slices per patient. Acquisition (3(3)3(3)6)-scheme [95]), retrospective motion correction and registration of native and post-contrast MOLLI data was performed as described in Section 3.2.5 of this thesis. If necessary, additional manual motion correction was applied to the T_1 image series as it was acquired in shallow breathing. After registration, ECV maps were calculated from the resulting T_1 maps using individually measured hematocrit. LGE images covering the

complete LV myocardium were acquired directly adjacent to post contrast T_1 maps after a cumulative dose of 0.2 mmol/kg Gd-DTPA (Magnevist, Bayer Healthcare, Leverkusen, Germany).

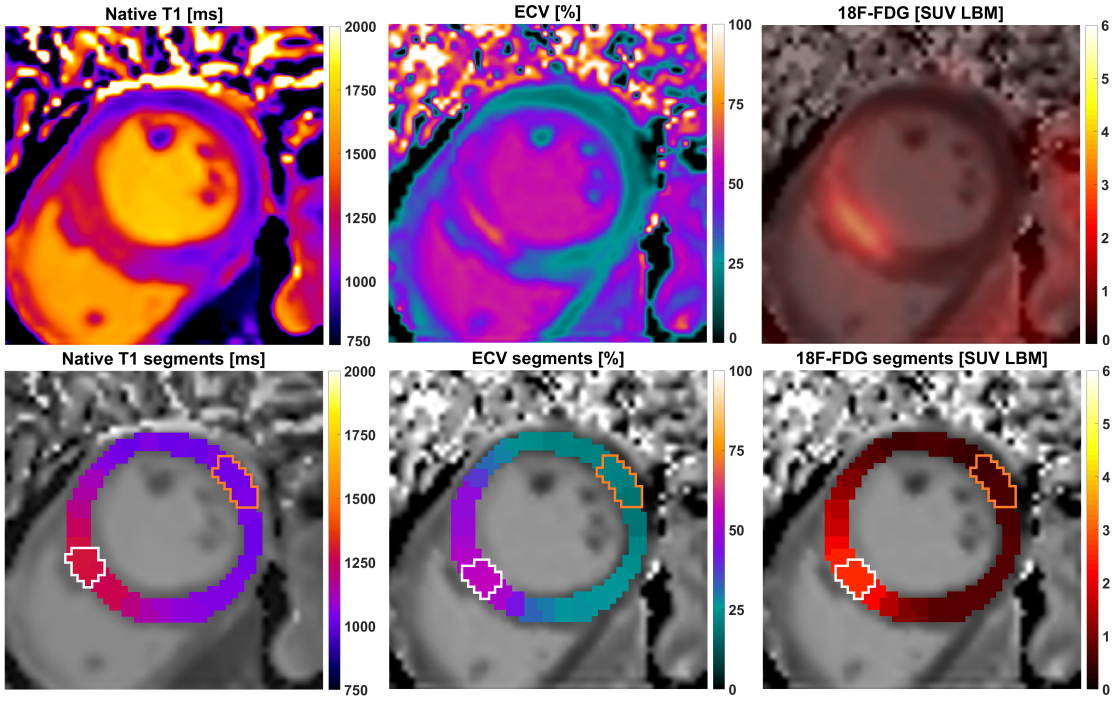

Figure 7.1: Visualization of the three analyzed image signals and their segmentation for one example case. The upper panel shows from left to right: native T_1, extracellular volume and ^{18}F-FDG uptake after fusion with the corresponding ECV map. The lower panel shows the respective segmentation results, consisting of 32 segments per slice that are co-localized between the three imaging methods. For each of these, white lines enclose the two sectors with the highest signal and orange lines the sectors defined as remote.

7.2.4 PET/MRI Image Analysis

For PET/MR image registration, the MunichHeart software [97] was used to fuse ^{18}F-FDG PET images with ECV and native T_1 maps. Manual alignment was performed between ungated PET data and individually motion-corrected MRI data if necessary. Manual segmentation on the basis of ECV maps was performed for the most infarct-centric of the three acquired slices, which was determined on the basis of LGE images covering the whole left ventricle. Basal and mid-ventricular slices were segmented into 32 sectors (16 for apical slices), equally spaced along a centerline between endo and-epicardial borders without additional morphological reference. This segmentation was applied to the registered ECV, nT_1 and ^{18}F-FDG PET images of that slice. For each patient, segmentation of the chosen slice therefore resulted in 32 transmural sector values (16 for apical slices) for each of the three image signals under investigation as shown in Fig. 7.1. An average of the two

highest sector values was taken as representing maximum insult severity for each patient and each image signal in the sense of an "imaging biopsy". These maximum values were determined independently for each imaging method, and therefore do not necessarily refer to the exact same intra-slice location (see Fig. 7.1). For the quantitative analysis of remote regions, three sectors as distal as possible to the sector with the highest value were chosen manually. Therefore, for each patient, the remote value of ECV, nT_1 and ^{18}F-FDG uptake respectively refers to the average from the so-defined remote sectors, and the maximum value refers to the average of the two highest sector values. Additional measures of infarct size in % of LV volume were obtained by manual delineation of enhancement regions in the LGE images as described previously [119].

7.2.5 Blood Analysis

Daily blood sampling was performed for up to 6 days after revascularization. Peak levels of blood parameters creatine kinase (CK), creatine kinase-MB (CK-MB), troponin T as well as peak leukocyte and monocyte counts were taken from this sampling period as previously reported [119].

7.2.6 Data Analysis and Statistics

Data processing and statistical analysis were executed in Matlab R2017a (Mathworks, Natick (MA), USA). Between-subject correlations represent a correlation of per-subject means, within-subject correlations were calculated using multiple regression (analysis of covariance). R- and p-values are given as Pearson correlations coefficients with a 5% significance level.

Fit procedures employed an unconstrained linear model, both an R-squared goodness-of-fit value (adjusted for the number of predictors) and 95% confidence intervals for resulting parameters are reported.

Table 7.2: Patient Characteristics

Characteristics	
Final [n] (%)	25 (100)
Male [n] (%)	22 (88)
Age [y]	66 ± 10
Pain to PCI [h]	7.2 ± 7.1
PCI to scan [d]	4.9 ± 1.4
HR at scan [bpm]	62 ± 9
Infarct size (LGE) [% LV]	17.3 ± 7.1
Avg. blood markers	
CK max [U/l]	1806 ± 930
CK-MB max [U/l]	211 ± 124
Troponin T max [U/l]	2.5 ± 1.7
Peak Leukocytes [G/l]	12.8 ± 4.3
Peak Monocytes [G/l]	1.1 ± 0.4

7.3 Results

7.3.1 Patient Cohort

The physiological characteristics of the final patient cohort (n = 25) are shown in Table 7.2. A total of 42 individual segments from four patients were excluded before quantitative

analysis due to small susceptibility artifacts in the T_1 maps (n = 3) or breathing artifacts in the PET attenuation map (n = 1).

7.3.2 Mutual Comparison of ^{18}F-FDG, ECV and native T_1

The total number of sectors after exclusions was 662 for each imaging method, consisting of 32 (mid/basal) or 16 (apical) sectors per patient for each of the 25 subjects. The upper panel of Fig. 7.2 shows the comparisons of these sector values in a globally pooled fashion. All three comparisons (FDG/ECV, FDG/nT_1, ECV/nT_1) exhibited similarly significant correlations between subject means (R = 0.60, 0.43, 0.51). The lower panel of Fig. 7.2 shows the corresponding within-patient correlations, i.e. a linearization of within-slice signal increase for each patient (i.e. each slice) individually. Within-patient analysis yielded much higher correlation factors (R = 0.91, 0.87, 0.88) than the globally pooled comparison.

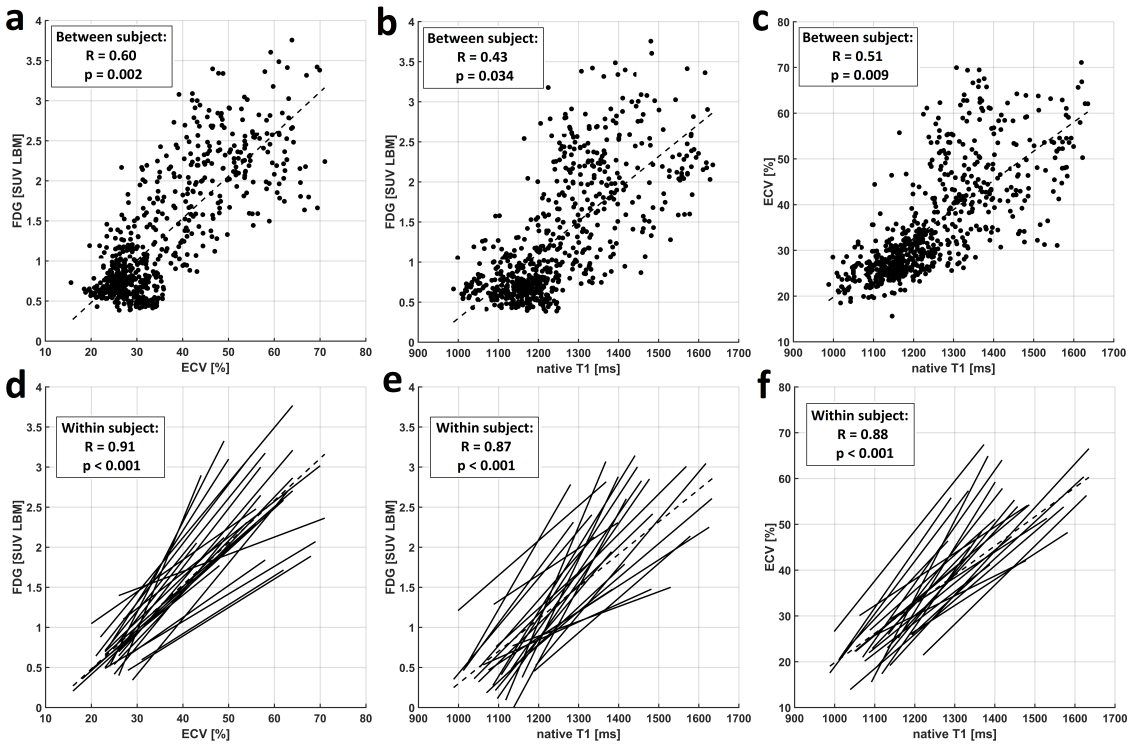

Figure 7.2: Pooled comparison (**a-c**) and individual regressions (**d-f**) between sector values from all three imaging methods. These are ^{18}F-FDG vs. ECV (**a**/**d**), ^{18}F-FDG vs. nT_1 (**b**/**e**) and ECV vs. nT_1 (**c**/**f**). Plots (**a-c**) each include results from all 662 sectors from all 25 patients and the correlation between subjects. Plots (**d-f**) visualize the different slopes of individual linear regressions and show the respective correlation factors within subjects.

The underlying inter-patient variability of absolute values at the high end was most clearly discernible for the comparison of FDG/ECV. Consequentially, if only the average

of the two maximum sector values from each patient were compared, no significant correlations were observed for FDG/ECV, FDG/nT_1 nor ECV/nT_1 (Fig. 7.3). Table 7.3 shows ranges and averages for maximum and remote values across all patients for each imaging method. While maximum values were determined individually for each imaging method, average distances between sectors containing these were small across modalities, i.e. on average 1.2 sectors between ECV/FDG, 2 sectors between nT_1/FDG and 1.9 sectors between nT_1/ECV.

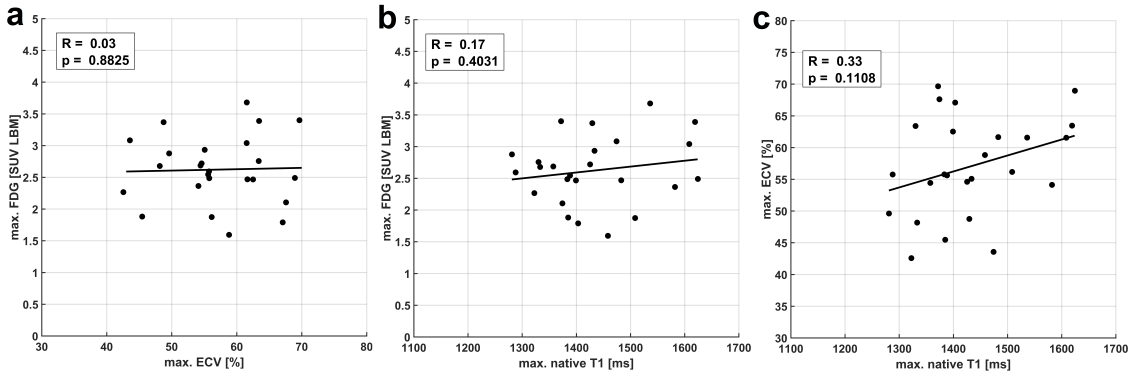

Figure 7.3: Comparison of maximum sector values between ECV/^{18}F-FDG (**a**), nT_1/^{18}F-FDG (**b**) and ECV/nT_1 (**c**) for all 25 patients, showing no significant correlations between the three methods. All points in plots (**a-c**) are equivalent to a per-patient average of the two highest sector values shown in the corresponding pooled comparisons in Fig. 7.2 (**a-c**)

7.3.3 Comparison of Maximum Image Signals and Infarct Size

Results for comparing infarct sizes with corresponding maximum values of ECV, ^{18}F-FDG uptake and native T_1 are shown in Fig. 7.4. Infarct sizes calculated on the basis of LGE images yielded an average infarct size of 17.3 ± 7.1% of LV volume. A highly significant correlation of cellular damage as indicated by maximum ECV with infarct size was observed ($p = 0.002$). Conversely, no significant correlation between infarct size and either maximum ^{18}F-FDG uptake or maximum native T_1 was observed.

Table 7.3: Maximum and Remote Values for ECV, native T_1 and ^{18}F-FDG

	Mean	**SD**	**Range**
Max. ECV [%]	57.0	7.8	42.6 - 70.0
Max. nT_1 [ms]	1432	101	1281 - 1624
Max. FDG [SUV LBM]	2.62	0.53	1.62 - 3.74
Rem. ECV [%]	27.8	3.9	20.3 - 34.7
Rem. nT_1 [ms]	1163	92	998 - 1419
Rem. FDG [SUV LBM]	0.71	0.22	0.45 - 1.22

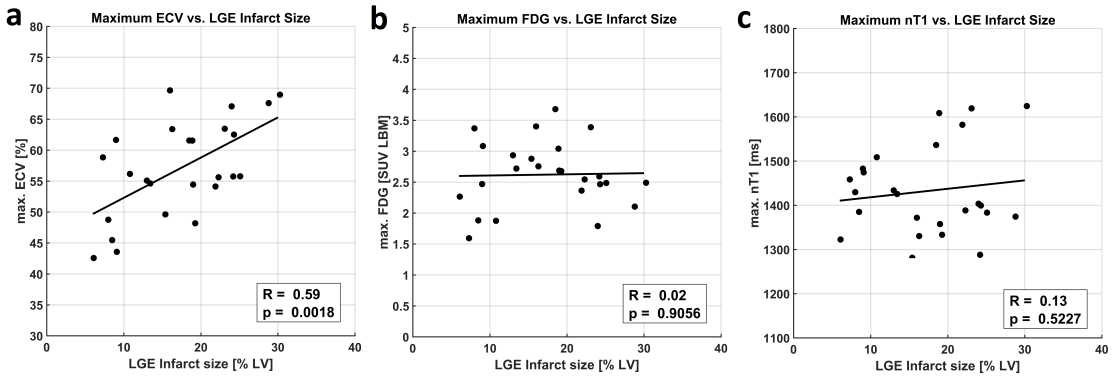

Figure 7.4: Comparison of maximum ECV, ^{18}F-FDG uptake and native T_1 values from the most infarct-centric slice with relative global infarct size as measured independently from LGE images in % LV. A good correlation between infarct extent and maximum tissue damage in terms of ECV was observed (**a**), while no correlation was seen between infarct size and maximum ^{18}F-FDG uptake (**b**) and native T_1 (**c**).

7.3.4 Comparison of Maximum Image Signals and Blood Markers

Maximum ECV (Fig. 7.5), ^{18}F-FDG uptake (absolute (Fig. 7.6) and TBR) and native T_1 (Fig. 7.7) were compared to peak values of peripheral blood parameters CK, CK-MB, troponin T as well as peak leukocyte and monocyte counts. Monocyte counts were unavailable for two patients, and were excluded for one additional patient due to splenectomy, resulting in 22 instead of 25 data points for Figs. 7.5(d)/7.6(d)/ 7.7(d). For maximum ECV, a strong trend towards association with peak CK ($p = 0.052$) and a significant correlation with peak CK-MB ($p = 0.0057$) were observed, despite no correlation to peak troponin or monocytes. The comparison to peak CK-MB revealed a tight relationship at the low end and a larger variability at the high end of values (Fig. 7.5(b)). For absolute ^{18}F-FDG uptake, only a narrowly significant correlation was found with troponin ($p = 0.042$), and none was found for ^{18}F-FDG TBR normalized to LV blood (see Appendix C). Maximum native T_1 values did not show significant correlations to CK or CK-MB, but a highly significant correlation ($p = 0.0046$) to peak monocyte counts and a significant correlation with troponin ($p = 0.024$). The corresponding comparisons to peak leukocyte counts are not shown, yielding a significant trend ($p = 0.033$) with native T_1.

7.3.5 Estimation of Contributions to ^{18}F-FDG Uptake Signal

In a final step, a cohort-average regression analysis using MRI results in conjunction with PET data was executed to yield an estimate of relative contributions to the ^{18}F-FDG signal. As a simplification, three contributing factors to the ^{18}F-FDG signal were assumed, namely: (migrated) inflammatory cell populations, post-ischemic cellular metabolism and a combination of blood pool and remaining metabolic background signal within the myocardium. Concerning their relationship to imaging results, the following three explorative hypotheses were made:

First, ^{18}F-FDG signals observed in this study contain a combination of blood pool and

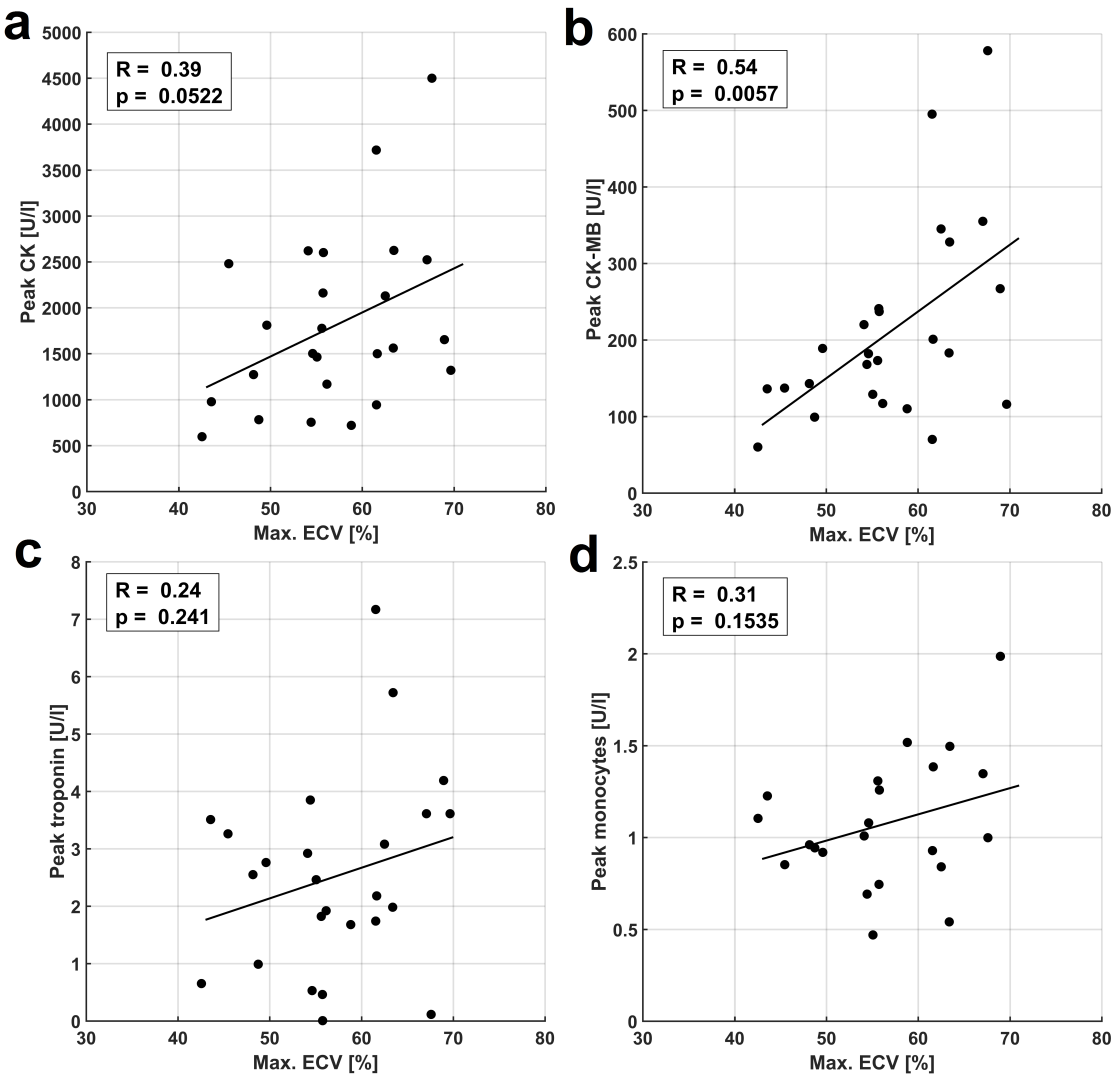

Figure 7.5: Comparison of maximum ECV with peak blood parameters CK (**a**), CK-MB fraction (**b**), troponin (**c**), and monocyte counts (**d**). A narrowly insignificant trend for CK ($p = 0.052$) and a highly significant correlation to CK-MB ($p = 0.0057$) were observed.

remaining metabolic contributions (FDG^{back}) that are spatially constant and equal to the signal from remote regions. Second, the post-ischemic metabolic signal fraction (FDG^{pIS}) at the site of infarction is – on a cohort-wide average – proportional to the (reduced) fraction of intact myocytes as indicated by ECV imaging. Third, the infiltrative/inflammatory cellular signal fraction (FDG^{Inf}) at the site of infarction is – on a cohort-wide average – proportional to the edematous response indicated by the relative increase of native T_1, considering the high correlation of maximum T_1 values to peripheral monocyte counts shown before.

Based on these assumptions, an alternative maximum ^{18}F-FDG signal (FDG_{constr}) was constructed from a linear combination of the three described contributing pathways:

$$FDG_{constr} = \lambda \cdot \Delta nT1_{FDG} + \mu \cdot (100 - ECV_{FDG}) + FDG_{remote},$$

$$\Delta nT1_{FDG} = nT1_{FDG} - nT1_{remote}.$$

Here, the scale for ECV was inverted so that the term 100 - ECV reflects the amount of remaining cellular volume, while λ and μ represent arbitrary proportionality coefficients.

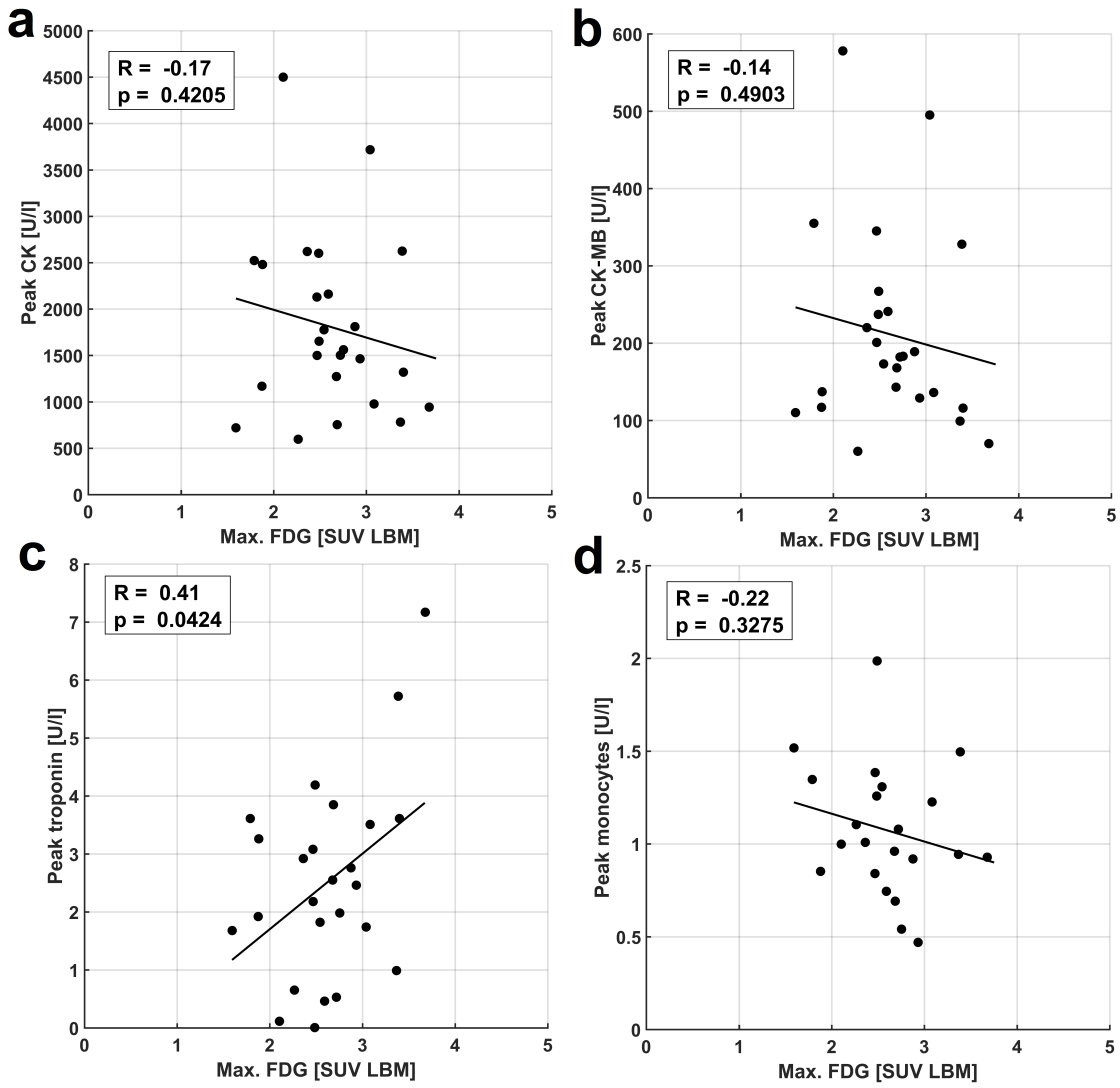

Figure 7.6: Comparison of maximum ^{18}F-FDG uptake with peak blood parameters CK (**a**), CK-MB fraction (**b**), troponin (**c**), and monocyte counts (**d**). A narrowly significant trend for troponin (p = 0.042) was observed.

Note that maximum values of ^{18}F-FDG uptake were determined as before (FDG_{max}), but corresponding T_1 and ECV values ($nT1_{FDG}/ECV_{FDG}$) were now taken from the exact same intra-slice location as the maximum FDG value. The above equation was solved for coefficients λ and μ by minimizing the difference between constructed (FDG_{constr}) and measured maximum (FDG_{max}) FDG uptake. This is equivalent to interpreting the vector of differences FDG_{max} – FDG_{remote} across all patients as a linear combination of the corresponding vectors of ΔnT_1 and (100 - ECV) values. Assuming only the three described contributions to the ^{18}F-FDG signal, averages for relative contributions are given by:

$$dFDG^{back} = \frac{\langle FDG_{remote} \rangle}{\langle FDG_{constr} \rangle}, \;\; dFDG^{Inf} = \frac{\lambda \langle \Delta nT1_{FDG} \rangle}{\langle FDG_{constr} \rangle}, \;\; dFDG^{pIS} = \frac{\mu \langle 100 - ECV_{FDG} \rangle}{\langle FDG_{constr} \rangle}$$

The average background contribution to the maximum ^{18}F-FDG uptake signal was 28% ± 8%. This was independent of the actual fit results as the mean of FDG_{constr} was essentially the same as the mean of the measured maximum ^{18}F-FDG uptake if evaluated across the whole cohort. Solving for λ and μ as described above led to similar estimates of mean contributions for $dFDG^{Inf}$ and $dFDG^{pIS}$ at about 38% and 34% respectively. Figure 7.8(a) shows the resulting patient-wise comparison between measured uptake signals and the ones constructed using the obtained parameters λ and μ. With a stronger divergence at the lower end of values, 95% confidence intervals for fit parameters λ and μ translated to large ranges for minimum - maximum contributions of 15% - 61% for $dFDG^{Inf}$ and 11% - 58% for $dFDG^{pIS}$ respectively. Fig. 7.8(b) shows the same fit applied separately to both high (green) and low ends (red) of measured ^{18}F-FDG uptake values as separated by the median. For the higher half, estimated average contributions for all pathways were similar to the fit of the whole cohort, but both adjusted R-squared (0.56) and 95% confidence intervals ((26 - 54)% for $dFDG^{Inf}$ and (21 - 50)% for $dFDG^{pIS}$) were much more indicative of an appropriate model. Exclusion of the outlier seen in Fig. 7.8(b) resulted in significantly tighter confidence intervals ((33 - 51)% for $dFDG^{Inf}$ and (25 - 43)% for $dFDG^{pIS}$) and a higher adjusted R-squared (0.77). Conversely, the fit to the lower half of values produced highly variable results with confidence bounds extending into an unphysiological (negative) range.

7.4 Discussion

The study at hand has compared absolute measures of ^{18}F-FDG uptake, extracellular volume and native T_1 in patients early after revascularized myocardial infarction using simultaneously acquired PET/MRI data. Quantitative results have been derived for a single, infarct-centric slice position that was co-localized between all three methods, which can be seen as a biopsy-like imaging approach. An effort was made to link the so-obtained image signals to underlying pathophysiological processes using independent measures of infarct size and peripheral blood markers of cardiac damage and inflammatory cell populations. The study did not investigate correlations between image signals and functional recovery post AMI as these have already been given separately for ECV [77], ^{18}F-FDG [119] and native T_1 [34] in quantitative or semi-quantitative fashion.

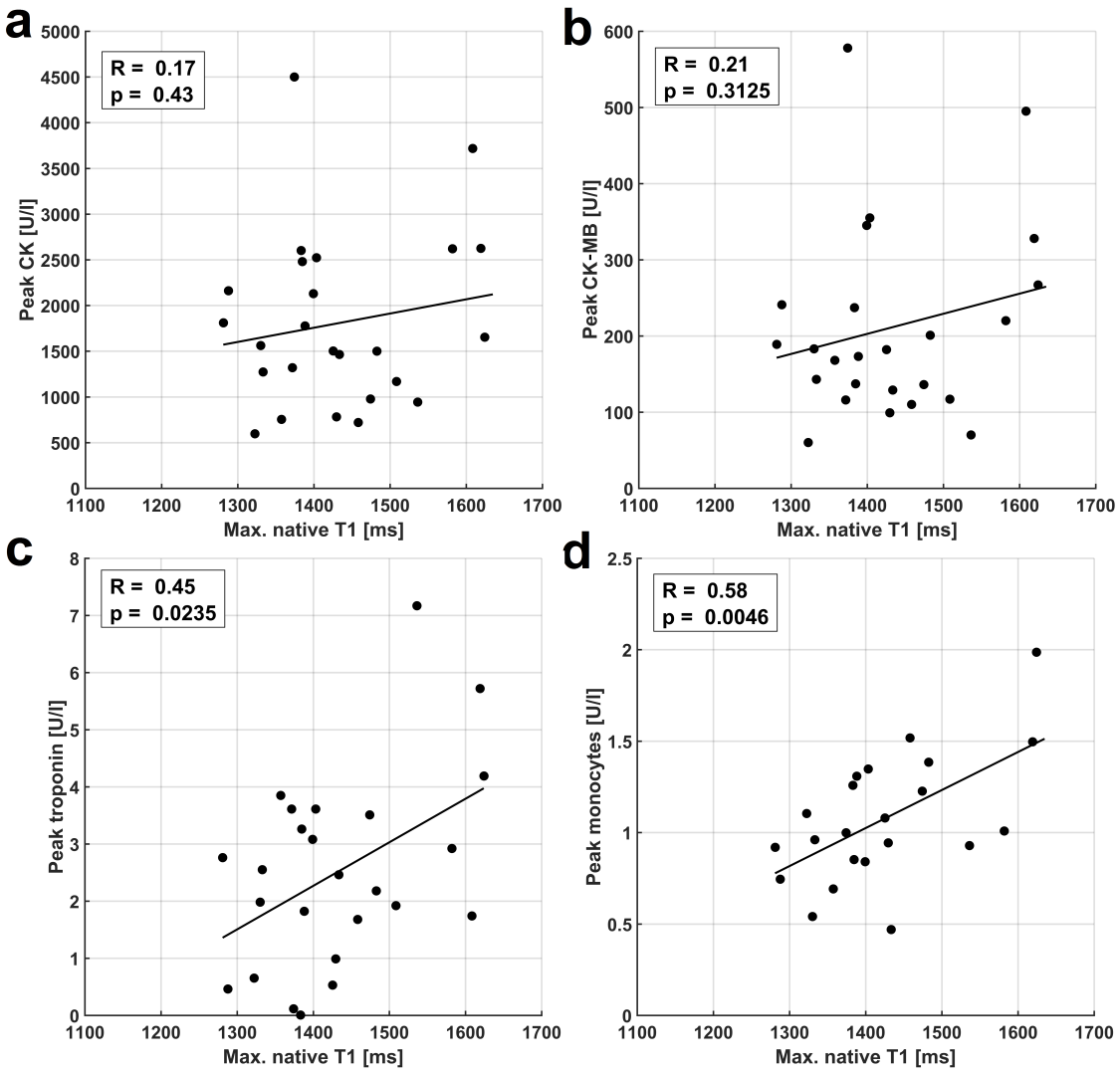

Figure 7.7: Comparison of maximum native T_1 with peak blood parameters CK (**a**), CK-MB fraction (**b**), troponin (**c**), and monocyte counts (**d**). A narrowly significant trend for troponin ($p = 0.024$) and a highly significant correlation ($p = 0.0046$) for monocyte counts was found. No significant correlations to CK or CK-MB fraction were observed.

7.4.1 Comparison of Signal Localization and Magnitude

The first step was the comparison of inter-patient and intra-patient (i.e. intra-slice) signals as shown in Fig. 7.2. The excellent correlations for the latter suggest a very good co-localization of pathophysiological processes indicated by the three different image signals. While in the vast majority of studies, extents of image signals are compared by global thresholding, e.g. using multiples of standard deviations as binary cutoff values, the intra-patient correlations shown herein are independent of differences in absolute signal increase between patients, i.e. differences seen in the correlation slopes in Fig. 7.2(c-d). Despite the

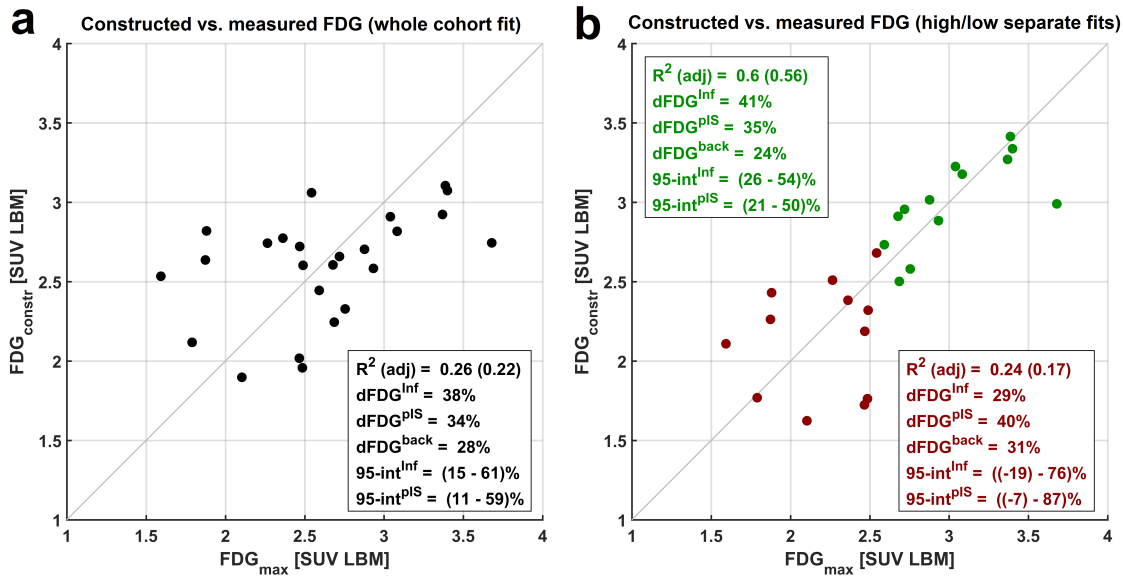

Figure 7.8: Comparison of measured maximum ^{18}F-FDG uptake values FDG_{max} with values FDG_{constr} that were constructed from a linear combination of co-localized relative increase in native T1 and cellular volume. For the fit across the whole cohort (**a**), stronger mismatches between measured and constructed uptake values can be seen at the lower end. Performing separate fits for the high (green) and low (red) ends of FDG_{max} (**b**), significantly better visual and statistical results were obtained for the former (despite on wide outlier), while a fit to the lower end produced similar variability and much weaker fit statistics

good co-localization of signal increases, the heterogeneity of these slopes and equivalently the comparison of maximum values in Fig. 7.3 suggest sensitivities to different underlying tissue properties. Therefore, ECV, ^{18}F-FDG uptake and native T_1 can each be seen as representing mutually distinct combinations of features with respect to infarct-related pathophysiology, while the respective underlying processes are largely co-localized.

7.4.2 Comparison of Signal Magnitudes and External Markers

For myocardial ECV, estimates derived from pre- and post-contrast T_1 mapping have been shown to be sensitive to a number of different disease processes [125] and histologically verified to correlate with fibrosis [37]. With respect to AMI, quantitative ECV mapping has only recently been shown to be associated with functional outcome in patients [77] but further investigation of pathophysiological mechanisms are lacking. While significant association of ECV with edema has been documented at day 1 after AMI in pigs [65], the same study reported a disappearance of this association after 7 days, which suggests edema if at all as a minor contributor to ECV estimates from the study at hand obtained 5 days after AMI. A possible pathophysiological correlate for absolute ECV in this study has been provided in the form of CK/CK-MB blood markers for (myocytic)

cellular damage. The significant correlation between peak CK-MB and ECV is in fact remarkable as it reflects the association of a global, peripheral blood parameter with a focal, biopsy-like imaging result. It may however be seen as an epiphenomenon to the additional finding of a highly significant correlation between ECV at the infarct center and infarct size, where peak CK-MB activity is an established marker for the latter [43]. This observed relationship between the extent of the area being subject to ischemic insult and the amount of myocytic damage at its center may be seen as somewhat mechanistically plausible, considering a decrease of the probability for remaining collateralization with distance to the nearest non-infarcted tissue regions. The much smaller significance for the corresponding correlation observed between peak CK and ECV is consistent with a lower specificity of CK to myocardial damage compared to CK-MB. With respect to FDG, data from this study suggest no correlation of maximum ^{18}F-FDG uptake at the infarct center with peak monocyte or leukocyte counts or global infarct size. This was irrespective of whether maximum ^{18}F-FDG was evaluated in absolute terms as SUV LBM or normalized to LV blood activity as a TBR. A similar finding [119] has been interpreted as a conceivable disproportionality between systemic/peripheral inflammatory cell counts and the presence of migrated inflammatory cells within the myocardium begetting the imaging signal. While it is known that ^{18}F-FDG is taken up by inflammatory cell populations [86], the interpretation of a corresponding image signal from the post-ischemic myocardium is challenging due to the concurrent presence of background contributions from myocyte uptake. Despite a somewhat reliable suppression of physiologic FDG metabolism in healthy cardiomyocytes, the potential presence of post-ischemic FDG uptake due to a switch of metabolism from fatty acids towards glucose consumption early after AMI is a major confounder to the interpretation of ^{18}F-FDG uptake as a purely inflammatory signal [132]. Therefore, ^{18}F-FDG image signals are generally regarded as a mixture of background/blood pool, post-ischemic and inflammatory constituents in this context. Native myocardial T_1 may reflect a variety of pathologic tissue alterations, but is generally accepted to indicate the edematous increase of free water content early after AMI [143]. The expected increase of infarct-centric native T_1 observed in this study is therefore attributed to an edematous reaction, which however did not show a correlation with infarct size as ECV did. With respect to native T_1, the most interesting finding from this study is a highly significant correlation with peak monocyte counts and a weaker but still significant association to peak leukocyte counts, of which monocytes are a subset specific to inflammatory activity. As for ECV, this association of biopsy-like imaging results with peripheral blood markers is remarkable, even more so considering that native T_1 was not found to be related to infarct size. Therefore, the data at hand provides evidence for the fact that myocardial edema and the systemic inflammatory reaction are quantitatively associated. Summarizing the comparison of imaging results with peripheral blood parameters, the data at hand suggest ECV as a marker of cellular damage early after reperfused AMI, with maximum values related to infarct size and therefore reflecting most likely a mechanistic property of the respective infarct. Conversely, the missing correlation to infarct size for maximum ^{18}F-FDG uptake and native T_1 suggest their association with a more patient- than infarct-specific reaction to the ischemic insult. This notion is strongly supported by the observed association of native T_1 with peak monocyte counts.

7.4.3 Estimation of Contributions to ^{18}F-FDG Uptake Signal

As stated before, it is known that, despite dietary preparation, ^{18}F-FDG uptake signal early after AMI represents some mixture of inflammatory cell uptake and remaining post-ischemic metabolism [86,119,132]. Building on the interpretation of maximum ECV and native T_1 as quantitative indicators of (extra-) cellular content and inflammatory activity, it was hypothesized in this study that the maximum values of ^{18}F-FDG uptake observed at the infarct center could be constructed from a linear combination of ECV and native T_1 values measured at the same location. The presented result that at the infarct center only about 40% of the uptake signal actually reflects inflammatory activity may in fact explain earlier accounts of relatively weak associations between measures of mean or maximum ^{18}F-FDG uptake with counts of monocyte subsets despite a relation to functional outcome [119].

However, a number of major assumptions were made that are potentially unreliable when applied on a cohort-average level: First, the association of native T_1 in the tissue with the systemic inflammatory reaction as indicated by monocyte counts is purely circumstantial and lacks further validation with respect to the relationship between peripheral and migrated cell populations. Second, the assumption that post-ischemic metabolism is directly proportional to relative cellular content on a cohort-average while the underlying process is clearly more case-specific may be flawed. Thirdly, the assumption that peak ^{18}F-FDG uptake may be divided into three pathways in the proposed fashion probably represent an additional, significant simplification of reality. This especially applies to assuming a quantitatively consistent background signal within the whole myocardium, which may adequately describe blood pool contributions, but not potentially remaining, variable physiological myocyte uptake. Although errors due to the latter assumption are somewhat constrained by the limited variability observed in remote ^{18}F-FDG signals, the ratio of remote to maximum FDG uptake was often much higher for the lower end of FDGmax values. Performing separate fits for the low and high ends of ^{18}F-FDG signals revealed that mean estimation of signal contributions was mainly driven by high uptake values, while significant variability was introduced from the lower end of values. The latter finding may be explained both by a less stable fit due to a lower range of "fittable" non-background signal, as well as by the fact that potential physiological variations in background signal would have a stronger relative impact. As a consequence, the fit results and confidence intervals corresponding to the high end of values probably represent more reliable estimates of ^{18}F-FDG signal contributions using the proposed approach. As an additional Limitation, since fits were executed on the basis of intra-slice differences between maximum and remote regions for FDG and native T_1, a potential global component of inflammatory activity that may also be present in remote regions would be falsely attributed to the background signal using the described approach. Therefore, the proposed contribution of inflammatory cell populations may be seen as a lower limit.

7.4.4 Limitations

An important translational limitation to results from this study is that patients exhibiting microvascular obstructions post AMI were not amenable to the presented analysis. While there exist propositions on the segmentation of MVO border zones for e.g. ECV map-

ping [77], the difference in spatial resolution between PET and MRI precluded comparable sub-segmentations of the myocardial wall. For similar reasons, only transmural short-axis sectors were defined for LV myocardium, where especially cardiac motion hampers a meaningful sub-segmentation across the myocardial wall in PET. With respect to segmentation, locations for maximum values were determined individually for each modality because the alternative of having one of the three methods be the reference standard for locating the corresponding sectors would have introduced a bias into the comparison and additionally precluded the translation of conclusions to situations where the reference modality is not available. The small spatial differences introduced by individual determination of reference sectors did not suggest this as a significant limitation to the finding that all three modalities indicate mutually distinct processes within the tissue.

The acquisition scheme (3(3)3(3)6) used in this study for MOLLI T_1 mapping has been shown to be more sensitive to variations in heart rate than other, more recently proposed schemes [72]. However, the fact that resting heart rates in the examined cohort did not vary strongly and that heart rate did not correlate with remote native T_1 ($R = -0.22$, $p = 0.3$) do not suggest this as a major confounder to the presented findings.

Additionally, the practice of using peak values of peripheral blood markers as a surrogate for their summed activity may have introduced additional variability into the reported results. While the described practice is known to be relatively accurate for CK/CK-MB [43], the inflammatory reaction indicated by monocyte counts may behave in a more complex fashion. With respect to statistics, the large number of performed correlation analyses may have justified the use of a 1% significance level to make type 1 errors less likely. However, the main conclusions presented herein only rely on findings with p-values < 0.01.

7.4.5 Conclusion

Simultaneously acquired PET/MRI data from this study have shown a close spatial concordance of relative signal increase in combination with a divergence of absolute signal magnitudes between ^{18}F-FDG uptake, native T_1 and ECV early after revascularized AMI. A biopsy-like imaging approach has revealed links between MRI-derived ECV estimates and blood markers of muscular damage as well as an association of the edematous response indicated by absolute native T_1 estimates with the systemic inflammatory activity indicated by peripheral monocyte counts.

On the basis of these pathophysiological correlates, an explorative combination of co-localized PET and MRI results have suggested similar contributions of inflammatory activity and post-ischemic metabolism at the infarct center early after AMI.

Part III

Conclusion

Conclusions

The thesis at hand has presented the development and clinical application of a variety of mathematical methods for modeling the relationship between medical imaging data and physiology. In the context of clinical PET/MRI, simultaneously acquired data from both modalities have been used in a synergistic fashion in order to expand the current understanding of MRI and PET methods for perfusion imaging and tissue characterization. Especially with respect to absolute perfusion quantification using DCE-MRI data, this thesis has made significant contributions to the field by providing important insights into the opportunities and limitations of mathematical methods for dynamic data analysis.

DCE-MRI Deconvolution Modeling

The contributions with respect to DCE-MRI perfusion imaging can be summarized as follows:

- Data in this thesis provides further evidence that measurability of vascular perfusion characteristics using DCE-MRI varies depending on data quality and the physiological state of the tissue. Addressing this, a mathematically sound, hierarchical method to determine the amount of resolvable vascular information from model-based deconvolution analysis was developed and applied in a clinically relevant patient cohort.
- For the described hierarchical approach, it was shown in patients after myocardial infarction that already a small amount of DCE-MRI perfusion data and appropriate application of two-region models can result in extracellular volume estimates comparable to those from equilibrium techniques, implying the potential for significant reductions in scan time and contrast agent dose.
- Using simultaneously acquired, $^{13}NH_3$-ammonia PET perfusion flow estimates as a reference, limitations of DCE-MRI deconvolution analyis in the regime of small transit times were described and adressed through implementation of a physiologically motivated constraint to the widely-used Fermi model.
- Addressing the issue of bolus arrival time estimation, a new method based on shifted low-frequency Fourier phase spectra in the DCE-MRI response function was implemented and shown to be both accurate in determining bolus arrival time as well as providing potential clinical value by characterizing arterial coronary path lengths.
- A spline-based reconstruction of DCE-MRI response functions aimed at model-independent estimation of vascular perfusion parameters beyond perfusion flow was developed and shown to be applicable to vasodilator stress data, however, with significant limitations.

Quantitative MRI Tissue Characterization

MRI-based tissue characterization using the two most established quantitative methods, T_1 and extracellular volume mapping, was applied early after revascularized myocardial infarction and compared to blood markers of cardiovascular pathology and blood counts of inflammatory cell populations. For the core of the infarct - excluding MVOs - correlations with monocyte counts suggested a previously unknown link between the systemic inflammatory response and an increase in native T_1, as well as a link between absolute extracellular volume and creatine kinase-MB expression.

Synergistic Evaluation of PET/MRI data

In addition to insights contributing to the technical refinement or understanding of dynamic MRI data modeling, this thesis has introduced a paradigm of combining quantitative imaging results obtained from simultaneously acquired PET and MRI data. It was applied both to perfusion imaging as well as to tissue characterization, and resulted in findings relating imaging signals and physiology in ways that would not have been conceivable outside of a multi-modality context:

- With respect to quantitative perfusion flow, estimates from simultaneously acquired DCE-MRI and $^{13}NH_3$-ammonia PET were shown to be comparable, but PET resting flows are overestimated by DCE-MRI under the common assumption of equal tissue and arterial hematocrit. A combination of MRI-derived plasma flow and PET-derived blood flow yielded direct estimates of tissue hematocrit, which were found to be lower than arterial hematocrit at rest but increasing at vasodilator stress. These findings may have implications not only for MRI but for all imaging modalities using extracellular agents for the assessment of perfusion.

- For tissue characterization, a combination of fasted ^{18}F-FDG uptake signal in patients early after myocardial infarction with MRI-based native T_1 and ECV estimates was proposed on the basis of concomitantly observed physiological correlates for the latter two. A model constructing the measured ^{18}F-FDG signal as a linear combination of inflammatory and post-ischemic signal pathways yielded similar contributions for both, challenging the notion of fasted ^{18}F-FDG uptake being a purely inflammatory image signal.

Part IV

Appendix

Appendix A

Indicator-Dilution Theory

The transit time distribution h can be seen as a propagation function for indicator particles through a system for which no a priori knowledge exists. It has units of s^{-1}, formally making it a frequency function, and may be defined by [151]:

$$q_0 h(t)\,dt = F C_{out}(t)\,dt \tag{A.1}$$

Indicator flow F through the system has units of volume over time and q_0 is a fixed amount of indicator particles appearing at the entrance of the flow system at time $t = 0$. The term $h(t)dt$ is the fraction of q_0 that is appearing at the system exit between t and $t + dt$. The absolute amount of indicator $q_0 h(t)dt$ appearing at the exit between t and $t + dt$ may be expressed in terms of the sampled concentration at the exit C_{out}, which is the absolute amount of particles normalized by their distribution volume V within the sampled fluid. This volume has traversed the system in a time between t and $t + dt$ and is therefore given by Fdt according to the definition of F, which motivates Eq. A.1. The same holds true in a more global sense, i.e. the total distribution volume of indicator within the system equals flow multiplied by mean circulation (or transit) time. This is in fact one of the main theorems of indicator-dilution theory time called the central volume principle, for which a detailed derivation can be found in [152].

If the initial amount of indicator q_0 is thought of as a single particle, $h(t)dt$ can equivalently be thought of as the probability for that particle to appear at the system exit between t and $t + dt$. Since the amount of indicator at the entrance is fixed, integration of h over all times is normalized and a function H can be defined as:

$$\int_0^{t\to\infty} h(t)\,dt =: H(t \to \infty) = 1 \tag{A.2}$$

In the limit of infinite time after injection, H becomes 1 since every indicator particle has left the flow system at some point. With the normalization of h, it follows from integration of equation A.1:

$$F = \frac{q_0}{\int_0^\infty C_{out}\,dt} \tag{A.3}$$

Equation A.3 can be seen as a classic "invasive" indicator-dilution equation [92]. Here, calculation of flow F is based on the assumption that after a single injection, all fluid appearing at the system exit is also taken out of the system and indicator concentration of

the emerging fluid is measured until there is no more indicator left inside the system. In order to find a formalism that allows flow estimation by external monitoring, i.e. accounting for recirculation or an inability to measure the whole time course of C_{out}, a convolution formula for an arbitrary indicator input can be given as [138,151]:

$$o(t) = \int_0^t i(t-\tau)h(\tau)\,d\tau \tag{A.4}$$

and therefore:

$$C_{out}(t) = \int_0^t C_a(t-\tau)h(\tau)\,d\tau = C_a(t) \otimes h(t) \tag{A.5}$$

The functions $i(t)$ and $o(t)$ were originally thought of as being frequency functions, but they can be generalized to any kind of input. Equation A.5 is the description of a mechanism that propagates volume with a certain concentration of particles through a system via convolution using the propagation function h. In order to solve the problem of having to measure the outflow concentration c_{out}, the Fick principle in its integral formulation is introduced:

$$q(t) = F \int_0^t \left[C_a(\tau) - C_{out}(\tau)\right]\,d\tau \tag{A.6}$$

It relates the amount of indicator $q(t)$ inside a system to the difference in concentrations at its exit and entrance via flow through the system F effectively acting as a statement of mass conservation. Using the Fick principle and Eq. A.5, C_{out} may be eliminated as follows:

$$\begin{aligned} q(t) &= F \int_0^t \left[C_a(\tau) - C_{out}(\tau)\right]\,d\tau \\ &= F \int_0^t \left[C_a(\tau) - \int_0^\tau C_a(T)h(\tau - T)dT\right]\,d\tau \\ &= F \int_0^t \left[C_a(\tau) - C_a(\tau) \cdot H(t-\tau)\right]\,d\tau \\ &= F \cdot \left[C_a(t) \otimes (1 - H(t))\right] \end{aligned}$$

Convolution and integration are switched in the second step assuming discretely sampled functions C_a and h. Restating this in terms of a measurable indicator concentration, the tissue/system density is used changing also dimensions of flow F to volume per time per unit mass:

$$q(t) = \frac{\varrho}{\varrho} \cdot F \cdot [C_a(t) \otimes (1 - H(t))]$$

$$\Leftrightarrow \quad \frac{q(t)}{V_{tissue}} = \varrho \cdot \frac{F}{m_{tissue}} \cdot [C_a(t) \otimes (1 - H(t))]$$

With:

$$\frac{q(t)}{V_{tissue}} = C_m \quad and \quad \frac{F}{m_{tissue}} \to F$$

The density of muscular tissue can be assumed very close to 1 g/mL and therefore be omitted, while flow F is usually given in units of mL/min/g:

$$\begin{aligned} C_m &= F \cdot [C_a(t) \otimes (1 - H(t))] \\ &=: C_a(t) \otimes R_F(t) \end{aligned} \tag{A.7}$$

Equation A.7 relates the externally measurable tissue curve C_m and AIF C_a via the function R_F, incorporating all relevant information about the system, explicitly framed as a normalized function $1 - H(t)$ characterizing system outflow and an amplitude that is equal to flow F.

Appendix B

Low-Resolution AIF Perfusion Results

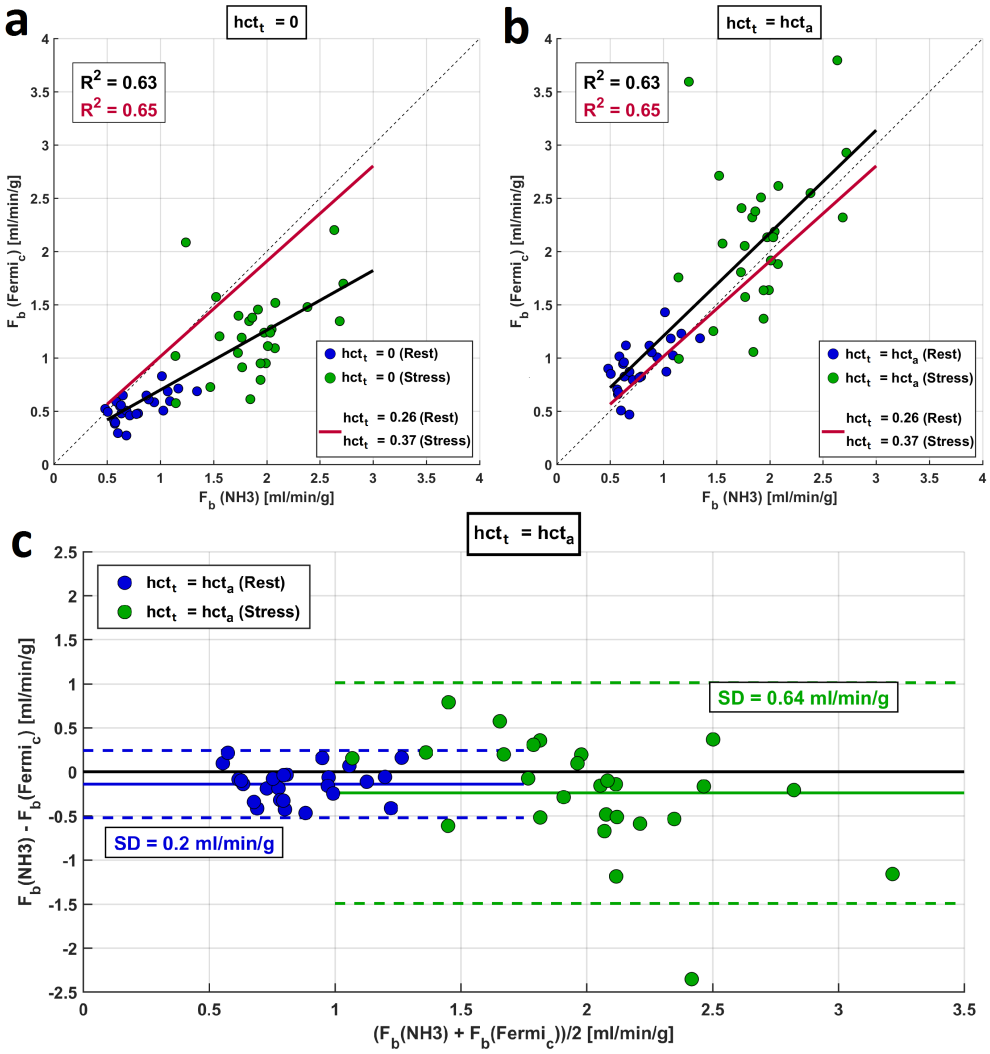

Figure B.1: Slice-average flow comparison to PET for the low-resolution AIF. (**a**/**b**) Similar systematic differences between $^{13}NH_3$ PET and DCE-MRI flow estimates as for the saturation-corrected high-resolution AIF were observed. (**c**) Bland-Altman plot highlighting the higher absolute variability between PET and MRI results especially at stress.

Appendix C

^{18}F-FDG TBR vs. Blood Parameters

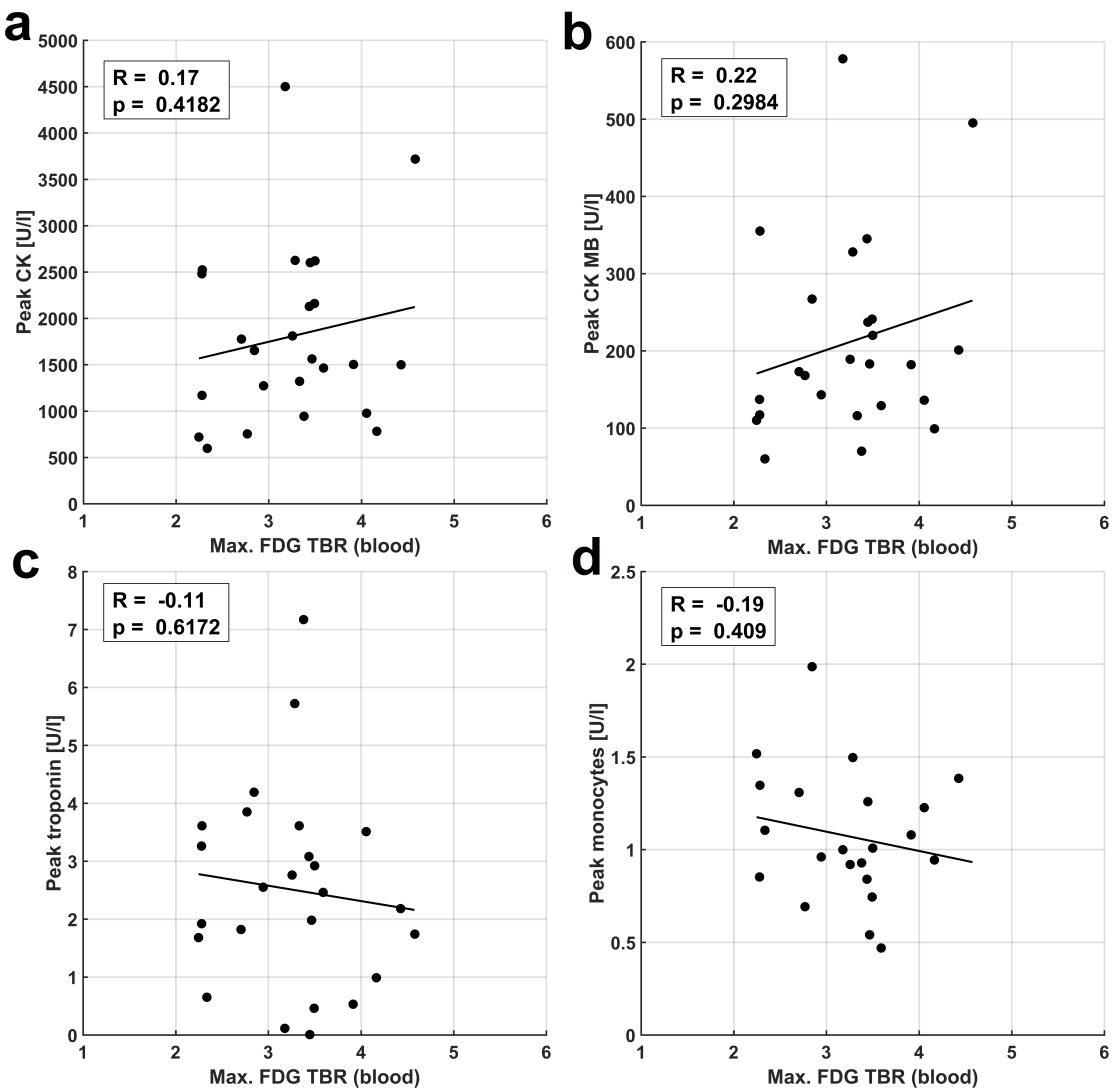

Figure C.1: Comparison of ^{18}F-FDG uptake TBR (normalized to LV blood activity) with peripheral blood markers CK (**a**), CK-MB (**b**), troponin (**c**) and monocyte counts (**d**).

List of Figures

List of Publications

The following peer-reviewed research articles, review articles and conference papers were published during the work on this thesis, each one listed containing both a significant contribution from the author as well as a direct relation to the topic of this thesis:

Research Articles

K. P. Kunze, C. Rischpler, C. Hayes, T. Ibrahim, K.-L. Laugwitz, A. Haase, M. Schwaiger, and S. G. Nekolla. Measurement of Extracellular Volume and Transit Time Heterogeneity Using Contrast-Enhanced Myocardial Perfusion MRI in Patients After Acute Myocardial Infarction. *Magnetic Resonance in Medicine* **77**, 2320–2330 (2017).

K. P. Kunze, S. G. Nekolla, C. Rischpler, S. Zhang, C. Hayes, N. Langwieser, T. Ibrahim, K.-L. Laugwitz and M. Schwaiger. Myocardial Perfusion Quantification using Simultaneously Acquired $^{13}NH_3$-Ammonia PET and Dynamic Contrast-Enhanced MRI in Patients at Rest and Stress. *Magnetic Resonance in Medicine*, doi: 10.1002/mrm.27213 (2018)

K. P. Kunze, R. J. Dirschinger, H. Kossmann, F. Hanus, T. Ibrahim, K.-L. Laugwitz, M. Schwaiger, C. Rischpler and S. G. Nekolla. Quantitative Extracellular Volume, Native T_1 and ^{18}F-FDG PET/MR Imaging in Patients after Revascularized Myocardial Infarction and Association with Markers of Myocardial Damage and Systemic Inflammation. *Journal of Cardiovascular Magnetic Resonance* **20**, 33 (2018).

Review Articles

C. Rischpler, S. G. Nekolla, **K. P. Kunze**, and M. Schwaiger. PET/MRI of the Heart. *Seminars in Nuclear Medicine* **45**, 234–247 (2015).

M. Schwaiger, **K. Kunze**, C. Rischpler, and S. G. Nekolla. PET/MR: Yet Another Tesla? *Journal of Nuclear Cardiology* **24**, 1019–1031 (2017).

S. G. Nekolla, S. van Marwick, S. Schachoff, **K. P. Kunze**, and C. Rischpler. Cardiovascular PET/MRI: Technical Considerations and Outlook. *Current Cardiovascular Imaging Reports* **10**, 36 (2017).

Conference Papers

K. P. Kunze, C. Rischpler, S. Schachoff, M. Schwaiger, and S. G. Nekolla. Measuring the expansion of myocardial extracellular volume using quantitative perfusion imaging: Validation with T1 mapping and simultaneous 18FDGPET in patients after acute myocardial infarction. *Journal of Cardiovascular Magnetic Resonance* **17**, (Suppl. 1) 1–2 (2015).

K. P. Kunze, C. Rischpler, S. Zhang, C. Hayes, M. Schwaiger, and S. G. Nekolla. Towards a synergistic application of multimodal MR/PET myocardial perfusion imaging: Measuring capillary transit time heterogeneity with MRI and blood flow with simultaneous N-13 Ammonia PET. In *Proceedings of the 23rd Annual Meeting of ISMRM, Toronto, Canada*, page 1006 (2015).

K. P. Kunze, C. Rischpler, T. Ibrahim, K.-L. Laugwitz, M. Schwaiger, and S. Nekolla. Quantitative comparison of 18F-FDG PET with MRI-derived extracellular volume measurements in patients after acute myocardial infarction. *Journal of Nuclear Medicine* **56**, (Suppl. 3) 184 (2015).

K. P. Kunze, C. Rischpler, M. Schwaiger, and S. G. Nekolla. Measuring microvascular flow characteristics with myocardial DCE-MRI perfusion data using a model-independent, multi-resolution spline approach in patients at stress. In *Proceedings of the 24th Annual Meeting of ISMRM, Singapore, Singapore*, page 2609 (2016).

K. P. Kunze, T. Vitadello, C. Rischpler, M. Schwaiger, and S. G. Nekolla. Quantitative dynamic MRI in the phase domain: Characterization of coronary arterial morphology using a simple Fourier method to accurately estimate bolus arrival times in DCE-MRI perfusion imaging. In *Proceedings of the 25th Annual Meeting of ISMRM, Honolulu, USA*, page 3238 (2017).

K. P. Kunze, T. Vitadello, C. Rischpler, M. Schwaiger, and S. G. Nekolla. Microvascular tissue characterization with cardiac PET/MRI: Quantitative comparison of myocardial DCE-MRI perfusion flow with 18F-FDG viability PET and coronary angiography. In *Proceedings of the 25th Annual Meeting of ISMRM, Honolulu, USA*, page 0533 (2017).

Acknowledgements

For his long lasting supervision of my thesis work on-site, vocational mentoring, and generous support of my conference and research experiences abroad, I would like to cordially thank PD Dr. Stephan G. Nekolla.

I am grateful to Prof. Dr. Axel Haase for his supervision and support of my work, as well as to Prof. Dr. Markus Schwaiger for providing additional mentoring and an excellent scientific environment during my stay at the department of Nuclear Medicine.

I am indebted to a number of colleagues, friends, and office mates who have helped me during the last couple of years in so many ways: Giaime Rancan, Ian Somlai-Schweiger, Jorge Cabello, HuaLei Shelley Zhang, Sybille Ziegler, Marie Bieth, Negar Omidvari, Tobias Wech, Sebastian Fürst, Isabel Dregely, Franz Schilling, Geoffrey Topping, Rupert Trager, Manuel Schneider, Mathias Lukas and Borjana Bogdanovic.

For the clinical studies, a very special thanks goes to Sylvia Schachoff and Anna Winter for their friendly support and patience with my additions to the many hours of patient scans we have spent together. I would also like to thank Dr. Christoph Rischpler for his enduring support and advice during a number of retrospective data analyses and manuscript preparations.

I would like to express my gratitude towards Drs. Andrew Arai and Peter Kellman for taking the time to host me at NIH in Bethesda, as well as towards Drs. Claudia Prieto and René Botnar for doing the same at St. Thomas' Hospital in London.

Significant funding for this work was provided by the German Research Council (DFG) through grant No. 8810001759. The PET/MRI system on which data acquisition for this thesis was executed was supported by DFG through the Large Equipment Initiative (Großgeräteinitiative) 2010. Additional funding for travel expenses was provided by the TUM Graduate School (TUM-GS).

Bibliography

1. Alessio, A. M., Bassingthwaighte, J. B., Glenny, R. *et al.* Validation of an axially distributed model for quantification of myocardial blood flow using 13N-ammonia PET. *Journal of Nuclear Cardiology* **20,** 64–75 (2013).
2. Arheden, H., Saeed, M., Higgins, C. B. *et al.* Measurement of the Gadopentetate Dimeglumine at Echo-planar MR Imaging to Quantify Myocardial Infarction: Comparison with 99m Tc-DTPA Autoradiography in Rats. *Radiology* **211,** 698–708 (1999).
3. Axel, L. Tissue mean transit time from dynamic computed tomography by a simple deconvolution technique. *Investigative Radiology* **18,** 94–99 (1983).
4. Barnhart, J. L., Kuhnert, N., Bakan, D. A. *et al.* Biodistribution of GdCL3 and Gd-DTPA and their influence on proton magnetic relaxation in rat tissues. *Magnetic Resonance Imaging* **5,** 221–231 (1987).
5. Baskurt, O. K., Yalcin, O., Gungor, F. *et al.* Hemorheological parameters as determinants of myocardial tissue hematocrit values. *Clinical Hemorheology and Microcirculation* **35,** 45–50 (2006).
6. Bassingthwaighte, J. B., Wang, C. Y. & Chan, I. S. Blood-Tissue Exchange via Transport and Transformation by Capillary Endothelial Cells. *Circulation Research* **65,** 997–1020 (1989).
7. Beanlands, R. S. B., DeKemp, R., Scheffel, A. *et al.* Can nitrogen-13 ammonia kinetic modeling define myocardial viability independent of fluorine-18 fluorodeoxyglucose? *Journal of the American College of Cardiology* **29,** 537–543 (1997).
8. Beyer, T., Townsend, D. W., Brun, T. *et al.* A Combined PET/CT Scanner for Clinical Oncology. *Journal of Nuclear Medicine* **41,** 1369–1379 (2000).
9. Biglands, J., Magee, D., Boyle, R. *et al.* Evaluation of the effect of myocardial segmentation errors on myocardial blood flow estimates from DCE-MRI. *Physics in Medicine and Biology* **56,** 2423–2443 (2011).
10. Blumhagen, J. O., Braun, H., Ladebeck, R. *et al.* Field of view extension and truncation correction for MR-based human attenuation correction in simultaneous MR/PET imaging. *Medical Physics* **41,** 022303 (2014).
11. Breton, E., Kim, D., Chung, S. *et al.* Quantitative contrast-enhanced first-pass cardiac perfusion MRI at 3 Tesla with accurate arterial input function and myocardial wall enhancement. *Journal of Magnetic Resonance Imaging* **34,** 676–684 (2011).
12. Brix, G., Schad, L. R., Deimling, M. *et al.* Fast and precise T1 imaging using a TOMROP sequence. *Magnetic Resonance Imaging* **8,** 351–356 (1990).

13. Brix, G., Kiessling, F., Lucht, R. *et al.* Microcirculation and microvasculature in breast tumors: Pharmacokinetic analysis of dynamic MR image series. *Magnetic Resonance in Medicine* **52,** 420–429 (2004).

14. Brix, G., Zwick, S., Griebel, J. *et al.* Estimation of tissue perfusion by dynamic contrast-enhanced imaging: simulation-based evaluation of the steepest slope method. *European Radiology* **20,** 2166–2175 (2010).

15. Brix, G., Zwick, S., Kiessling, F. *et al.* Pharmacokinetic analysis of tissue microcirculation using nested models: multimodel inference and parameter identifiability. *Medical Physics* **36,** 2923–2933 (2009).

16. Broadbent, D. A., Biglands, J. D., Larghat, A. *et al.* Myocardial blood flow at rest and stress measured with dynamic contrast-enhanced MRI: Comparison of a distributed parameter model with a fermi function model. *Magnetic Resonance in Medicine* **70,** 1591–1597 (2013).

17. Broadbent, D. A., Biglands, J. D., Ripley, D. P. *et al.* Sensitivity of Quantitative Myocardial Dynamic Contrast-Enhanced MRI to Saturation Pulse Efficiency, Noise and T1 Measurement Error: Comparison of Nonlinearity Correction Methods. *Magnetic Resonance in Medicine* **75,** 1290–1300 (2016).

18. Buckley, D. L., Kershaw, L. E. & Stanisz, G. J. Cellular-interstitial water exchange and its effect on the determination of contrast agent concentration in vivo: Dynamic contrast-enhanced MRI of human internal obturator muscle. *Magnetic Resonance in Medicine* **60,** 1011–1019 (2008).

19. Buckley, D. L., Biglands, J. D., Larghat, A. *et al.* Myocardial microvascular function at rest and under adenosine stress measured with dynamic contrast-enhanced MRI. *Proceedings of the 19th Annual Meeting of ISMRM, Montreal, Canada,* 1338 (2011).

20. Bulluck, H., White, S. K., Rosmini, S. *et al.* T1 mapping and T2 mapping at 3T for quantifying the area-at-risk in reperfused STEMI patients. *Journal of Cardiovascular Magnetic Resonance* **17,** 73 (2015).

21. Calamante, F., Gadian, D. & Connelly, A. Delay and dispersion effects in dynamic susceptibility contrast MRI: Simulations using singular value decomposition. *Magnetic Resonance in Medicine* **44,** 466–473 (2000).

22. Camici, P. G. & Crea, F. Coronary Microvascular Dysfunction. *The New England Journal of Medicine* **356,** 830–840 (2007).

23. Camici, P. G. & Rimoldi, O. E. The clinical value of myocardial blood flow measurement. *Journal of Nuclear Medicine* **50,** 1076–1087 (2009).

24. Carberry, J., Carrick, D., Haig, C. *et al.* Remote Zone Extracellular Volume and Left Ventricular Remodeling in Survivors of ST-Elevation Myocardial Infarction. *Hypertension* **68,** 385–391 (2016).

25. Carr, D. H., Brown, J., Bydder, G. M. *et al.* Gadolinium-DTPA as a contrast agent in MRI: Initial clinical experience in 20 patients. *American Journal of Roentgenology* **143,** 215–224 (1984).

26. Catana, C., van der Kouwe, A., Benner, T. *et al.* Toward Implementing an MRI-Based PET Attenuation-Correction Method for Neurologic Studies on the MR-PET Brain Prototype. *Journal of Nuclear Medicine* **51,** 1431–1438 (2010).

27. Catana, C., Wu, Y., Judenhofer, M. S. *et al.* Simultaneous Acquisition of Multislice PET and MR Images: Initial Results with a MR-Compatible PET Scanner. *Journal of Nuclear Medicine* **47,** 1968–1977 (2006).

28. Cernicanu, A. & Axel, L. Theory-based signal calibration with single-point T1 measurements for first-pass quantitative perfusion MRI studies. *Academic Radiology* **13,** 686–693 (2006).

29. Cerqueira, M. D., Weissman, N. J., Dilsizian, V. *et al.* Standardized myocardial segmentation and nomenclature for tomographic imaging of the heart: A Statement for Healthcare Professionals from the Cardiac Imaging Committee of the Council on Clinical Cardiology of the American Heart Association. *Circulation* **105,** 539–542 (2002).

30. Cheong, L. H., Koh, T. S. & Hou, Z. An automatic approach for estimating bolus arrival time in dynamic contrast MRI using piecewise continuous regression models. *Physics in Medicine and Biology* **48,** N83–N88 (2003).

31. Coelho-Filho, O. R., Rickers, C., Kwong, R. Y. *et al.* MR myocardial perfusion imaging. *Radiology* **266,** 701–715 (2013).

32. Cousineau, D., Rose, C. P., Lamoureux, D. *et al.* Changes in Cardiac Transcapillary Exchange with Metabolic Coronary Vasodilation in the Intact Dog. *Circulation Research* **53,** 719–730 (1983).

33. Crea, F., Camici, P. G. & Merz, C. N. B. Coronary microvascular dysfunction: An update. *European Heart Journal* **35,** 1101–1111 (2014).

34. Dall'Armellina, E., Piechnik, S. K., Ferreira, V. M. *et al.* Cardiovascular magnetic resonance by non contrast T1-mapping allows assessment of severity of injury in acute myocardial infarction. *Journal of Cardiovascular Magnetic Resonance* **14,** 15 (2012).

35. Delso, G., Fürst, S., Ladebeck, R. *et al.* Performance Measurements of the Siemens mMR Integrated Whole-Body PET/MR Scanner. *Journal of Nuclear Medicine* **52,** 1914–1922 (2011).

36. Depre, C., Vanoverschelde, J. L. & Taegtmeyer, H. Glucose for the heart. *Circulation* **99,** 578–588 (1999).

37. Diao, K.-Y., Yang, Z.-G., Xu, H.-Y. *et al.* Histologic validation of myocardial fibrosis measured by T1 mapping: a systematic review and meta-analysis. *Journal of Cardiovascular Magnetic Resonance* **18,** 92 (2017).

38. Dilsizian, V., Bacharach, S. L., Beanlands, R. S. *et al.* PET myocardial perfusion and metabolism clinical imaging. *Journal of Nuclear Cardiology* **16,** 651–651 (2009).

39. Dixon, T. Simple Proton Spectroscopic lmaging. *Radiology* **153,** 189–194 (1984).

40. Donahue, K. M., Weisskoff, R. M., Chesler, D. A. *et al.* Improving MR quantification of regional blood volume with intravascular T1 contrast agents: accuracy, precision, and water exchange. *Magnetic Resonance in Medicine* **36,** 858–867 (1996).

41. Fårhæus, R. & Lindqvist, T. Viscosity of blood in narrow capillary tubes. *American Journal of Physiology* **96,** 562–568 (1931).

42. Ferreira, V. M., Piechnik, S. K., Dall'Armellina, E. *et al.* Non-contrast T1-mapping detects acute myocardial edema with high diagnostic accuracy: a comparison to T2-weighted cardiovascular magnetic resonance. *Journal of Cardiovascular Magnetic Resonance* **14,** 42 (2012).

43. Fiolet, J. W., ter Welle, H. F., van Capelle, F. J. *et al.* Infarct size estimation from serial CK MB determinations: peak activity and predictability. *British Heart Journal* **49,** 373–380 (1983).

44. Fürst, S., Grimm, R., Hong, I. *et al.* Motion Correction Strategies for Integrated PET/MR. *Journal of Nuclear Medicine* **56,** 261–269 (2015).

45. Garpebring, A., Ostlund, N. & Karlsson, M. A novel estimation method for physiological parameters in dynamic contrast-enhanced MRI: application of a distributed parameter model using Fourier-domain calculations. *IEEE Transactions on Medical Imaging* **28,** 1375–1383 (2009).

46. Gatehouse, P. D., Elkington, A. G., Ablitt, N. A. *et al.* Accurate assessment of the arterial input function during high-dose myocardial perfusion cardiovascular magnetic resonance. *Journal of Magnetic Resonance Imaging* **20,** 39–45 (2004).

47. Gatehouse, P., Lyne, J., Smith, G. *et al.* T2* effects in the dual-sequence method for high-dose first-pass myocardial perfusion. *Journal of Magnetic Resonance Imaging* **24,** 1168–1171 (2006).

48. Gewirtz, H. & Dilsizian, V. Integration of quantitative positron emission tomography absolute myocardial blood flow measurements in the clinical management of coronary artery disease. *Circulation* **133,** 2180–2196 (2016).

49. Gewirtz, H. & Dilsizian, V. Myocardial viability: survival mechanisms and molecular imaging targets in acute and chronic ischemia. *Circulation Research* **120,** 1197–1212 (2017).

50. Grant, A. M., Deller, T. W., Khalighi, M. M. *et al.* NEMA NU 2-2012 performance studies for the SiPM-based ToF-PET component of the GE SIGNA PET/MR system. *Medical Physics* **43,** 2334–2343 (2016).

51. Greenwood, J. P., Maredia, N., Younger, J. F. *et al.* Cardiovascular magnetic resonance and single-photon emission computed tomography for diagnosis of coronary heart disease (CE-MARC): A prospective trial. *The Lancet* **379,** 453–460 (2012).

52. Greulich, S., Kitterer, D., Latus, J. *et al.* Comprehensive Cardiovascular Magnetic Resonance Assessment in Patients With Sarcoidosis and Preserved Left Ventricular Ejection Fraction. *Circulation: Cardiovascular Imaging* **9,** e005022 (2016).

53. Griswold, M. A., Jakob, P. M., Heidemann, R. M. *et al.* Generalized Autocalibrating Partially Parallel Acquisitions (GRAPPA). *Magnetic Resonance in Medicine* **47,** 1202–1210 (2002).

54. Grobner, T. Gadolinium - A specific trigger for the development of nephrogenic fibrosing dermopathy and nephrogenic systemic fibrosis? *Nephrology Dialysis Transplantation* **21,** 1745 (2006).

55. Haacke, E. M., Brown, R. W., Thompson, M. R. *et al.* in *Magnetic Resonance Imaging: Physical Principles and Sequence Design* 83–92 (Wiley, 1999).

56. Haase, A., Frahm, J., Matthaei, D. *et al.* FLASH Imaging. Rapid NMR Imaging Using Low Flip-Angle Pulses. *Journal of Magnetic Resonance* **67,** 258–266 (1986).

57. Hansen, P. C. Analysis of discrete ill-posed problems by means of the L-Curve. *SIAM Review* **34,** 561–580 (1992).

58. Hansen, P. C. Regularization Tools version 4.0 for Matlab 7.3. *Numerical Algorithms* **46,** 189–194 (2007).

59. Hazlewood, C. F., Chang, D. C., Nichols, B. L. *et al.* Nuclear Magnetic Resonance Transverse Relaxation Times of Water Protons in Skeletal Muscle. *Biophysical Journal* **14,** 583–606 (1974).

60. Heyndrickx, G. R., Millard, R. W., McRitchie, R. J. *et al.* Regional myocardial functional and electrophysiological alterations after brief coronary artery occlusion in conscious dogs. *Journal of Clinical Investigation* **56,** 978–985 (1975).

61. Hsu, L. Y., Groves, D. W., Aletras, A. H. *et al.* A quantitative pixel-wise measurement of myocardial blood flow by contrast-enhanced first-pass CMR perfusion imaging: Microsphere validation in dogs and feasibility study in humans. *JACC: Cardiovascular Imaging* **5,** 154–166 (2012).

62. Hudson, H. M. & Larkin, R. S. Accelerated Image Reconstruction Using Ordered Subsets of Projection Data. *IEEE Transactions on Medical Imaging* **13,** 601–609 (1994).

63. Hutchins, G. D., Schwaiger, M., Rosenspire, K. C. *et al.* Noninvasive Quantification of Regional Blood-Flow in the Human Heart Using N-13 Ammonia and Dynamic Positron Emission Tomographic Imaging. *Journal of the American College of Cardiology* **15,** 1032–1042 (1990).

64. Ishida, M., Ichihara, T., Nagata, M. *et al.* Quantification of myocardial blood flow using model based analysis of first-pass perfusion MRI: Extraction fraction of Gd-DTPA varies with myocardial blood flow in human myocardium. *Magnetic Resonance in Medicine* **66,** 1391–1399 (2011).

65. Jablonowski, R., Engblom, H., Kanski, M. *et al.* Contrast-Enhanced CMR Overestimates Early Myocardial Infarct Size: Mechanistic Insights Using ECV Measurements on Day 1 and Day 7. *JACC: Cardiovascular Imaging* **8,** 1379–1389 (2015).

66. Jacobs, M., Benovoy, M., Chang, L.-C. *et al.* Evaluation of an automated method for arterial input function detection for first-pass myocardial perfusion cardiovascular magnetic resonance. *Journal of Cardiovascular Magnetic Resonance* **18** (2016).

67. Jerosch-Herold, M., Wilke, N. & Stillman, A. E. Magnetic resonance quantification of the myocardial perfusion reserve with a Fermi function model for constrained deconvolution. *Medical Physics* **25,** 73–84 (1998).

68. Jerosch-Herold, M., Wilke, N., Wang, Y. *et al.* Direct comparison of an intravascular and an extracellular contrast agent for quantification of myocardial perfusion. *International Journal of Cardiac Imaging* **15,** 453–464 (1999).

69. Jerosch-Herold, M., Swingen, C. & Seethamraju, R. T. Myocardial blood flow quantification with MRI by model-independent deconvolution. *Medical Physics* **29,** 886–897 (2002).

70. Judd, R. M., Reeder, S. B. & May-Newman, K. Effects of water exchange on the measurement of myocardial perfusion using pramagnetic contrast agents. *Magnetic Resonance in Medicine* **342,** 334–342 (1999).

71. Kellman, P., Arai, A. E. & Xue, H. T1 and extracellular volume mapping in the heart: estimation of error maps and the influence of noise on precision. *Journal of Cardiovascular Magnetic Resonance* **15,** 56 (2013).

72. Kellman, P. & Hansen, M. S. T1-mapping in the heart: accuracy and precision. *Journal of Cardiovascular Magnetic Resonance* **16,** 2 (2014).

73. Kellman, P., Hansen, M. S., Nielles-Vallespin, S. *et al.* Myocardial perfusion cardiovascular magnetic resonance: optimized dual sequence and reconstruction for quantification. *Journal of Cardiovascular Magnetic Resonance* **19,** 43 (2017).

74. Kellman, P., Wilson, J. R., Xue, H. *et al.* Extracellular volume fraction mapping in the myocardium, part 2: initial clinical experience. *Journal of Cardiovascular Magnetic Resonance* **14,** 64 (2012).

75. Kershaw, L. E. & Buckley, D. L. Precision in measurements of perfusion and microvascular permeability with T1-weighted dynamic contrast-enhanced MRI. *Magnetic Resonance in Medicine* **56,** 986–992 (2006).

76. Kety, S. S. The theory and applications of the exchange of inert gas at the lungs and tissues. *Pharmacological Reviews* **3,** 1–41 (1951).

77. Kidambi, A., Motwani, M., Uddin, A. *et al.* Myocardial Extracellular Volume Estimation by CMR Predicts Functional Recovery Following Acute MI. *JACC: Cardiovascular Imaging* **10,** 989–999 (2017).

78. Kinahan, P. E., Townsend, D. W., Beyer, T. *et al.* Attenuation correction for a combined 3D PET/CT scanner. *Medical Physics* **25,** 2046–2053 (1998).

79. King, R. B., Raymond, G. M. & Bassingthwaighte, J. B. Modeling blood flow heterogeneity. *Annals of Biomedical Engineering* **24,** 352–372 (1996).

80. King, R. B., Deussen, A., Raymond, G. M. *et al.* A vascular transport operator. *American Journal of Physiology* **265,** H2196–H2208 (1993).

81. Klitzman, B. & Duling, B. R. Microvascular hematocrit and red cell flow in resting and contracting striated muscle. *American Journal of Physiology* **237,** H481–H490 (1979).

82. Koh, T. S., Zeman, V., Darko, J. *et al.* The inclusion of capillary distribution in the adiabatic tissue homogeneity model of blood flow. *Physics in Medicine and Biology* **46,** 1519–1538 (2001).

83. Köstler, H., Ritter, C., Lipp, M. *et al.* Prebolus quantitative MR heart perfusion imaging. *Magnetic Resonance in Medicine* **52,** 296–299 (2004).

84. Kroll, K., Wilke, N., Jerosch-Herold, M. *et al.* Modeling regional myocardial flows from residue functions of an intravascular indicator. *American Journal of Physiology* **271,** H1643–H1655 (1996).

85. Kunze, K. P., Rischpler, C., Hayes, C. *et al.* Measurement of Extracellular Volume and Transit Time Heterogeneity Using Contrast-Enhanced Myocardial Perfusion MRI in Patients After Acute Myocardial Infarction. *Magnetic Resonance in Medicine* **77,** 2320–2330 (2017).

86. Lee, W. W., Marinelli, B., Van Der Laan, A. M. *et al.* PET/MRI of inflammation in myocardial infarction. *Journal of the American College of Cardiology* **59,** 153–163 (2012).

87. Levin, C. S. & Hoffman, E. J. Calculation of positron range and its effect on the fundamental limit of positron emission tomography system spatial resolution. *Physics in Medicine and Biology* **44,** 781–799 (1999).

88. Li, X., Springer, C. S. & Jerosch-Herold, M. First-pass dynamic contrast-enhanced MRI with extravasating contrast reagent: Evidence for human myocardial capillary recruitment in adenosine-induced hyperemia. *NMR in Biomedicine* **22,** 148–157 (2009).

89. Look, D. C. & Locker, D. R. Time saving in measurement of NMR and EPR relaxation times. *Review of Scientific Instruments* **41,** 250–251 (1970).

90. Love, C., Tomas, M. B., Tronco, G. G. *et al.* FDG PET of infection and inflammation. *Radiographics* **25,** 1357–1368 (2005).

91. Martinez-Möller, A., Souvatzoglou, M., Delso, G. *et al.* Tissue Classification as a Potential Approach for Attenuation Correction in Whole-Body PET/MRI: Evaluation with PET/CT Data. *Journal of Nuclear Medicine* **50,** 520–526 (2009).

92. Meier, P. & Zierler, K. L. On the theory of the indicator-dilution method for measurement of blood flow and volume. *Journal of Applied Physiology* **6,** 731–744 (1954).

93. Messroghli, D. R., Greiser, A., Fröhlich, M. *et al.* Optimization and validation of a fully-integrated pulse sequence for modified look-locker inversion-recovery (MOLLI) T1 mapping of the heart. *Journal of Magnetic Resonance Imaging* **26,** 1081–1086 (2007).

94. Messroghli, D. R., Moon, J. C., Ferreira, V. M. *et al.* Clinical recommendations for cardiovascular magnetic resonance mapping of T1, T2, T2* and extracellular volume: A consensus statement by the Society for Cardiovascular Magnetic Resonance (SCMR) endorsed by the European Association for Cardiovascular Imagi. *Journal of Cardiovascular Magnetic Resonance* **19,** 1–24 (2017).

95. Messroghli, D. R., Radjenovic, A., Kozerke, S. *et al.* Modified look-locker inversion recovery (MOLLI) for high-resolution T 1 mapping of the heart. *Magnetic Resonance in Medicine* **52,** 141–146 (2004).

96. Messroghli, D. R., Walters, K., Plein, S. *et al.* Myocardial T1 mapping: Application to patients with acute and chronic myocardial infarction. *Magnetic Resonance in Medicine* **58,** 34–40 (2007).

97. Metz, S., Ganter, C., Lorenzen, S. *et al.* Phenotyping of Tumor Biology in Patients by Multimodality Multiparametric Imaging: Relationship of Microcirculation, avb3 Expression, and Glucose Metabolism. *Journal of Nuclear Medicine* **51,** 1691–1698 (2010).

98. Miller, C. A., Naish, J. H., Ainslie, M. P. *et al.* Voxel-wise quantification of myocardial blood flow with cardiovascular magnetic resonance: effect of variations in methodology and validation with positron emission tomography. *Journal of Cardiovascular Magnetic Resonance* **16,** 11 (2014).

99. MMID4 Manual. Documentation Version 3.0, published by the National Simulation Resource, University of Washington (WA) (2003).

100. Moon, J. C., Messroghli, D. R., Kellman, P. *et al.* Myocardial T1 mapping and extracellular volume quantification: a Society for Cardiovascular Magnetic Resonance (SCMR) and CMR Working Group of the European Society of Cardiology consensus statement. *Journal of Cardiovascular Magnetic Resonance* **15,** 92 (2013).

101. Morcos, S. K. Extracellular gadolinium contrast agents: Differences in stability. *European Journal of Radiology* **66,** 175–179 (2008).

102. Morton, G., Chiribiri, A., Ishida, M. *et al.* Quantification of absolute myocardial perfusion in patients with coronary artery disease. *Journal of the American College of Cardiology* **60,** 1546–1555 (2012).

103. Mouridsen, K., Hansen, M. B., Østergaard, L. *et al.* Reliable estimation of capillary transit time distributions using DSC-MRI. *Journal of Cerebral Blood Flow and Metabolism* **34,** 1511–1521 (2014).

104. Muzik, O., Beanlands, R. S., Hutchins, G. D. *et al.* Validation of nitrogen-13-ammonia tracer kinetic model for quantification of myocardial blood flow using PET. *Journal of Nuclear Medicine* **34,** 83–91 (1993).

105. Nahrendorf, M., Swirski, F. K., Aikawa, E. *et al.* The healing myocardium sequentially mobilizes two monocyte subsets with divergent and complementary functions. *The Journal of Experimental Medicine* **204,** 3037–3047 (2007).

106. Nekolla, S. G., Reder, S., Saraste, A. *et al.* Evaluation of the novel myocardial perfusion positron-emission tomography tracer 18F-BMS-747158-02: Comparison to 13N-ammonia and validation with microspheres in a pig model. *Circulation* **119,** 2333–2342 (2009).

107. Nekolla, S., Gneiting, T., Syha, J. *et al.* T1 maps by K-space reduced snapshot-FLASH MRI. *Journal of Computer Assisted Tomography* **16,** 327–332 (1992).

108. Nuyts, J., Bal, G., Kehren, F. *et al.* Completion of a truncated attenuation image from the attenuated PET emission data. *IEEE Transactions on Medical Imaging* **32,** 237–246 (2013).

109. Østergaard, L., Kristiansen, S. B., Angleys, H. *et al.* The role of capillary transit time heterogeneity in myocardial oxygenation and ischemic heart disease. *Basic Research in Cardiology* **109,** 409 (2014).

110. Pack, N. A., DiBella, E. V. R., Rust, T. C. *et al.* Estimating myocardial perfusion from dynamic contrast-enhanced CMR with a model-independent deconvolution method. *Journal of Cardiovascular Magnetic Resonance* **10,** 52 (2008).

111. Pack, N. A., DiBella, E. V. R., Wilson, B. D. *et al.* Quantitative myocardial distribution volume from dynamic contrast-enhanced MRI. *Magnetic Resonance Imaging* **26,** 532–542 (2008).

112. Papanastasiou, G., Williams, M. C., Kershaw, L. E. *et al.* Measurement of myocardial blood flow by cardiovascular magnetic resonance perfusion: comparison of distributed parameter and Fermi models with single and dual bolus. *Journal of Cardiovascular Magnetic Resonance* **17,** 1–10 (2015).

113. Pietsch, H., Pering, C., Lengsfeld, P. *et al.* Evaluating the role of zinc in the occurrence of fibrosis of the skin: A preclinical study. *Journal of Magnetic Resonance Imaging* **30,** 374–383 (2009).

114. Pries, A. R., Neuhaus, D. & Gaehtgens, P. Blood viscosity in tube flow: dependence on diameter and hematocrit. *The American Journal of Physiology* **263,** H1770–H1778 (1992).

115. Pries, A. R., Secomb, T. W. & Gaehtgens, P. Biophysical aspects of blood flow in the microvasculature. *Cardiovascular Research* **32,** 654–667 (1996).

116. Qayyum, A. A., Hasbak, P., Larsson, H. B. W. *et al.* Quantification of myocardial perfusion using cardiac magnetic resonance imaging correlates significantly to rubidium-82 positron emission tomography in patients with severe coronary artery disease: A preliminary study. *European Journal of Radiology* **83,** 1120–1128 (2014).

117. Rahimtoola, S. H. The hibernating myocardium. *American Heart Journal* **117,** 211–221 (1989).

118. Ridgway, J. P. Cardiovascular magnetic resonance physics for clinicians: part I. *Journal of Cardiovascular Magnetic Resonance* **12,** 71 (2010).

119. Rischpler, C., Dirschinger, R. J., Nekolla, S. G. *et al.* Prospective Evaluation of 18F-Fluorodeoxyglucose Uptake in Postischemic Myocardium by Simultaneous Positron Emission Tomography/Magnetic Resonance Imaging as a Prognostic Marker of Functional Outcome. *Circulation: Cardiovascular imaging* **9,** e004316 (2016).

120. Rischpler, C., Langwieser, N., Souvatzoglou, M. *et al.* PET/MRI early aftermyocardial infarction: Evaluation of viability with late gadolinium enhancement transmurality vs. 18F-FDG uptake. *European Heart Journal: Cardiovascular Imaging* **16,** 661–669 (2015).

121. Rischpler, C., Nekolla, S. G., Kunze, K. P. *et al.* PET/MRI of the heart. *Seminars in Nuclear Medicine* **45,** 234–247 (2015).

122. Robson, P. M., Dweck, M. R., Trivieri, M. G. *et al.* Coronary Artery PET/MR Imaging: Feasibility, Limitations, and Solutions. *JACC: Cardiovascular Imaging* **10,** 1103–1112 (2017).

123. Rogers, I. S., Nasir, K., Figueroa, A. L. *et al.* Feasibility of fdg imaging of the coronary arteries: Comparison between acute coronary syndrome and stable angina. *JACC: Cardiovascular Imaging* **3,** 388–397 (2010).

124. Rose, C. P. & Goresky, C. A. Vasomotor control of capillary transit time heterogeneity in the canine coronary circulation. *Circulation Research* **39,** 541–554 (1976).

125. Sado, D. M., Flett, A. S., Banypersad, S. M. *et al.* Cardiovascular magnetic resonance measurement of myocardial extracellular volume in health and disease. *Heart* **98,** 1436–1441 (2012).

126. Sangren, W. C. & Sheppard, C. W. A mathematical derivation of the exchange of a labeled substance between a liquid flowing in a vessel and an external compartment. *The Bulletin of Mathematical Biophysics* **15,** 387–394 (1953).

127. Schabel, M. C. A unified impulse response model for DCE-MRI. *Magnetic Resonance in Medicine* **68,** 1632–1646 (2012).

128. Schelbert, H. R., Phelps, M. E., Huang, S. C. *et al.* N-13 ammonia as an indicator of myocardial blood flow. *Circulation* **63,** 1259–1272 (1981).

129. Schmidt, R., Graafen, D., Weber, S. *et al.* Computational fluid dynamics simulations of contrast agent bolus dispersion in a coronary bifurcation: Impact on MRI- based quantification of myocardial perfusion. *Computational and Mathematical Methods in Medicine* **2013** (2013).

130. Schwaiger, M., Brunken, R., Grover-McKay, M. *et al.* Regional myocardial metabolism in patients with acute myocardial infarction assessed by positron emission tomography. *Journal of the American College of Cardiology* **8,** 800–808 (1986).

131. Schwaiger, M., Kunze, K., Rischpler, C. *et al.* PET/MR: Yet another Tesla? *Journal of Nuclear Cardiology* **24,** 1019–1031 (2017).

132. Schwaiger, M., Schelbert, H. R., Ellison, D. *et al.* Sustained regional abnormalities in cardiac metabolism after transient ischemia in the chronic dog model. *Journal of the American College of Cardiology* **6,** 336–347 (1985).

133. Sherry, A. D., Caravan, P. & Lenkinski, R. E. Primer on gadolinium chemistry. *Journal of Magnetic Resonance Imaging* **30,** 1240–1248 (2009).

134. Sourbron, S. P. & Buckley, D. L. Tracer kinetic modelling in MRI: estimating perfusion and capillary permeability. *Physics in Medicine and Biology* **57,** R1–R33 (2012).

135. Sourbron, S. P. & Buckley, D. L. On the scope and interpretation of the Tofts models for DCE-MRI. *Magnetic Resonance in Medicine* **66,** 735–745 (2011).

136. St Lawrence, K. S. & Lee, T. Y. An adiabatic approximation to the tissue homogeneity model for water exchange in the brain: I. Theoretical derivation. *Journal of Cerebral Blood Flow and Metabolism* **18,** 1365–1376 (1998).

137. Stanisz, G. J. & Henkelman, R. M. Gd-DTPA relaxivity depends on macromolecular content. *Magnetic Resonance in Medicine* **44,** 665–667 (2000).

138. Stephenson, J. L. Theory of the measurement of blood flow by the dilution of an indicator. *Bulletin of Mathematical Biophysics* **10,** 117–121 (1948).

139. Tofts, P. S. & Kermode, A. G. Measurement of the blood-brain barrier permeability and leakage space using dynamic MR imaging. 1. Fundamental concepts. *Magnetic Resonance in Medicine* **17,** 357–367 (1991).

140. Tran-Gia, J., Wech, T., Hahn, D. *et al.* Consideration of slice profiles in inversion recovery Look-Locker relaxation parameter mapping. *Magnetic Resonance Imaging* **32,** 1021–1030 (2014).

141. Treibel, T. A., Zemrak, F., Sado, D. M. *et al.* Extracellular volume quantification in isolated hypertension - changes at the detectable limits? *Journal of Cardiovascular Magnetic Resonance* **17,** 74 (2015).

142. Tsujioka, H., Imanishi, T., Ikejima, H. *et al.* Impact of Heterogeneity of Human Peripheral Blood Monocyte Subsets on Myocardial Salvage in Patients With Primary Acute Myocardial Infarction. *Journal of the American College of Cardiology* **54,** 130–138 (2009).

143. Ugander, M., Bagi, P. S., Oki, A. J. *et al.* Myocardial edema as detected by pre-contrast T1 and T2 CMR delineates area at risk associated with acute myocardial infarction. *JACC: Cardiovascular Imaging* **5,** 596–603 (2012).

144. Verotta, D. Two constrained deconvolution methods using spline functions. *Journal of Pharmacokinetics and Biopharmaceutics* **21,** 609–636 (1993).

145. Wang, H., DiBella, E. V. R., Adluru, G. *et al.* Effect of slice excitation profile on ungated steady state cardiac perfusion imaging. *Biomedical Physics & Engineering Express* **3** (2017).

146. Watson, C., Newport, D. & Casey, M. in *Three-Dimensional Image Reconstruction in Radiation and Nuclear Medicine* 255–268 (Aix-les-Bains, France: Kluwer Academic Publishers, 1996).

147. Weingärtner, S., Meßner, N. M., Budjan, J. *et al.* Myocardial T1-mapping at 3T using saturation-recovery: reference values, precision and comparison with MOLLI. *Journal of Cardiovascular Magnetic Resonance* **18,** 84 (2017).

148. White, S. K., Sado, D. M., Flett, A. S. *et al.* Characterising the myocardial interstitial space: the clinical relevance of non-invasive imaging. *Heart* **98,** 773–779 (2012).

149. Wollenweber, T., Roentgen, P., Schäfer, A. *et al.* Characterizing the inflammatory tissue response to acute myocardial infarction by clinical multimodality noninvasive imaging. *Circulation: Cardiovascular Imaging* **7,** 811–818 (2014).

150. Xue, H., Zuehlsdorff, S., Kellman, P. *et al.* in *MICCAI* 741–749 (2009).

151. Zierler, K. L. Equations for measuring blood flow by external monitoring of radioisotopes. *Circulation Research* **16,** 309–321 (1965).

152. Zierler, K. L. Theoretical basis of indicator-dilution methods for measuring flow and volume. *Circulation Research* **10,** 393–407 (1962).

Online Resources

153. *http://chem.ch.huji.ac.il/nmr/techniques/1d/pulseq_files/fid.gif*
154. *http://commons.wikimedia.org/wiki/File:Fahraeus_effect.svg*
155. *http://commons.wikimedia.org/wiki/File:Gadoteric_acid.png*
156. *http://commons.wikimedia.org/wiki/File:Gd(DTPA)(aq)2-.png*
157. *http://en.ecgpedia.org/wiki/File:Coronary_anatomy.png*
158. *http://physiome.org/jsim/models/webmodel/NSR/MMID4/*
159. *http://www.who.int/mediacentre/factsheets/fs310/en/*
160. *https://commons.wikimedia.org/wiki/File:Diagram_of_the_human_heart_(cropped).svg*

All pages visited on February 19th 2018.